Charged systems in bulk and at interfaces

Dissertation
zur Erlangung des akademischen Grades
Doktor der Naturwissenschaften (Dr. rer. nat.)
in der Wissenschaftsdisziplin Theoretische Physik

eingereicht an der
Matematisch-Naturwissenschaftlichen Fakultät der Universität Potsdam

angefertigt am
Max-Planck-Institut für Kolloid- und Grenzflächenforschung in Golm

von

André Guérin Moreira

geboren am 3. Mai 1973 in Rio de Janeiro

Potsdam, im Januar 2001

Summary

One of the rules-of-thumb of colloid and surface physics is that most surfaces are charged when in contact with a solvent, usually water. This is the case, for instance, in charge-stabilized colloidal suspensions, where the surface of the colloidal particles are charged (usually with a charge of hundreds to thousands of e, the elementary charge), monolayers of ionic surfactants sitting at an air–water interface (where the water-loving head groups become charged by releasing counterions), or bilayers containing charged phospholipids (as cell membranes). In this work, we look at some model-systems that, although being a simplified version of reality, are expected to capture some of the physical properties of real charged systems (colloids and electrolytes).

We initially study the simple double layer, composed by a charged wall in the presence of its counterions. The charges at the wall are smeared out and the dielectric constant is the same everywhere. The Poisson-Boltzmann (PB) approach gives asymptotically exact counterion density profiles around charged objects in the weak-coupling limit of systems with low-valent counterions, surfaces with low charge density and high temperature (or small Bjerrum length). Using Monte Carlo simulations, we obtain the profiles around the charged wall and compare it with both Poisson-Boltzmann (in the low coupling limit) and the novel strong coupling (SC) theory in the opposite limit of high couplings. In the latter limit, the simulations show that the SC leads in fact to asymptotically correct density profiles. We also compare the Monte Carlo data with previously calculated corrections to the Poisson-Boltzmann theory. We also discuss in detail the methods used to perform the computer simulations.

After studying the simple double layer in detail, we introduce a dielectric jump at the charged wall and investigate its effect on the counterion density distribution. As we will show, the Poisson-Boltzmann description of the double layer remains a good approximation at low coupling values, while the strong coupling theory is shown to lead to the correct density profiles close to the wall (and at all couplings). For very large couplings, only systems where the difference between the dielectric constants of the wall and of the solvent is small are shown to be well described by SC.

Another experimentally relevant modification to the simple double layer is to make the charges at the plane discrete. The counterions are still assumed to be point-like, but we constraint the distance of approach between ions in the plane and counterions to a minimum distance D. The ratio between D and the distance between neighboring ions in the plane is, as we will see, one of the important quantities in determining the influence of the discrete nature of the charges at the wall over the density profiles. Another parameter that plays an important role, as in the previous case, is the coupling as we will demonstrate, systems with higher coupling are more subject to discretization effects than systems with low coupling parameter.

After studying the isolated double layer, we look at the interaction between two double lay-

ers. The system is composed by two equally charged walls at distance d, with the counterions confined between them. The charge at the walls is smeared out and the dielectric constant is the same everywhere. Using Monte-Carlo simulations we obtain the inter-plate pressure in the global parameter space, and the pressure is shown to be negative (attraction) at certain conditions. The simulations also show that the equilibrium plate separation (where the pressure changes from attractive to repulsive) exhibits a novel unbinding transition. We compare the Monte Carlo results with the strong-coupling theory, which is shown to describe well the bound states of systems with moderate and high couplings. The regime where the two walls are very close to each other is also shown to be well described by the SC theory.

Finally, Using a field-theoretic approach, we derive the exact low-density ("virial") expansion of a binary mixture of positively and negatively charged hard spheres (two-component hard-core plasma, TCPHC). The free energy obtained is valid for systems where the diameters d_+ and d_- and the charge valences q_+ and q_- of positive and negative ions are unconstrained, i.e., the same expression can be used to treat dilute salt solutions (where typically $d_+ \sim d_-$ and $q_+ \sim q_-$) as well as colloidal suspensions (where the difference in size and valence between macroions and counterions can be very large). We also discuss some applications of our results.

Contents

Chapter 1

Introduction

Colloidal systems surround us. Smoke, formed by solid particles suspended in air, fog, which is composed of tiny liquid drops also suspended in air (also known as “aerosol”), milk, a suspension of liquid drops in another liquid (emulsion) and ink, in general solid particles suspended in a liquid, are a few examples of colloids that can be ordinarily found in every day’s life. In fact, colloidal physics and chemistry is one of the scientific fields with most examples of industrial applications, as for instance in processing food (e.g. stabilization of emulsions, like milk and mayonnaise), in extraction of oil (with the help of surfactants), pharmaceutics (drug delivery with hollow polymeric capsules that can in principle transport drugs directly to the places where they are needed in the body), and even aerospace (use of new super-glues that can glue the joining parts of airplanes). On the environmental side, colloidal particles can be also used to adsorb pollutants and purify water. Beyond the technological applicability, very fundamental questions concerning self-organized order in colloidal systems are being asked (and sometimes answered) within the realm of soft condensed matter physics[65, 118].

Colloidal suspensions can be roughly divided into *lyophilic*, i.e., the particles interact favorably with the solvent and like to stay in solution and *lyophobic*, which is the opposite: the particles prefer to stick to each other and form larger aggregates that eventually drop out of solution. One can avoid this latter process of aggregation by charging the colloidal particles, which then (in principle) stay away from each other due to the Coulombic repulsive interaction. Electrostatically stabilized systems can last very long (some water-soluble paints are stabilized this way) even though the suspension might be only a metastable state. These are the so-called charge stabilized colloidal suspensions. Another class of charged systems that is also very important are salt (or electrolyte) solutions. Ions like sodium, potassium, calcium, etc. are fundamental to living cells (it is no accident that we use salt in our food).

The term colloid was coined by the Scottish chemist Thomas Graham (1805–1869), who found that substances like starch, gelatin and glue when in solution had very different properties from, say, sugar or salt. For instance, colloidal particles diffuse much slower when in solution than non-colloidal particles. Also, if a solution of sugar and glue inside a dialysis bag is put into contact with a reservoir of water, the sugar diffuses through the membrane into the water, while the glue is unable to cross the pores of the dialysis bag. We now know that the size of colloidal particles (or macromolecules, in contrast to simple molecular systems) is responsible for such differences.

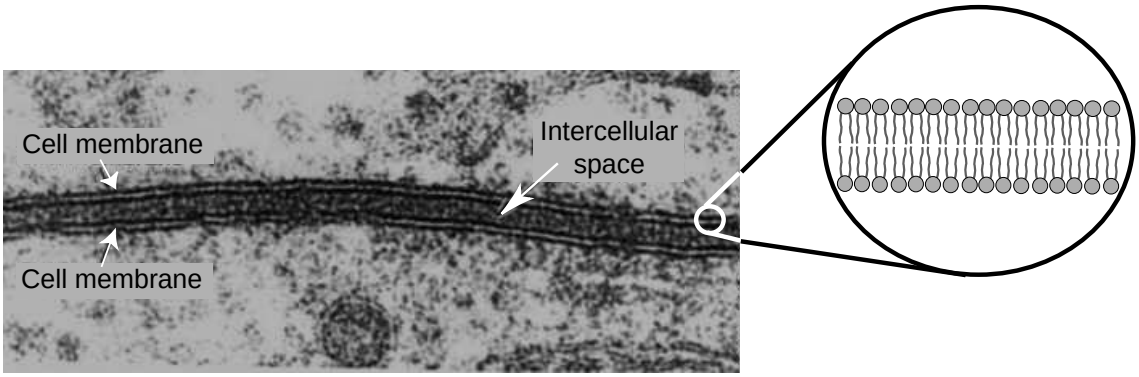

Figure 1.1: Photo of two cells close to each other. The cell membranes (clearly visible in the photo) are in general charged due to the presence of charged phospholipids in their composition, which are organized in a bilayer, as schematically represented. Picture adapted from Ref. [21].

Typically, colloidal particles have radii that lie between 1 nm and 1000 nm, that is, the particles are made of many atoms, but not enough to make the object really macroscopic (for this reason these are often referred to as *mesoscopic* particles).

In the mesoscopic scale, surface properties can play an extremely important role. To see this, let us assume a spherical colloidal particle with radius R formed by atoms (or molecules) that have radius r_0. The ratio between the number of atoms (or molecules) that are at the surface and the total number of atoms in the colloidal particle is approximately given by $4r_0/R$. This means that if $r_0 \sim 0.1$ nm and $R \sim 1$ nm, 40% of the atoms forming the colloidal particles are in fact at its surface; if $R \sim 1000$ nm, this number becomes 0.04%, which although small, is not infinitesimal (as it would be for a macroscopic object). This also shows why colloidal suspension can sometimes be used as catalysts in chemical reactions, since there is a lot of area available in a relatively small volume: if one sums the areas of all particles (assuming they are small spheres of radius 10 nm) that are in a liter of a suspension at volume fraction 0.1, one finds $\sim 10^4$ m^2, which is a quite impressive number.

One of the rules-of-thumb of colloid and surface physics is that most surfaces are charged when in contact with a solvent (usually water). The charges on the surfaces may be chemically bounded or adsorbed to the interface, and the pH of the solution can also influence the value of the charge at the surface. There are usually two interactions between the particles that are important, namely the electrostatic and the van der Waals. Gravity, for instance, does not play any role: the ratio between the gravitational and the electrostatic force between two colloidal particles is generally smaller than 10^{-25}. If the solutions are enough dilute, the van der Waals interactions becomes also unimportant in comparison to the Coulomb interactions. Colloidal particles that are charged have typically a surface charge density of one e (elementary charge) per one hundred Å^2 (with a total charge between the hundreds and thousands of e per colloidal particle). The asymmetry in size and charge between the colloidal particles and their counterions is very large, and is one of the salient aspects of charged colloids. Loosely speaking, the surface of a colloidal particle looks to a counterion almost like an infinite charged plane. Charged surfaces are also important in biological system, as for instance in cell membranes, which contain charged phospholipids (i.e., with head-groups that become charged when in solution) in their composition.

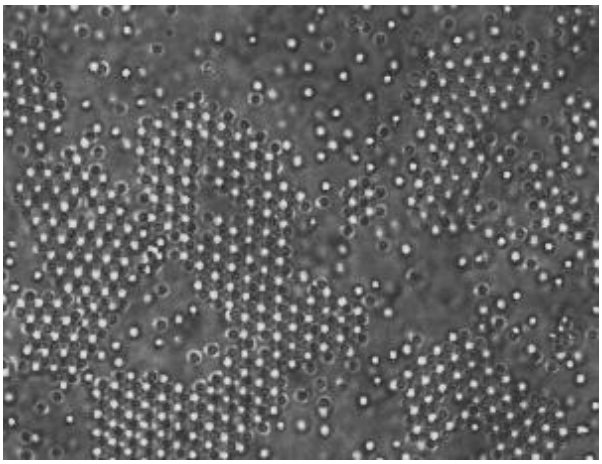

Figure 1.2: Colloidal crystal in coexistence with its fluid (picture from Ref. [59]). Although the particles are equally charged, some kind of attraction between them has to develop so that the crystal can form.

The pioneering works in the field of charged fluids and colloidal physics done by Faraday, Debye and Hückel, Gouy and Chapman, Bjerrum, Meyer, Verwey and Overbeek, just to mention a few, have brought our understanding of these systems to a relatively high standard. However, there are still many open questions and unexplained phenomena (cf. Fig. 1.2), which makes this an interesting area for research. We approach here some models that, although crude simplifications of reality and very simple in their concept, are yet quite challenging. A better knowledge of the simple double layer (modeled by an infinite charged plane in the presence of counterions), or of a two-component plasma (also known as the primitive model, where oppositely charged hard spheres are in solution) can cast some light onto real systems.

Fig. 1.3 summarizes the organization of this thesis. We start by looking at inhomogeneous charged systems. In the next three Chapters we will study the already mentioned double layer problem, in its simplest case where a charged wall is in the presence of counterions (Chapter 2), as well as when some modifications are incorporated so that the idealized model becomes slightly more realistic: when there is a dielectric jump at the charged interface (Chapter 3) or when the charges fixed on the wall are made discrete (Chapter 4). We will look at the thermodynamic properties of these systems with the help of Monte Carlo simulations, and compare it with some analytical results.

After this, we will look at the interaction between double layers (Chapter 5), where two similarly charged walls confine their counterions between them. This is a natural step after studying the isolated double layer, and has direct consequences to important problems like DNA condensation[99] or the stability of colloidal suspensions[114]. Again, Monte Carlo simulations are used to study this problem, and comparison with analytical results are also made.

Finally, in Chapter 6 we move from inhomogeneous to bulk systems and calculate the low-density ("virial") expansion of the free energy of the two-component plasma. This is an asymptotic result, only valid for very dilute solutions; however, it allows one to treat in equal footing both dilute electrolyte solutions (where co- and counterions have similar charge valences and sizes) as well as dilute colloidal suspensions (where the size and charge asymmetry between the macroions and their counterions can be of orders of magnitude).

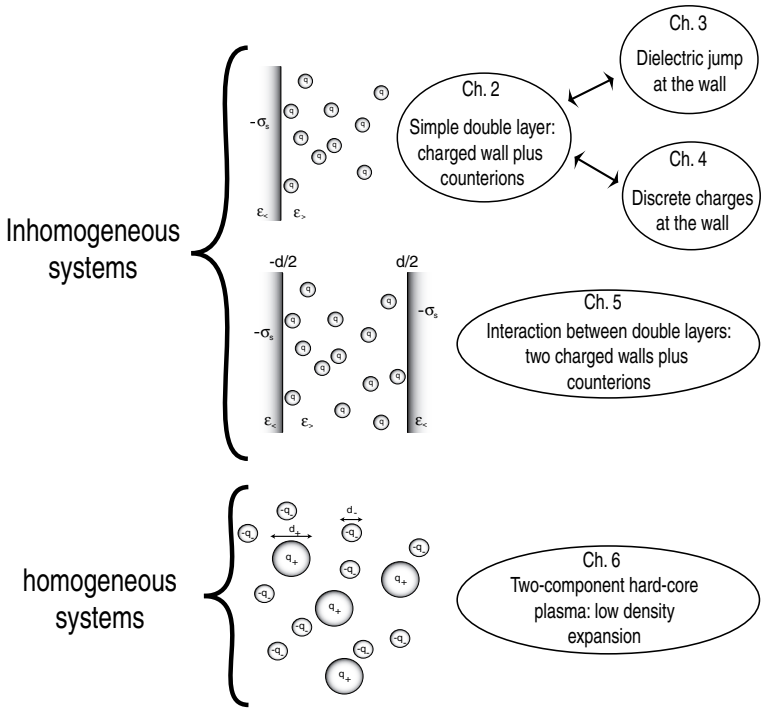

Figure 1.3: The relation between the various Chapters in this thesis.

We close this thesis in Chapter 7 with some final comments and prospective future work.

Chapter 2

Counterion distribution close to a charged wall

We study the simple double layer, composed by a charged wall in the presence of its counterions. The charges at the wall are smeared out and the dielectric constant is the same everywhere. The Poisson-Boltzmann (PB) approach gives asymptotically exact counterion density profiles around charged objects in the weak-coupling limit of systems with low-valent counterions, surfaces with low charge density and high temperature (or small Bjerrum length). Using Monte Carlo simulations, we obtain the profiles around the charged wall and compare it with both Poisson-Boltzmann (in the low coupling limit) and the novel strong coupling (SC) theory in the opposite limit of high couplings. In the latter limit, the simulations show that the SC leads in fact to asymptotically correct density profiles. We also compare the Monte Carlo data with previously calculated corrections to the Poisson-Boltzmann theory. Finally, we discuss in detail the methods used to perform the computer simulations.

2.1 Introduction

The ionic distribution close to a charged wall (electric double layer) is an old problem which has attracted attention in recent years[52]. The basic system consists of an impenetrable wall with a smeared out charge density σ_s in the presence of its counterions (with charge valence q) immersed in a solvent characterized by a certain dielectric constant (cf. Fig. 2.1). Some examples where the double layer problem is relevant can be found in biology (e.g. cell membranes are charged due to the phospholipids that compose it), in colloidal chemistry (the stability problem of lyophobic colloids[114]) or in interface physics[47].

The first approximate solution to this model was obtained by Gouy[37] and Chapman[20] using the Poisson-Boltzmann equation and point-like counterions, in a way similar to the one later used by Debye and Hückel to treat strong electrolytes[27]. This solution is asymptotically exact in the limit of weakly charged systems or at high temperatures, where the correlations between the counterions become less important, and a mean-field theory can be used to describe the system.

Since then, there have been various attempts to improve or correct the Poisson-Boltzmann (PB) solution[7, 14]. One old example is the concept of Stern layer[108], which assumes a

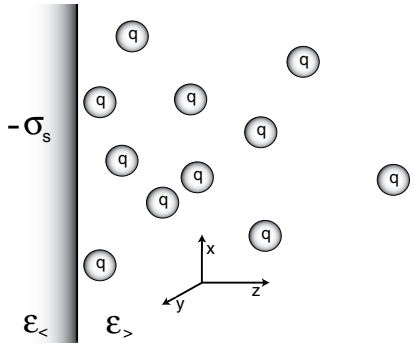

Figure 2.1: Schematic view of the semi-infinite charged wall with charge density σ_s and its counterions (with charge valence q) in solution; $\varepsilon_<$ and $\varepsilon_>$ are, respectively, the dielectric constant of the wall and of the solvent where the counterions are (in this Chapter we will only consider systems with $\varepsilon_< = \varepsilon_>$). The counterions cannot penetrate the wall.

layer of condensed counterions (with approximately 2 Å of thickness) in coexistence with non-condensed counterions, which would be described by the Poisson-Boltzmann equation. Liquid state theory[69, 43] has also been applied to these systems, especially with the hypernetted chain (HNC) closure relation, which has proved to be a very powerful technique regarding charged systems[11]. When applied to the double layer problem[54, 55, 84, 9], it yields numerical results that are in very good agreement with computer simulations[40, 15, 25, 53]. However, integral equation theories sometimes rely on numerical work and fail to provide an intuitive insight into the problem. More recently, there has been some interest in applying field-theoretic methods[61, 12] to charged systems. Perturbative field theory has been applied to study different aspects of these systems, ranging from the critical behavior of the Restricted Primitive Model[51, 17, 76] to the equation of state of a One-Component Plasma[16, 73]. Also the double layer has been tackled with these methods, as for instance, to study image-charge effects[81, 96], or to obtain corrections to Poisson-Boltzmann[83, 95].

In what follows we summarize the field-theoretic derivation[80] of an analytic expression for the counterion distribution which is asymptotically exact for systems with highly valent counterions and highly charged surfaces (strong coupling limit), complementing the Poisson-Boltzmann theory, which is valid in the opposite (weak coupling) limit. We also present in detail the computer simulations[74] performed to study the double layer and used to test the analytical results.

2.2 Poisson-Boltzmann and strong coupling

The starting point is the Hamiltonian of a system of N counterions,[1] each with charge valence q, at the half-space $z > 0$ in the presence of an oppositely charged hard-wall located at $z = 0$ with surface charge σ_s, viz.

$$\frac{\mathcal{H}}{k_B\,T} = \sum_{j=1}^{N-1}\sum_{k=j+1}^{N}\frac{q^2\,\ell_B}{|\mathbf{r}_j - \mathbf{r}_k|} + 2\pi q\ell_B\sigma_s\sum_{j=1}^{N} z_j, \tag{2.1}$$

[1] Without loss of generality, we always assume the counterions to be positively charged.

where

$$\ell_B \equiv e^2/4\pi\varepsilon k_B T \tag{2.2}$$

is the Bjerrum length (the distance at which two elementary charges interact with the same strength as the thermal energy, $k_B\,T$) and $\mathbf{r}_j = (x_j, y_j, z_j)$ is the position of counterion j. At this point we do not consider a possible difference in the dielectric constants of the hard-wall and of the solution (we will look at this in Chapter 3). The first sum in Eq. (2.1) corresponds to the interaction between counterions in solution, while the second one is the interaction between each counterion and the charged wall. The system is globally neutral, i.e. $\sigma_s = q\,N/A$, where A is the area of the wall. As usual, any effects coming from the lateral finite size of the wall are not taken into account in the Hamiltonian, since it is assumed that the system is very close to the thermodynamic limit ($N \to \infty$ and $A \to \infty$ with fixed σ_s).

It is convenient to define the Gouy-Chapman length $\mu \equiv 1/2\pi q\ell_B\sigma_s$, which is the distance at which a counterion interacts with the (unscreened) charged wall with the same strength as the thermal energy. If we rescale all lengths according to $\mathbf{r} = \widetilde{\mathbf{r}}\,\mu$, then the Hamiltonian Eq. (2.1) reads

$$\frac{\mathcal{H}}{k_B\,T} = \sum_{j=1}^{N-1}\sum_{k=j+1}^{N}\frac{\Xi}{|\widetilde{\mathbf{r}}_j - \widetilde{\mathbf{r}}_k|} + \sum_{j=1}^{N}\widetilde{z}_j. \tag{2.3}$$

Notice that after this rescaling, the Hamiltonian depends *explicitly* only on the coupling parameter

$$\Xi \equiv \frac{q^2\,\ell_B}{\mu} = 2\pi q^3\ell_B^2\sigma_s. \tag{2.4}$$

The Hamiltonian in rescaled units can give us some useful information about this system. The Monte Carlo simulations that we will present show that the typical distance between an ion and the charged wall is of the order of one Gouy-Chapman length, meaning that the binding energy per ion (cf. the second term in the rhs of Eq. (2.3)) is of the order of unity. In Fig. 2.2 we show the snapshots of Monte Carlo simulations for three different values of the coupling, viz. $\Xi = 0.1$, 10 and 10^4. For low coupling (Fig. 2.2a), the counterions distribute themselves in a diffuse cloud, and each counterion is surrounded in all directions by other counterions—a usual situation where mean-field theory yields good results. The typical distance between the counterions scales like $\Xi^{1/3}$, and the repulsion energy per pair goes like $\Xi^{2/3}$ (cf. the first term in the rhs of Eq. (2.3)), i.e., the repulsion between counterions becomes small (compared to the biding energy per ion), and the counterion distribution should be quite disordered. In the other limit, (Fig. 2.2c), the counterions orginize themselves in a two-dimensional layer close to the wall. Each counterion is laterally surrounded by other counterions, typically at a distance $\Xi^{1/2}$ away from each other. The repulsion energy per pair scales like $\Xi^{1/2}$, that is, it is now the dominant term in the energy. Note that here mean-field theory is expected to break down, since the ions are almost independent to move in the direction perpendicular to the wall, and are only confined by the linear potential due to the fixed smeared out charge distribution on the wall. In fact, the latter suggests that one should expect the counterion distribution perpendicular to the wall to decay like an exponential law (cf. barometric law) for large Ξ.

The partition function of a system of N counterions interacting through the Coulomb potential $v_c(\mathbf{r}) = \ell_B/r$ (in units of k_BT) with each other and with a fixed charge distribution $\sigma(\mathbf{r})$ is given

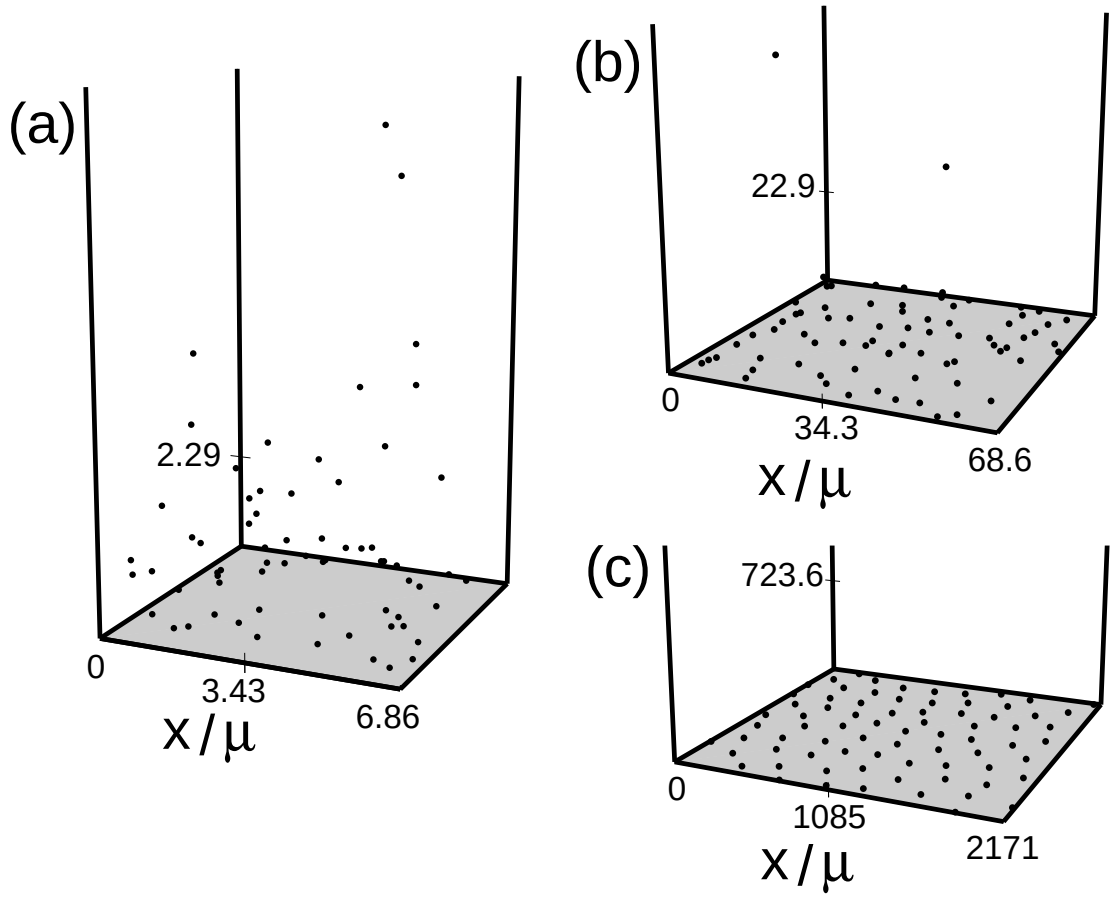

Figure 2.2: Snapshots of counterion distributions containing 75 particles for different values of the coupling constant Ξ: (a) weak coupling regime ($\Xi = 0.1$) where the Poisson-Boltzmann prediction is accurate; (b) intermediate coupling regime ($\Xi = 10$); (c) strong coupling regime ($\Xi = 10^4$). Notice that in (a) there are 8 particles located far away from the wall which are not shown.

by

$$\mathcal{Z} = \frac{1}{N!}\int \prod_{l=1}^{N} \mathrm{d}\mathbf{r}_l \exp\left(-q^2 \sum_{<jk>} v_c(\mathbf{r}_j - \mathbf{r}_k) - q\int \mathrm{d}\mathbf{r}\sigma(\mathbf{r}) \sum_j v_c(\mathbf{r} - \mathbf{r}_j) + \sum_j h(\mathbf{r}_j)\right) \quad (2.5)$$

where the sum over $< jk >$ corresponds to the sum over pairs of counterions and the field h has been added to calculate density distributions later on. The configurational integral is assumed to span the upper half-space only ($z > 0$). At this point we employ a Hubbard-Stratonovich transformation[36], which leads to

$$\mathcal{Z} = \frac{1}{N!}\int \frac{\mathcal{D}\phi}{\mathcal{Z}_v} \exp\left(-\frac{1}{2}\int \mathrm{d}\mathbf{r}\mathrm{d}\mathbf{r}'\phi(\mathbf{r})v_c^{-1}(\mathbf{r} - \mathbf{r}')\phi(\mathbf{r}') - \imath\int \mathrm{d}\mathbf{r}\sigma(\mathbf{r})\phi(\mathbf{r})\right)$$
$$\times \left[\int \mathrm{d}\mathbf{r} \mathrm{e}^{h(\mathbf{r}) - \imath q\phi(\mathbf{r})}\right]^N \quad (2.6)$$

where we introduced the notation $\mathcal{Z}_v = \sqrt{\det v_c}$. The inverse of the Coulomb potential, v_c^{-1}, is defined such that

$$\int \mathrm{d}\mathbf{r}'' v_c^{-1}(\mathbf{r}-\mathbf{r}'')\, v_c(\mathbf{r}''-\mathbf{r}') = \delta(\mathbf{r}-\mathbf{r}'). \tag{2.7}$$

Assuming the dielectric constant to be the same everywhere, the Coulomb potential obeys the Poisson law, viz.

$$\frac{k_B T \varepsilon}{e^2}\nabla^2 v_c(\mathbf{r}-\mathbf{r}') = -\delta(\mathbf{r}-\mathbf{r}'); \tag{2.8}$$

it follows from Eqs. (2.7) and (2.8) that $v_c^{-1}(\mathbf{r}) = -\nabla^2\delta(\mathbf{r})/4\pi\ell_B$.

For simplicity, we perform a Legendre transformation to the grand-canonical ensemble, $\mathcal{Q} = \sum_N \lambda^N \mathcal{Z}$, and thereby introduce the fugacity λ (exponential of the chemical potential). The grand-canonical partition function can therefore be written as

$$\mathcal{Q} = \int \frac{\mathcal{D}\phi}{\mathcal{Z}_v} \exp\!\left(-\int \mathrm{d}\mathbf{r}\left[\frac{[\nabla\phi(\mathbf{r})]^2}{8\pi\ell_B} + \imath\sigma(\mathbf{r})\phi(\mathbf{r}) - \lambda\theta(z)\mathrm{e}^{h(\mathbf{r})-\imath q\phi(\mathbf{r})}\right]\right) \tag{2.9}$$

where $\theta(z) = 1$ for $z > 0$ and zero otherwise. Next we rescale the action, similarly to our previous rescaling analysis of the Hamiltonian. All lengths are rescaled by the Gouy-Chapman length, $\mathbf{r} = \mu\tilde{\mathbf{r}}$, the fluctuating field is rescaled by the valence, $\phi = \bar{\phi}/q$. We also use the explicit form $\sigma(\mathbf{r}) = -\sigma_s\delta(z)$ (with $\sigma_s > 0$) for the fixed charge distribution. The result is

$$\mathcal{Q} = \int \frac{\mathcal{D}\bar{\phi}}{\mathcal{Z}_v} \exp\left(-\frac{1}{8\pi\Xi}\int \mathrm{d}\tilde{\mathbf{r}}\left[[\nabla\bar{\phi}(\tilde{\mathbf{r}})]^2 - 4\imath\delta(\tilde{z})\bar{\phi}(\tilde{\mathbf{r}}) - 4\Lambda\theta(\tilde{z})\mathrm{e}^{h(\tilde{\mathbf{r}})-\imath\bar{\phi}(\tilde{\mathbf{r}})}\right]\right) \tag{2.10}$$

where the rescaled fugacity Λ is defined by

$$\Lambda = 2\pi\lambda\mu^3\Xi = \frac{\lambda}{2\pi\ell_B\sigma_s^2}. \tag{2.11}$$

The expectation value of the counterion density, $\rho(\tilde{\mathbf{r}})$, follows[2] by taking a functional derivative with respect to the generating field h, $\rho(\tilde{\mathbf{r}}) = \delta\ln\mathcal{Q}/\delta h(\tilde{\mathbf{r}})\mu^3$, giving rise to

$$\frac{\rho(\tilde{\mathbf{r}})}{2\pi\ell_B\sigma_s^2} = \Lambda\langle\mathrm{e}^{-\imath\bar{\phi}(\tilde{z})}\rangle. \tag{2.12}$$

The normalization condition for the counterion distribution, $\mu\int\mathrm{d}\tilde{z}\rho(\tilde{z}) = \sigma_s/q$, which follows directly from the definition of the grand-canonical partition function, leads to

$$\Lambda\int_0^\infty \mathrm{d}\tilde{z}\langle\mathrm{e}^{-\imath\bar{\phi}(\tilde{z})}\rangle = 1. \tag{2.13}$$

This shows that the expectation values of the fugacity term in Eq.(2.10) is bounded and of the order of unity per unit area.

[2] In general one should represent the average density as $\langle\rho(\tilde{\mathbf{r}})\rangle$, the brackets representing thermal averages. In order to avoid a heavy notation, we do not use this here and ρ is to be understood as the thermal average (unless otherwise stated).

Let us first repeat the saddle-point analysis[83], which, because of the structure of the action in Eq.(2.10), should be valid for $\Xi \ll 1$. The saddle-point equation reads

$$\frac{\mathrm{d}^2\bar{\phi}(\tilde{z})}{\mathrm{d}\tilde{z}^2} = 2\imath\Lambda \mathrm{e}^{-\imath\bar{\phi}(\tilde{z})} \tag{2.14}$$

with the boundary condition $\mathrm{d}\bar{\phi}(\tilde{z})/\mathrm{d}\tilde{z} = -2\imath$ at $\tilde{z} = 0$. The solution of this differential equation is

$$\imath\bar{\phi}(\tilde{z}) = 2\ln\left(1 + \Lambda^{1/2}\tilde{z}\right) \tag{2.15}$$

while the boundary condition leads to $\Lambda = 1$, which shows that the saddle-point approximation is indeed valid in the limit $\Xi \ll 1$. Combining Eqs.(2.12) and (2.15), the density distribution of counter ions is given by the well-known Poisson-Boltzmann prediction

$$\frac{\rho(\widetilde{z})}{2\pi\ell_B\sigma_s^2} = \frac{1}{[1+\widetilde{z}]^2}. \tag{2.16}$$

This result is exact in the limit of vanishing Ξ. For a classical derivation of the Poisson-Boltzmann theory, see [114, 69].

Let us now consider the opposite limit, when the coupling constant Ξ is large[80]. In this case, the saddle-point approximation breaks down, since the pre-factor in front of the action in Eq.(2.10) becomes small. However, from the field-theoretic partition function Eq.(2.10), it is clear what has to be done in this limit. Since the fugacity term is bounded, as evidenced by Eq.(2.13), one can expand the partition function (and also all expectation values) in powers of Λ/Ξ. Upon Legendre transformation to the canonical ensemble, this gives the standard virial expansion. The normalization condition Eq.(2.13) can be solved by an expansion of the fugacity as $\Lambda = \Lambda_0 + \Lambda_1/\Xi + \cdots$, which leads to an expansion of the density profile with the small parameter $1/\Xi$. While the standard virial expansion fails for homogeneous bulk charged systems because of infra-red divergences, these divergences are renormalized for the present case of inhomogeneous distribution functions via the normalization condition Eq.(2.13). To leading order in this expansion, the rescaled density is

$$\frac{\rho(\widetilde{\mathbf{r}})}{2\pi\ell_B\sigma_s^2} = \Lambda \exp\left(-\frac{\Xi}{2}v_c(0) + \frac{1}{2\pi}\int \mathrm{d}\widetilde{\mathbf{r}}'\,\delta(\widetilde{z})\frac{1}{|\widetilde{\mathbf{r}}' - \widetilde{\mathbf{r}}|}\right), \tag{2.17}$$

where all lengths have been rescaled by μ. From the normalization condition Eq.(2.13) we obtain

$$\Lambda_0 = \exp\left(\frac{\Xi}{2}v_c(0) - \frac{1}{2\pi}\int \mathrm{d}\widetilde{\mathbf{r}}'\delta(z')\frac{1}{\widetilde{r}'}\right) \tag{2.18}$$

and thus to leading order the density distribution is given by

$$\frac{\rho(\widetilde{z})}{2\pi\ell_B\sigma_s^2} = \exp(-\widetilde{z}). \tag{2.19}$$

This is the exponential decay suggested by the previous scaling analysis of the Hamiltonian. Notice that this result is *exact* in the limit $\Xi \to \infty$. An exponential density profile (however with a different pre-factor) has also been obtained by Shklovskii[104] using an heuristic model for a

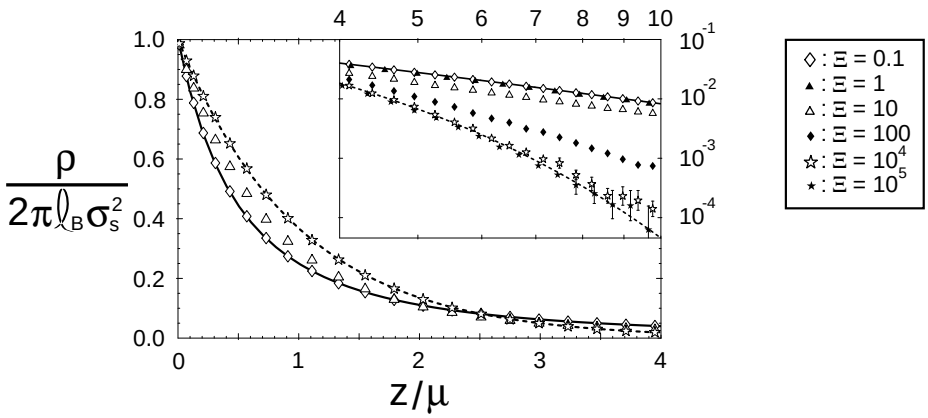

Figure 2.3: Rescaled counterion density distribution $\rho/2\pi\ell_B\sigma_s^2$ as a function of the rescaled distance $\widetilde{z} = z/\mu$ from the charged wall. The main figure shows Monte Carlo results for $\Xi = 0.1$ (open diamonds), $\Xi = 10$ (open triangles) and $\Xi = 10^4$ (open stars). The solid and the dashed lines denote the Poisson-Boltzmann and the strong coupling theory predictions, Eqs. (2.16) and (2.19) respectively. The inset shows a log-log plot of the density distribution at distances larger than $\widetilde{z} = 4$ for $\Xi = 10^5, 10^4, 100, 10, 1$ and 0.1 (from bottom to top). All simulations where performed with 75 particles and 10^6 Monte Carlo steps (we define what we call a step in Section 2.4), except the data for $\Xi = 0.1$ where 600 particles where simulated. Unless when explicitly shown, the error bars are comparable to or smaller than the symbols.

highly charged surface, where counterions bound to the wall are in chemical equilibrium with free ions.

We mention in passing that a similar exponential decay would also follow from the linearization of the Poisson-Boltzmann equation, very much in the spirit of Debye and Hückel[27]. The density profile in this case is given by

$$\frac{\rho(\widetilde{z})}{2\pi\ell_B\sigma_s^2} = 2\exp(-2\widetilde{z}). \tag{2.20}$$

However, this should be regarded as a coincidence: The Poisson-Boltzmann equation is only valid when Ξ is small; a linear approximation of the equation cannot describe better the behavior of the system than the full equation itself, especially for values of Ξ where the equation in expected to break-down.

2.3 Simulations: results

In this Section we present the results obtained from Monte Carlo simulations on the double layer, and compare them with the analytical results. The technical aspects concerning the simulations (calculation of the potentials, finite-size effects, etc.) are presented in the Section 2.4

2.3.1 Density profile

In Fig. 2.3 we show the Monte Carlo results for the average counterion density distribution for various values of Ξ, as well as the predictions from Poisson-Boltzmann (solid line) and strong coupling (dashed line). In the main graph ($\widetilde{z}$ between 0 and 4), open diamonds correspond to $\Xi = 0.1$, open triangles to $\Xi = 10$ and open stars to $\Xi = 10^4$. The error bars are comparable to or

smaller than the symbol sizes; the system with $\Xi = 0.1$ was simulated with $N = 600$, all others with $N = 75$. Note the very good agreement between Poisson-Boltzmann and strong coupling theory with the simulation results at low and high coupling, respectively. The inset in Fig. 2.3 shows Monte Carlos results for $\Xi = 10^5, 10^4, 100, 10, 1$ and 0.1 (from bottom to top) at larger distances from the wall (between 4 and 10 Gouy-Chapman lengths).

Previous computer simulations[111, 48] have also confirmed the validity of PB at the weak coupling regime. In fact, a picture that has emerged from previous studies is that PB is a good description for systems with monovalent counterions, but a poor description for systems with counterions with higher valence; deviations from the PB behavior can even lead to attraction between similarly charged plates[40] (see also Chapter 5). Eq. (2.4) gives us the clue to this: q has a power 3 in the expression for the coupling; if a system with monovalent ions has $\Xi \lesssim 1$, the same system with divalent ions will have a coupling 8 times larger! As is already clear from the simulation results Fig. 2.3, a system with $\Xi = 10$ clearly deviates from the PB curve in the vicinity of the wall.

The computer simulations done at high Ξ confirm the novel strong coupling limit as the correct asymptotic limit at infinite coupling. With this in mind, we can say that Fig. 2.3 presents a unified picture of the simple double layer problem (when only counterions are present): PB is the asymptotically correct as $\Xi \to 0$, SC is asymptotically correct as $\Xi \to \infty$, and any system with a Ξ between those limits will present a density profile that is between the power-law (PB) and the exponential decay (SC). Experimentally, a coupling of $\Xi = 100$—which is already quite close to the strong coupling regime—can be reached with divalent counterions for a surface charge density $\sigma_s \simeq 3.9$ nm^{-2}, which is feasible with compressed charged monolayers, and with trivalent counterions with $\sigma_s \simeq 1.2$ nm^{-2}, which is a typical value (cf. Table 2.1).

The rescaled densities as shown in Fig. 2.3 always fulfill

$$\frac{\rho(0)}{2\pi\ell_B\sigma_s^2} = 1. \tag{2.21}$$

This is a trivial consequence of the contact-value theorem[83, 47], which states that the value of the counterion density at contact with the wall $\rho(0)$ is related to the pressure P acting on the wall through

$$\frac{P}{2\pi\ell_B\sigma_s^2} = 1 - \frac{\rho(0)}{2\pi\ell_B\sigma_s^2}. \tag{2.22}$$

When in equilibrium, $P = 0$ and the result Eq. (2.21) follows. Incidentally, we remind that in Eq. (2.20) the density profile obtained through the linearized PB equation leads to a value of 2 for the rescaled density at contact, violating this theorem. We demonstrate the contact-value theorem in Appendix C; in Chapter 5 we will use it to calculate the pressure due to the counterions when they are confined between two similarly charged plates.

At very high couplings, one should expect a crystallization of the counterions into a Wigner crystal[77, 79]. A two-dimensional one-component plasma is known to crystallize at values of the plasma parameter $\Gamma \simeq 125$[11], which can be related to our coupling constant Ξ through $\Xi = 2\,\Gamma^2$, meaning that the Wigner crystal should be visible in the simulations at around $\Xi \simeq 31000$. In Fig. 2.4 we show the top view snapshots of two systems with high Ξ, one with $\Xi = 10^4$ (below crystallization) and another with $\Xi = 10^5$ (above crystallization). The latter shows, in contrast to the former, a clear two-dimensional ordering.

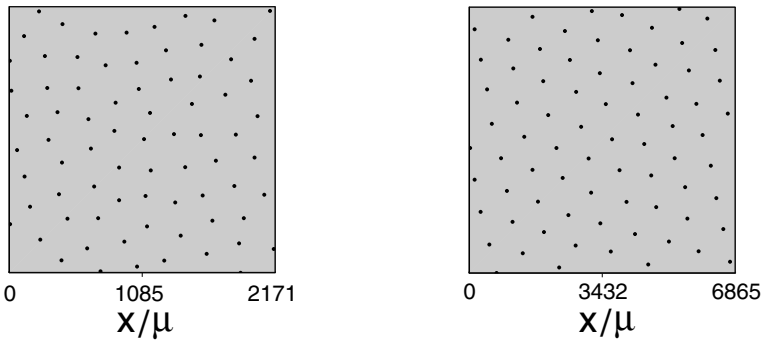

Figure 2.4: Top view snapshots of a system with $\Xi = 10^4$ (below the expected crystallization transition) and $\Xi = 10^5$ (above).

2.3.2 Two-dimensional pair distribution function

In Section 2.2 we showed that systems in the strong coupling regime exhibit a density profile that corresponds to a flat structure, in the sense that the average distance between neighboring counterions is much larger than the average distance between the counterions and the charged wall. Besides, as $\Xi \to \infty$, the repulsive interactions between counterions become dominant, and a counterion will be on average surrounded by other counterions in the direction parallel to the charged wall. Intuitively, one expects that a counterion will actually feel the surrounding counterions to act as a "cage", making any movement in the parallel direction very costly in the energetic point of view (hard-mode).

While this effect is already visible in the snapshots shown in Fig. 2.2, we can establish this more precisely by looking at the positional correlation between ions. Since this is essentially a two-dimensional effect, we look at the correlation function[6]

$$g_{2\mathrm{D}}(\widetilde{r}_{xy}) = \frac{A}{N^2}\Big\langle \sum_{<ij>} \delta(\widetilde{\mathbf{r}}_{xy} - \widetilde{\mathbf{r}}_{xy,i} + \widetilde{\mathbf{r}}_{xy,j})\Big\rangle \tag{2.23}$$

where $\sum_{<ij>}$ denotes a sum over pairs of particles, $\widetilde{\mathbf{r}}_{xy}$ is the two-dimensional vector $(\widetilde{x}, \widetilde{y})$ (with magnitude $\widetilde{r}_{xy}$) and $\widetilde{\mathbf{r}}_{xy,i}$ is the projection of the position of particle i into the xy plane. The function $g_{2\mathrm{D}}(\widetilde{r}_{xy})$ is the two-dimensional analog of the pair distribution function[69]. It gives the ratio between the probability of finding two counterions at distance $\widetilde{r}_{xy}$ and the expected probability for a homogeneous 2D gas with the same bulk density.

In Fig. 2.5 we show simulation results of $g_{2\mathrm{D}}(\widetilde{r}_{xy})$ for two particular systems, one with $\Xi = 0.1$ (away from the strong coupling regime) and another with $\Xi = 10^4$ (within the strong coupling regime, but still below crystallization). While in the former $g_{2\mathrm{D}}$ shows no spatial structure (except at very shot distances), the latter shows a clear depletion zone close to zero (few or no counterions are found at close distances), and an oscillatory behavior indicating a liquid-like two-dimensional positional order. The first peak gives the average distance between two neighboring counterions (the diameter of the aforementioned cage), which is approximately given by $\widetilde{r}_{typ} = 2/\sqrt{\pi\, N/A}$ or, when rescaled by μ,

$$\widetilde{r}_{typ} = 2\sqrt{2\,\Xi}, \tag{2.24}$$

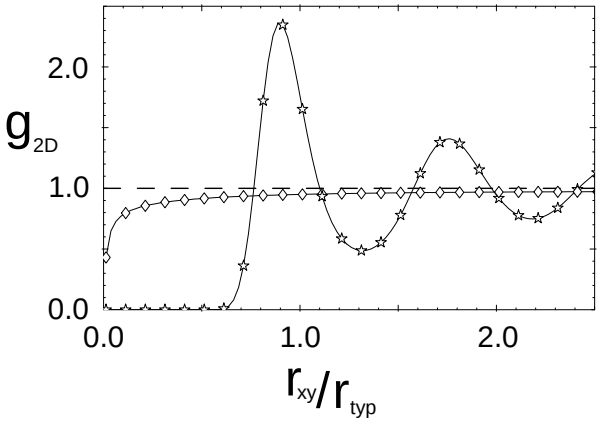

Figure 2.5: Two-dimensional pair correlation function for a system with $\Xi = 0.1$ (open diamonds) and $\Xi = 10^4$ (open stars), as a function of the xy projected distance between the ions $\widetilde{r}_{xy} = r_{xy}/\mu$; $\widetilde{r}_{typ} = 2/\sqrt{\pi\, N/A}$ is the distance expected between the particles for a homogeneous two-dimensional gas with N/A particles per unit area. The error bars are comparable to or smaller than the symbols.

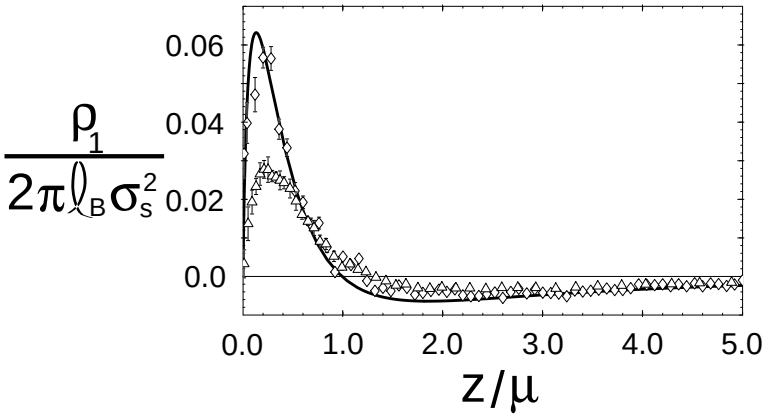

Figure 2.6: Comparison between the analytical prediction for the first correction to Poisson-Boltzmann and Monte Carlo results for $\Xi = 0.1$ (open diamonds, 600 particles and 10^6 MC steps) and $\Xi = 1.0$ (open triangles, 200 particles and 2×10^6 MC steps). Unless when explicitly shown, the error bars are comparable to or smaller than the symbols.

which is the distance expected between two neighboring particles in a two-dimensional homogeneous fluid (the area per particle is assumed to be a circle of radius $\widetilde{r}_{typ}$). This shows the cage effect when in the high coupling regime, and the idea that the parallel degrees of freedom become increasingly hard.

2.3.3 Corrections to Poisson-Boltzmann

As already discussed, the Poisson-Boltzmann theory corresponds to a saddle-point approximation which becomes exact at vanishing coupling. In fact, Ξ can be used as small parameter on a loop expansion around the saddle-point, leading to systematic corrections to it[83]. If one incorporates higher-order correction to the theory, how improved are the results when describing systems with finite, but small, Ξ?

The analytic expression of the one-loop correction to Poisson-Boltzmann for this particular geometry has been calculated in Ref. [83]. The corrected density profile reads

$$\rho(\widetilde{z}) = \rho_{PB}(\widetilde{z}) + \Xi\,\rho_1(\widetilde{z}) \tag{2.25}$$

where ρ_{PB} is the Poisson-Boltzmann result, Eq. (2.16), and ρ_1 is the one-loop correction to it (for the explicit expression, see Ref. [83]). In Fig. 2.6 we show the comparison between the analytical result for ρ_1 (full line) with the simulation results for $\Xi = 0.1$ and $\Xi = 1.0$. The points shown correspond to the function

$$\frac{1}{\Xi}\big(\rho(\widetilde{z}) - \rho_{PB}(\widetilde{z})\big) \tag{2.26}$$

where ρ is the density profile obtained from the simulations. In the regime where the one-loop correction is enough to correct the saddle-point result, the full line and the points should coincide. Notice that the function ρ_1 is very small, with a maximum value of 0.06 in a region where ρ_{PB} will be of the order of unity (in the rescaled units used here). Naturally, the prefactor Ξ in front of ρ_1 in Eq. (2.25) could be large enough so that this correction becomes important. But while for the system with $\Xi = 0.1$ the one-loop correction is enough to account for the (small) deviations between the simulation results and the PB result, already at $\Xi = 1$ it is clear that higher order corrections are necessary if one wishes to account for these deviations. In other words, in the region where the Ξ prefactor in Eq. (2.25) makes the one loop correction important is also the region that demands higher order corrections to the theory.

We should emphasize that this question is more of formal interest than of application. Even at $\Xi = 1$, where the one-loop is not enough to account for the differences between the MC and PB results, the relative correction to the PB density profile is of the order of 3%, meaning that PB is still a good description.

2.4 Simulations: technical aspects

2.4.1 Monte Carlo with periodic boundary conditions

We used the Monte Carlo method with Metropolis algorithm[70, 6] in order to study the thermal properties, in particular the density profile, of the electrical double layer.

We simulated systems with N point-like counterions (usually between 75 and 600) in a box of lateral size $\widetilde{L}$ with periodic boundary conditions in the directions parallel to the charged wall (x and y); in the direction z perpendicular to the wall the system is not periodic, and the ions are confined to the half-space which is not occupied by the wall (see Fig. 2.1). Although there were in the past some critique[112, 113] on the use of such boundary conditions for charged systems, it is now established[3] that this procedure yields very good results, provided that a suitable method is used to calculate the energy.

The typical run-time for the simulations was 10^6 Monte Carlo steps, where one step is defined as the sequence of attempts to move each counterion in the system from its present position to a new randomly chosen position according to the Monte Carlo recipe. In other words, one MC step is composed of N attempts to move the counterions from their positions. The ratio between the number of accepted moves and the total number of moves during a simulation (acceptance ratio) in

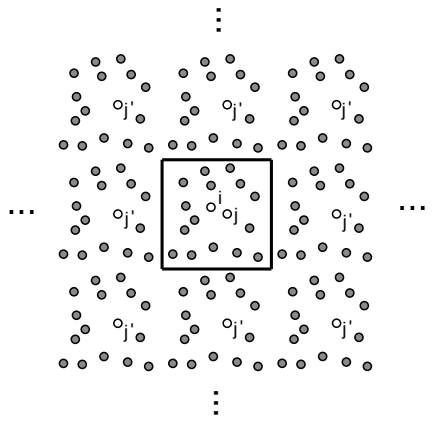

Figure 2.7: Schematic top view of the two-dimensional periodic boundary conditions used in the simulations to calculate the contribution to the electrostatic energy due to the interaction between ion j (and all its replicas) and ion i.

the simulations were always kept between 0.3–0.4, which is the usual rule-of-thumb for obtaining reasonable statistics. The systems were thermalized before any collection of data for averaging purposes was taken.

The two-dimensional periodicity of the box is in fact using the intrinsic symmetry of the problem in order to compensate for the finite size of the simulated systems and prevent artificial surface effects. The systems in the computer are globally neutral, i.e., the total positive charge equals the total negative charge, which means that the box sizes used do depend on the number of counterions in the simulations. It is easy to show that, for a system with coupling constant Ξ and N counterions, the lateral box size in rescaled units should be

$$\widetilde{L} = \frac{L}{\mu} = \sqrt{2\,\pi\,N\,\Xi} \tag{2.27}$$

so that electroneutrality is fulfilled.

2.4.2 The Lekner potential

Whenever calculating the force (or the potential) exerted by, say, particle j on particle i, one has to calculate not only the contribution coming from the pair in the central box (cf. Fig. 2.7), but also the contributions coming from all the replicas of particle j in the "virtual" simulation boxes (in principle infinite in number) around the central box. The replicas of particle i do not contribute to this, provided that the interaction potential between the particles is spherically symmetric. However, for most short-ranged potentials there is no need to account for the contributions of the neighboring boxes (except for particles close to the edges of the central box) since, in general, it is enough to have a box size a few times larger than the range of the interaction in order to avoid finite-size effects.

For ionic systems, the contributions coming from the replicas in the neighboring boxes cannot be neglected. The Coulomb potential is long-ranged, i.e., it is a power-law decaying like $1/r$ (where r is the distance between two interacting particles) and in the thermodynamic limit the coupling between parts of the system at large distances contribute non-vanishingly to the total

energy. Nevertheless, as long as electroneutrality holds, the energy per particle will always be bounded from below.

In a periodic system the electrostatic energy is

$$\frac{E_{el}}{k_BT} = \sum_{<ij>} q_i\, q_j\, \ell_B \sum_{\mathbf{n}} \frac{1}{|\mathbf{r}_i - \mathbf{r}_j + \mathbf{n}|}, \tag{2.28}$$

where the sum over $\mathbf{n}$ refers to all boxes—the central one and its infinite replicas—and the one over $<ij>$ refers to the sum over pairs of particles ($i \neq j$), one located at $\mathbf{r}_i$ and the other at $\mathbf{r}_j$. With a spherically symmetric potential, the influence of the replicas of a particle over itself is zero. This sum includes *all* charged particles in the system, i.e., it is extended to a region that is globally neutral.

In the computer, the sum over $\mathbf{n}$ has to be at some point truncated. It is then desirable to transform it into a fast converging series, so that the number of terms to be summed before a reliable truncation is not too big and the computations can be performed reasonably fast. A popular way to achieve this is known as the Ewald summation[31, 26, 3, 6, 113], first introduced in the context of ionic crystals. Here we use a different method introduced by Lekner[62, 63, 110] and Sperb[107]. The main reason is that the use of the Ewald summation for systems with two-dimensional periodicity (in contrast to crystals, with periodicity in all three dimensions) requires some modifications to the original method[45, 110], and only works if the ions are confined to a thin layer in the z direction. The Lekner-Sperb method is general, and is particularly suited for systems with 2D symmetry[24]. A comparison between the two methods in a system with 3D symmetry can be found in Ref. [57], and for a system with 2D symmetry in Ref. [110]. We now demonstrate Lekner's formula for the electrostatic energy, and apply it to the the case of one plane in the presence of its counterions.

Let us assume that the simulation box has lateral size L. Due to electroneutrality, the sum Eq. (2.28) exists, and can be rewritten as

$$\frac{E_{el}}{k_BT} = E_0 + \frac{\ell_B}{2L} \int \mathrm{d}\mathbf{r}\mathrm{d}\mathbf{r}' \hat{\rho}_c(\mathbf{r}) v_L(\mathbf{r}, \mathbf{r}') \hat{\rho}_c(\mathbf{r}') \tag{2.29}$$

where

$$E_0 = -\frac{\ell_B}{2L} \sum_i q_i^2 v_L(\mathbf{r}_i, \mathbf{r}_i) \tag{2.30}$$

is the self-energy of each particle in the system and

$$\hat{\rho}_c(\mathbf{r}) = \sum_i q_i \delta(\mathbf{r} - \mathbf{r}_i) \tag{2.31}$$

is the charge distribution of point charges, generalizable to any distribution. $v_L(\mathbf{r}, \mathbf{r}')$ is the potential at the point $\mathbf{r}$ due to the charge distribution at $\mathbf{r}'$ and its infinite replicas in x and y direction, given by

$$v_L(\mathbf{r}, \mathbf{r}') = \sum_{l,m=-\infty}^{+\infty} \frac{1}{\sqrt{[\xi + l]^2 + [\eta + m]^2 + \zeta^2}} \tag{2.32}$$

where we defined

$$\xi = \frac{|x-x'|}{L},\ \ \eta = \frac{|y-y'|}{L},\ \ \zeta = \frac{|z-z'|}{L}. \tag{2.33}$$

This sum has to be handled with care, since its is divergent. To deal with it, we sum and subtract the value of v_L for a reference state (which we do not have to specify) with $\xi = \alpha_1$, $\eta = \alpha_2$ and $\zeta = \alpha_3$, and rewrite v_L as

$$v_L(\mathbf{r},\mathbf{r}') = v_L(0) + \sum_{l,m=-\infty}^{+\infty} \frac{1}{\sqrt{[\xi+l]^2+[\eta+m]^2+\zeta^2}} - \sum_{l,m=-\infty}^{+\infty} \frac{1}{\sqrt{[\alpha_1+l]^2+[\alpha_2+m]^2+\alpha_3^2}}. \tag{2.34}$$

The term $v_L(0)$ is the value of v_L for the reference state, which is divergent, but the difference between the two infinite sums is a well defined quantity. Following Lekner[63], we show in Appendix A that v_L can be transformed into the function

$$v_L(\mathbf{r},\mathbf{r}') = v_L(0) + C - \ln\Big(\cosh(2\pi\zeta) - \cos(2\pi\eta)\Big) + s(\xi,\eta,\zeta) \tag{2.35}$$

where s is the (fast converging) series

$$s(\xi,\eta,\zeta) = 4\sum_{l=1}^{\infty}\cos(2\pi l\xi)\sum_{m=-\infty}^{+\infty} K_0\Big(2\pi l\sqrt{[\eta+m]^2+\zeta^2}\Big) \tag{2.36}$$

and C is a constant that depends on the reference state, given by

$$C = \ln\Big(\cosh(2\pi\alpha_3) - \cos(2\pi\alpha_1)\Big) - s(\alpha_1,\alpha_2,\alpha_3). \tag{2.37}$$

Eq. (2.35) is not only more manageable for calculations than Eq. (2.34): it also converges faster, and the sums can be typically truncated after a few terms. We will come back to this point later.

For the system of counterions in the presence of the charged wall we can write the charge distribution $\hat{\rho}_c$ as

$$\hat{\rho}_c(\mathbf{r}) = q\sum_{i=1}^{N}\delta(\mathbf{r}-\mathbf{r}_i) - \sigma_s\delta(z)\Theta_0^L(x)\Theta_0^L(y) \tag{2.38}$$

where $\Theta_0^L(x) = 1$ if $0 < x < L$, and 0 otherwise. This corresponds to the charge distribution within the simulation box, and the electroneutrality condition implies that $\int \mathrm{d}\mathbf{r}\hat{\rho}_c(\mathbf{r}) = 0$, i.e., $\sigma_s = qN/L^2$. Using Eqs. (2.38) and (2.35) in the electrostatic energy Eq. (2.29) we arrive, after some algebra, to the formula

$$\frac{E_{el}}{k_BT} = \frac{q^2\ell_B}{L}\sum_{<ij>}\widetilde{v}_L(\xi_{ij},\eta_{ij},\zeta_{ij}) + 2\pi q\ell_B\sigma_s\sum_{i=1}^{N} z_i - \frac{\ell_B q^2N^2}{2L}\int_0^1 \mathrm{d}\xi\,\mathrm{d}\,\eta\ \widetilde{v}_L(\xi,\eta,0) + Nu_0, \tag{2.39}$$

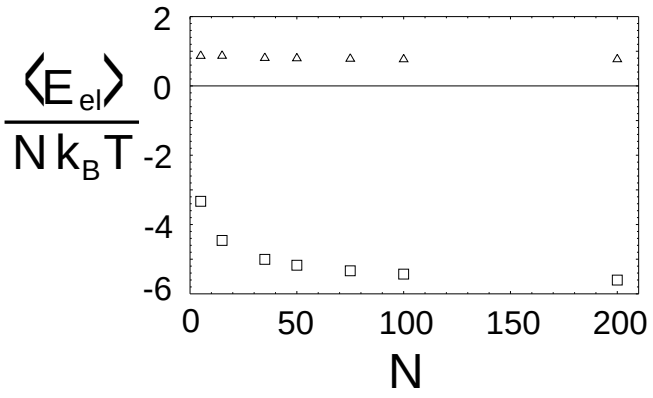

Figure 2.8: Average energy per particle for $\Xi = 1.0$ (open triangles) and $\Xi = 100$ (open squares) as a function of N, the number of counterions in the simulation. The error bars are comparable to or smaller than the symbols.

where $\xi_{ij} = |x_i - x_j|/L$ (with similar definitions for η_{ij} and ζ_{ij}) and

$$\widetilde{v}_L(\xi,\eta,\zeta) \equiv -\ln\Big(\cosh(2\pi\zeta) - \cos(2\pi\eta)\Big) + s(\xi,\eta,\zeta). \tag{2.40}$$

u_0 is the energy needed to construct one particle (self-energy), and is irrelevant here. The integral over $\widetilde{v}_L$ in Eq. (2.39) can be done and leads to

$$\int_0^1 \mathrm{d}\xi\,\mathrm{d}\eta\,\widetilde{v}_L(\xi,\eta,0) = \ln(2). \tag{2.41}$$

Rescaling all lengths with the Gouy-Chapman length as previously done, we finally get

$$\frac{E_{el}}{k_B T} = \frac{\Xi}{\widetilde{L}} \sum_{<ij>} \widetilde{v}_L(\xi_{ij},\eta_{ij},\zeta_{ij}) + \sum_{i=1}^{N} \widetilde{z}_i - \frac{\ln(2)}{2\sqrt{2\pi}}\sqrt{\Xi} N^{3/2} \tag{2.42}$$

which is the electrostatic energy of the simple double layer with periodic boundaries. Notice that we neglected the self-energy of the particles, and that a constant term $c\,N$ can be added to E_{el} without changing the thermodynamic properties of the system. This is the definition we use to calculate the electrostatic energy for each trial configuration in the computer simulations. The first term corresponds to the interaction between the counterions and the second term to the interaction between the counterions and the charged wall. The third term is the self-energy of the charged wall with size $L \times L$, which is a constant and irrelevant when N is fixed. This term is important only when calculating the thermodynamic energy per particle.

For calculating the counterion–counterion interaction we use the formula in Eq. (2.40), which is in general quite efficient, since the sum s can be truncated after a few terms due to the behavior of Bessel function at large arguments, viz. $K_0(x) \sim \exp x/\sqrt{x}$ as $x \to \infty$. However, the Bessel function diverges as its argument becomes small, and the sum s can be very inefficient for small

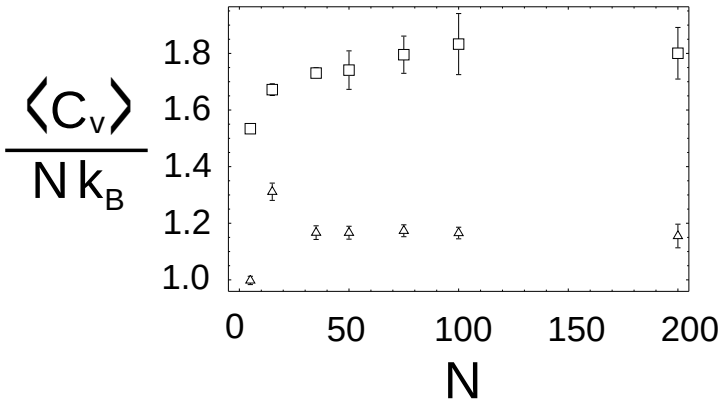

Figure 2.9: Specific heat per particle for $\Xi = 1.0$ (open triangles) and for $\Xi = 100$ (open squares) as a function of N, the number of counterions in the simulation. Unless when explicitly shown, the error bars are comparable to or smaller than the symbols.

$\sqrt{\eta^2 + \zeta^2}$. To solve this, Sperb[107] proposes the following transformation

$$4\sum_{l=1}^{+\infty}\cos(2\,\pi\,l\,\xi)K_0(2\,\pi\,l\,\varrho) = -1.386294 + 2\,\ln(\varrho) + \frac{1}{\sqrt{\xi^2+\varrho^2}} - \Psi(1+\xi) - \Psi(1-\xi) + \sum_{l=1}^{+\infty}\binom{-1/2}{l}\varrho^{2\,l}\big[Z(2\,l+1,1+\xi) + Z(2\,l+1,1-\xi)\big], \quad (2.43)$$

where Ψ is the digamma function and Z is the Hurwitz zeta function[2], and $\varrho = \sqrt{[\eta+m]^2+\zeta^2}$. This series converges very quicky if ϱ is small, provided that $\xi < 1/2$. When calculating the sum s in our simulation, we have included typically 5 to 7 terms in the sum in m, and used to following rule for the sum in l: if $\varrho > 3$, then we sum only three terms in l; if $1/3 < \varrho < 3$, we sum $2 + \mathrm{Integer}\big[3/\sqrt{\eta^2+\zeta^2}\big]$ terms in Lekner's formula; if $\sqrt{\eta^2+\zeta^2} < 1/3$, we use Sperb's formula (with 8 terms) in place of Lekner's. This is a conservative approach, but nevertheless we do not have to sum more than eleven terms in the l index. One can show that with this recipe the truncation error in the sums are (in absolute value) equal to or smaller than than approximately 10^{-11}.

One way to test the Lekner summmation is to look at the behavior of the average electrostatic energy. In Fig. 2.8 we show the average energy per particle obtained from Monte Carlo simulations for two couplings, viz. $\Xi = 1$ and $\Xi = 100$, as a function of the number of counterions N. This is the energy given by Eq. (2.42) (per particle) averaged over the trial configurations tested by the computer in the course of the simulations. As expected, after a certain critical size the energy per particle becomes constant. Notice that the thermodynamic energy per particle is equal to the values obtained from the simulation plus a constant (which is independent of N or Ξ) that we neglect.

Another way to test the formula Eq. (2.42) is by looking at the fluctuations of the energy around its average. This is in fact an useful quantity, since it can be related to the specific heat of

the system through the fluctuation-dissipation theorem[6]

$$C_v = k_B \Big\langle \big(\frac{\delta E_{el}}{k_B T}\big)^2 \Big\rangle \tag{2.44}$$

where the brackets $\langle\,\rangle$ denote the average over the trial configurations, and δE_{el} are the fluctuations around the total electrostatic energy, viz.

$$\delta E_{el}(t) = E_{el}(t) - \langle E_{el} \rangle \tag{2.45}$$

at a certain MC step t. In our case, the C_v calculated from the fluctuations is what one could call the "excess" specific heat, since the ideal gas contribution $C_{v,id} = 3N/2$ (in units of $k_B T$) has to be added to it in order to obtain the total specific heat. In Fig. 2.9 we show C_v/N obtained from the same simulations as in Fig.2.8, viz. $\Xi = 1$ and 100 as a function of N. As expected, C_v/N also becomes independent of N after a critical size of the system. As a side note, the value of C_v of the system with $\Xi = 1$ is close to unity, which is the value predicted by the Poisson-Boltzmann theory.

2.4.3 Binning

In order to measure the density profiles, we used particle-number histograms in the course of the simulations, from which the averages were obtained. This basically consists on dividing the half-space (where the counterions are) in bins of a certain size and counting how many particles are inside each bin. In the simulations discussed in this Chapter, we had typically 500 bins between $\widetilde{z} = 0$ and $\widetilde{z} = 10$, i.e., each with size 0.02μ.

2.4.4 Error-bars

The error-bars for each of the measured quantities in the simulations were obtained according to the block-averaging method[6, 33], which can be understood as follows: assume we run a simulation from $t = 0$ to $t = t_d$ (decade time in MC steps), and that we keep the value of the observable $X(t)$ at each step. If we divide the decade time into n parts (or "blocks", usually 10), then

$$X_i = \frac{n}{t_d} \sum_{j=[i-1]\,t_d/n}^{i\,t_d/n-1} X(j) \tag{2.46}$$

is the average value of X for the block i (indexed from 1 to n). It follows from this definition that the average value of X for the decade is the average over blocks, i.e.,

$$\bar{X} = \frac{1}{n} \sum_{i=1}^{n} X_i. \tag{2.47}$$

We run the program for t_d MC steps and calculate the error-bars for this decade through the dispersion on the average block-values of X, viz.

$$\frac{\Delta \bar{X}}{2} = \sqrt{\frac{1}{n} \sum_{i=1}^{n} (X_i - \bar{X})^2}. \tag{2.48}$$

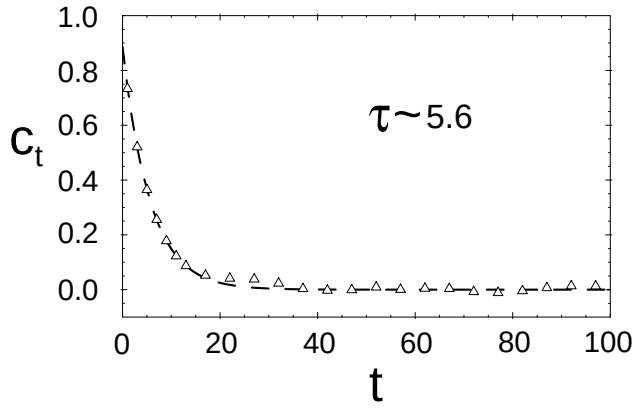

Figure 2.10: The typical time correlation function for one bin in the simulations. In this example, this is $c(t)$ for the bin number 25 (at distance 0.5μ away from the wall) for a system with 75 particles and $\Xi = 10$. The correlation initially decays exponentially (in this case $0.88\exp(-t/5.6)$), and later fluctuates around zero. Notice that $c(t)$ has not been normalized to $c(0)$ (self-correlation).

After this, we run the program for a decade of size $t'_d = n\,t_d$; the average value of X in the decade t_d becomes the average of X in the block $i = 1$ of the decade t'_d. This procedure is done recursively until the end of the simulation. For example: if a simulation is run for 10^6 steps (with $n = 10$), and we start this procedure for a minimum block size of $t = 10^3$, then we get error-bars for $t_d = 10^4$ and block size 10^3, for $t_d = 10^5$ and block size 10^4 and $t_d = 10^6$ and block size 10^5.

We use only the error-bars from the last decade. In effect, and coming back to the example above, this is the same as running 10 simulations of 10^5 MC steps and looking at the dispersion on the averages obtained. However, the information provided by the smaller decades tell us already something about how much we can trust the final error-bars. In fact, if the block sizes are very small, the $X(t)$ are highly correlated and the error-bars obtained through the block averages will also be very small; as the blocks become larger, the error-bars also increase, until the block sizes are so large that they become totally decorrelated, and the error-bars again decrease. We have observed this behavior in our simulations, and so the error-bars used are in principle reliable.

There is however another way to test whether the block sizes used for obtaining the error-bar are big enough to be regarded as independent. We looked at the time correlation function for some of the bins used to calculate the average density profile of the counterions. The time correlation function is defined as[33]

$$c_t = \frac{1}{t_{tot} - t} \sum_{i=1}^{t_{tot}-t} [X(i) - \bar{X}]\,[X(i+t) - \bar{X}]. \tag{2.49}$$

In this case, the variable X is the number of particles in a certain bin. In Fig. 2.10 we show the typical behavior of $c(t)$, in this case for the bin number 25 (i.e., at distance 0.5μ from the wall) of a system with 75 particles and $\Xi = 10$. The points are simulation results, and the dashed line is a curve of the form $\alpha\exp(-t/\tau)$. At first, the number of particles inside this bin during the successive steps are highly correlated; this correlation, however, decays exponentially, and later (in this example already after 40 Monte Carlo steps) $c(t)$ just fluctuates around zero. The decay time τ is a measure of how many steps the system needs to take so that it becomes uncorrelated:

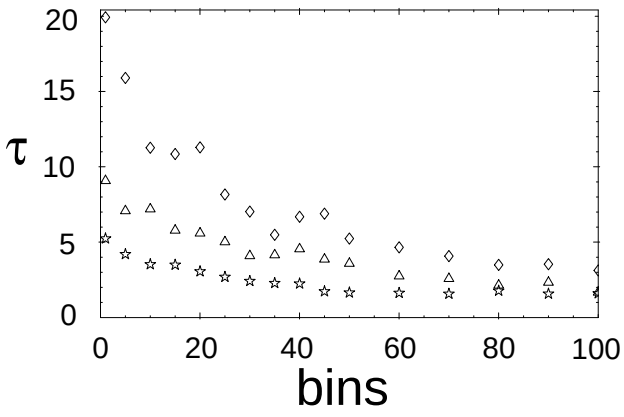

Figure 2.11: Simulation results for the correlation times as a function of the distance from the wall. We measured $c(t)$ for $\Xi = 0.1$ and 600 particles (open diamonds), $\Xi = 10$ and 75 particles (open triangles) and $\Xi = 10^4$ and 75 particles (open stars). The points shown correspond to the bins that measure the number of counterions in the first 2μ close to the charged wall.

if the previously mentioned block sizes are much bigger than this time, then one should expect the blocks to be statistically independent from each other.

In Fig. 2.11 we show the correlation times obtained for $\Xi = 0.1$, $\Xi = 10$ and $\Xi = 10^4$ (some of the simulations presented earlier in Fig. 2.3) as a function of the distance from the charged wall. It is then clear that the blocks of size 10^5 used to calculate the error-bars were much larger than the correlation times—the blocks can be regarded as independent. It is also interesting to notice that the systems with larger Ξ show smaller correlation times for the particle-number bins. While this is probably influenced by the number of particles in the simulation (remember that the simulation with $\Xi = 0.1$ shown was performed with 600 particles), the systems with $\Xi = 10$ and $\Xi = 10^4$ shown in this figure have the same number of particles, and direct comparison can be made. The smaller correlation times indicate that particles have more freedom to move around—this is another indication that, as Ξ grows, moves in the direction perpendicular to the charged wall become easier.

2.4.5 Finite-size effects

Any computer simulation has, for practical reasons and technological limitations, much less particles than what is typical for a macroscopic piece of matter (with the usual 10^{23} particles). The periodic boundary conditions and the Lekner potential partially correct this fact. However, one should test whether or not the number of particles used in the simulations yields results that are at least consistent, i.e., results that do not change as the number of particles change.

In Fig. 2.12 we show the density profile of a system with $\Xi = 0.1$ and $N = 5$, 15, 35 and 600 particles. As it is clear from this figure, already at 35 particles the resulting profile is close to the profile for 600 particles. From this one concludes that the results for 35 particles is close to the thermodynamic limit, as far the density profile is concerned, and as long as one believes in the self-consistency of the Monte Carlo results. Finite-size effects become less important as Ξ grows, which is not surprising: remember that the box size is related to the number of particles and the coupling through $\widetilde{L} = \sqrt{2\pi N \Xi}$.

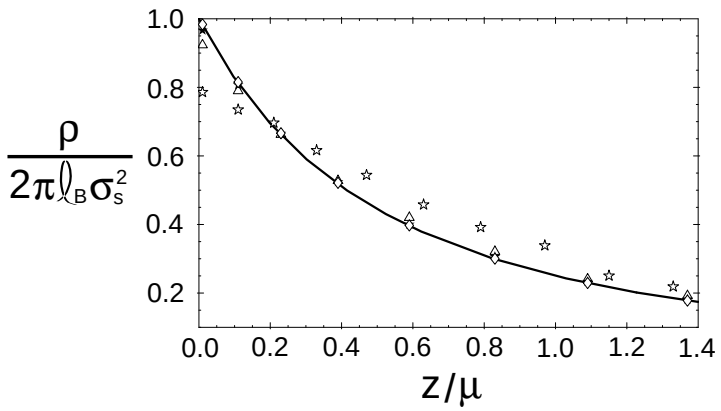

Figure 2.12: Results for the rescaled counterion density distribution as a function of the rescaled distance from the wall for $\Xi = 0.1$ and 5 particles and 10^8 MCS (open stars), 15 particles and 10^7 MCS (open triangles), 35 particles and 10^7 MCS (filled stars) and 600 particles and 10^6 MCS (open diamonds). Notice that finite-size effects almost negligible for 35 particles (in comparison to 600), and that the system with 15 particles is already quite close to the large-N behavior. For systems with larger Ξ this effect is even stronger. The error bars are comparable to or smaller than the symbols.

When testing the corrections to Poisson-Boltzmann (cf. Section 2.3.3), we have noticed that the simulations are more sensitive to finite-size effects at low values of Ξ. In Fig. 2.6 we have shown the simulation results as compared to the analytical prediction to the first correction to Poisson-Boltzmann. In Fig. 2.13, we show this graphic again, but now for systems with different sizes. As we see, while for $\Xi = 1$ the simulations with 75 and 200 particles yield the same correction, for $\Xi = 0.1$ we had to go up to 600 particles in order to avoid finite-size effects. For this latter we needed the (non-negligible) CPU time of approximately 830 hours, or 34.6 days, in machines with Alpha EV67/667, Alpha EV6/500 or R10000/225 processors. This long running time is a consequence of the heavy calculations, viz. square roots and Bessel functions, involved in the Lekner summation.

2.5 Conclusions

We have presented the Monte Carlo simulations obtained for the system composed by a charged wall in the presence of its counterions. This simple system is characterized by one explicit parameter $\Xi = 2\pi q^3 \ell_B^2 \sigma_s$: we presented the analytical results for the two limiting behaviors, viz. the time-honored Poisson-Boltzmann theory which is exact in the limit $\Xi = 0$ and the novel strong coupling theory[80], which is asymptotically exact in the limit $\Xi \to \infty$. Both limits were confirmed through extensive Monte Carlo simulations. The question that now arises is: how relevant are the results shown here?

In the theoretical point of view, having the two possible limiting behaviors of the system helps in many ways. Any computer simulation or approximate solution to the simple double layer leads necessarily to a counterion density distribution that lies between PB and SC. Having the analytic solutions for the two extreme cases is helpful when doing numerics, since one knows what to expect from the results. The computer simulations together with the analytical results give a fairly complete and unified picture of the simple double layer.

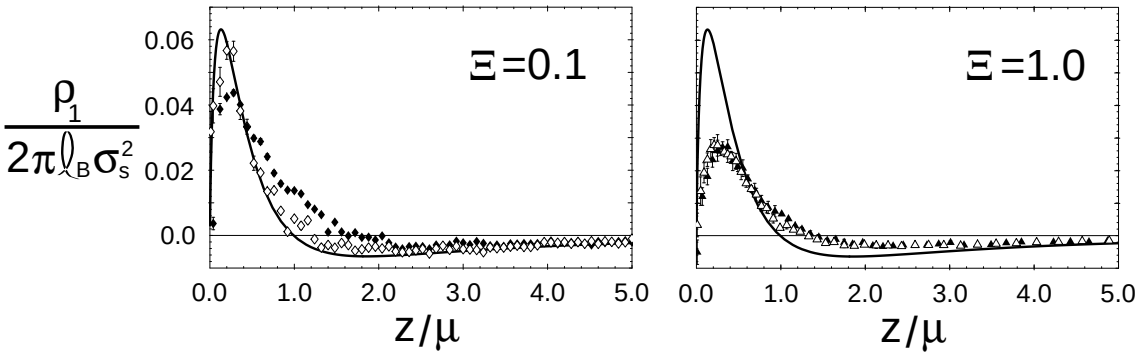

Figure 2.13: Finite-size effects on the first correction to Poisson-Boltzmann. For $\Xi = 0.1$, the systems simulated had 200 particles and 5×10^6 MCS (filled diamonds) and 600 particles and 10^6 MCS (open stars). For $\Xi = 1.0$, the systems simulated had 75 particles and 5×10^6 MCS (filled triangles) and 200 particles and 2×10^6 MCS (open triangles). Unless when explicitly shown, the error bars are comparable to or smaller than the symbols.

In Table 2.1 we show for some Ξ and q the corresponding values of the surface charge density σ_s, the Gouy-Chapman length μ and the distance between neighboring ions fixed at the wall (we will use this information later, when looking at systems with discrete charges fixed at the wall, instead of a smeared out distribution). From the surface charge density we can assess the experimental feasibility of a system: for instance, to get $\Xi = 100$ with monovalent counterions one would need a charge density at the wall corresponding to one e per 3.2 Å^2, which is in principle very difficult to realize experimentally. On the other hand, the same coupling can be achieved with divalent ions and compressed monolayers. With trivalent counterions the charge density needed at the wall to get $\Xi = 100$ is relatively low and easily realizable experimentally.

From the values of the Gouy-Chapman length one can check to which extend the ionic sizes matter for a certain system. Ions in solution are in general larger than their bare size due to the hydration shell[47]. In general, ions like Cl^-, Na^+, K^+ have hydrated radii between 2 and 3 Å (the former value determined in Section 6.3.2 using the activity coefficient of salts), and for Ca^{2+} a radius between 4 and 6 Å. The question is: when is it reasonable, in the context of the double layer, to assume the ions to be point like?

The counterion density profiles obtained have the typical decay length of μ. This means that if the ions are bigger than or of the order of the Gouy-Chapman length, one should expect packing effects to become important. But one should also distinguish the two physical situations corresponding to the high and to the low coupling regimes. According to Fig. 2.2, if the system has a low coupling, the counterions have a three dimensional spatial distribution, and one has to compare the ionic size with the typical distance between particle within the layer of one μ away from the wall—half of the counterions find themselves within this layer, as one can conclude by integrating Eq. (2.16) for $\widetilde{z}$ between 0 and 1. The typical distance is approximately $\widetilde{r}_{typ} = 2[3\Xi]^{1/3}$, which means that for $\Xi = 1$, $r_{typ} \simeq 2.9\mu$; if $\mu = 7.15$ Å (monovalent counterions, see Table 2.1), then the ions in the first layer will be typically 20 Å away from each other, well above the typical ionic size. In other words, for the systems in the first row in Table 2.1, the assumption of point-like counterions is good enough.

If the system has a high coupling (and for this matter $\Xi = 10$ is already high enough, see Fig. 2.2b), the charges will prefer to be organized in a two dimensional layer close to the wall: the

	$q=1$	$q=2$	$q=3$
$\Xi=1$	$\sigma_s=1/321.2$ $\mu=7.15$ $a=17.9$	$\sigma_s=1/2569.7$ $\mu=28.6$ $a=50.7$	$\sigma_s=1/8672.7$ $\mu=64.4$ $a=93.1$
$\Xi=10$	$\sigma_s=1/32.1$ $\mu=0.715$ $a=5.7$	$\sigma_s=1/256.9$ $\mu=2.86$ $a=16.0$	$\sigma_s=1/867.2$ $\mu=6.44$ $a=29.4$
$\Xi=100$	$\sigma_s=1/3.21$ $\mu=0.07$ $a=1.8$	$\sigma_s=1/25.7$ $\mu=0.3$ $a=5.1$	$\sigma_s=1/86.7$ $\mu=0.6$ $a=9.3$

Table 2.1: The surface charge density (σ_s, in Å^{-2}), Gouy-Chapman length (μ, in Å) and the distance between neighboring ions at the wall (a, in Å) for different values of the coupling and the valence of the counterions. In all cases, the Bjerrum length ℓ_B was assumed to be 7.15 Å, which is its approximate value in water at 25 C. Notice that the Gouy-Chapman length can be independently fixed (can be made larger or smaller) by changing the value of ℓ_B.

typical distance between the ions is approximately given by $\widetilde{r}_{typ}=2\sqrt{2\Xi}$. For $\Xi=10$, $r_{typ}\simeq 9\mu$, meaning that for a $\mu=0.7$ Å (monovalent counterions, see Table 2.1) the ions are at (laterally) ~ 6 Å away from each other, and for $\mu=2.9$ Å (divalent counterions) the ions are at lateral distances of ~ 25 Å away from each other—packing effects might be important in the former case, it is not in the latter one. Finally, for $\Xi=100$, $\widetilde{r}_{typ}\simeq 28\mu$ and one finds that the typical lateral distance is ~ 8.4 Å for divalent counterions, and 16.8 Å for trivalent counterions. In other words, for the system with trivalent counterions, the point-like assumption is safe. The fact that for some of the systems μ is smaller than the typical ionic radii is not critical, since the density profiles shown can be thought of as the probability distribution of finding the center of charge at distance $\widetilde{z}$ from the contact distance between the wall and the ion.

From this we can conclude that the problem studied here, and in particular the strong coupling regime, is not only of academic interest, but can be realized in the laboratory, using water as solvent and at room temperature. In fact, multivalent ions play an important role in biological systems, where organic ions like Spermidine (with valence $3+$) or Spermine (with valence $4+$), as well as inorganic ions like Calcium (valence $2+$) are present in the cellular medium (in this case, however, the screening of the ions by other species might change the scenario of the problem). By changing the temperature and/or the medium where the ions are dissolved, as for instance by using organic ions in low dielectric constant solvents (as has been recently used in the context of the critical behavior of ionic solutions[94, 78, 64, 93, 116]), one can fix the Gouy-Chapman length so that it stays at reasonable values even at very high values of Ξ.

We have up to now assumed the system to have smeared out charge distributions in the plane, and that the dielectric constant is the same everywhere. How good are these approximations? This is the question we will address in the next two chapters.

Chapter 3

The influence of the dielectric constant

After studying the simple double layer in detail, we now introduce a dielectric jump at the charged wall and investigate its effect on the counterion density distribution. As we will show, the Poisson-Boltzmann description of the double layer remains a good approximation at low coupling values, while the strong coupling theory is shown to lead to the correct density profiles close to the wall at all values of Ξ; for very large Ξ, only systems where the difference between the dielectric constants of the wall and of the solvent is small are well described by SC (at all values of $\widetilde{z}$).

3.1 Introduction

The first modification to the simple double layer problem that we will investigate the influence of a dielectric jump (that coincides with the charged wall) on the counterion distribution. The situation is the same as shown in Fig. 2.1, but now with $\varepsilon_< \neq \varepsilon_>$.

Dielectric effects can play an important role in different problems in soft condensed matter, as for instance in the influence of image-charges on the adsorption of polyelectrolytes onto oppositely charged surfaces[101], or in the process of ionic binding into specific sites in proteins[90], as in the activation of certain enzymes through the binding of Ca^{2+} ions. In the case of the double layer problem, the motivation to look at this is quite clear: the counterions are generally dissolved in water (with $\varepsilon = 80\varepsilon_0$), while the charged surface—either a Langmuir monolayer sitting at the air–water interface[71], or a charged mica surface in a surface force apparatus[47, 50]—has typically a very different dielectric constant. Another interesting case, which we will not analyze here, is when the ions are in the presence of a metallic electrode (with $\varepsilon = \infty$).

The double layer with the dielectric jump has been studied in the past with the help of different techniques, like computer simulations[15], liquid state theories[54, 9], as well as field theory[96], usually leading to the expected depletion of counterions close to the charged wall (when the medium where the ions are has the highest dielectric constant). In this Chapter, we will apply the Monte Carlo simulation techniques used in the previous Chapter to study image-charge effects, and as in the previous case, we will also test the PB as well the SC predictions.

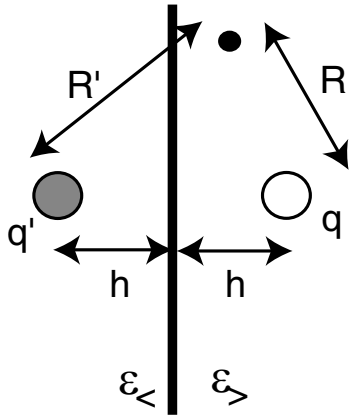

Figure 3.1: Schematic view of a point charge in the presence of a dielectric jump (modeled by the image-charge to left). The black dot corresponds to the test point (see text).

3.2 Interaction between charges in the presence of a dielectric jump

We begin with a quick derivation of the electric potential generated by one charge in the presence of a dielectric jump. We will use here the method of images[102], which is the simplest way to obtain the potential for this case.

Let us assume the configuration shown in Fig. 3.1. The point charge qe (where q is the charge valence) is located at $\mathbf{r} = (0, 0, h)$ and the dielectric jump at the $z = 0$ plane. The latter is modeled by a image-charged $q'e$ at $\mathbf{r} = (0, 0, -h)$ and the boundary condition

$$\varepsilon_< \frac{\partial\varphi(0^-)}{\partial z} = \varepsilon_> \frac{\partial\varphi(0^+)}{\partial z}, \tag{3.1}$$

where $\varepsilon_<$ and $\varepsilon_>$ are the dielectric constants at $z < 0$ and $z > 0$, respectively, and φ is the electric potential. Another boundary condition comes from the continuity of φ at the wall, i.e., $\varphi(0^-) = \varphi(0^+)$. The potential at a test point located at $z > 0$ is then given by

$$\varphi(x, y, z > 0) = \frac{e}{4\,\pi\,\varepsilon_>}\Big[\frac{q}{R} + \frac{q'}{R'}\Big] \tag{3.2}$$

where

$$R = \sqrt{x^2 + y^2 + (z - h)^2} \tag{3.3}$$

is the distance between the *point charge* and the test point and

$$R' = \sqrt{x^2 + y^2 + (z + h)^2} \tag{3.4}$$

is the distance between the *image-charge* and the test point. For $z < 0$ the potential reads

$$\varphi(x, y, z < 0) = \frac{e}{4\,\pi\,\varepsilon_<}\frac{q''}{R}. \tag{3.5}$$

Notice that at a test point in the region $z < 0$, one would not feel the image-charge $q'e$ nor the real charge qe, but a "renormalized" charge $q''e$ at the point $(0, 0, h)$. With this we have two unknowns

(q' and q'') and two boundary conditions. Solving this leads to

$$\varphi(x,y,z) = \begin{cases} e/4\,\pi\,\varepsilon_> \left[q/R + q\,\Delta/R'\right] & \text{if } z > 0 \\ qe/2\,\pi\,R\,[\varepsilon_> + \varepsilon_<] & \text{if } z < 0. \end{cases} \tag{3.6}$$

R and R' are still given by Eqs. (3.3) and (3.4) and

$$\Delta = \frac{\varepsilon_> - \varepsilon_<}{\varepsilon_> + \varepsilon_<}. \tag{3.7}$$

Formally solving the Poisson equation, viz.

$$\nabla\left[\varepsilon(\mathbf{r})\nabla\varphi(\mathbf{r},\mathbf{r}')\right] = -qe\delta(\mathbf{r}-\mathbf{r}') \tag{3.8}$$

(where $\varepsilon(r) \equiv \varepsilon_<\theta(-z) + \varepsilon_>\theta(z)$; $\theta(z)$ is 1 if $z > 0$ and 0 otherwise) with the same boundary conditions leads, as it should, to the same result for the potential.

We now interpret this. A test point at $z < 0$ feels only the source charge at $(0,0,h)$, but with a different value for its charge. On the other hand, when the test point is in the half-space $z > 0$ it not only feels the original source charge at $(0,0,h)$, but also a second charge (the image-charge) at $(0,0,-h)$ with charge $qe\Delta$. If $\varepsilon_> > \varepsilon_<$ then Δ is positive and the image has the same sign as the source charge; if $\varepsilon_> < \varepsilon_<$ then $\Delta < 0$ and source and image-charges have opposite sign. We will use this potential when writing down the Hamiltonian for the double layer in the presence of a dielectric jump.

3.3 The Hamiltonian

With arguments similar to the ones just presented, it is easy to show that a plane with charge density $e\,\sigma_s$ located at the interface where the dielectric jump occurs generates the electric field (for $z > 0$)

$$E = \frac{e\,\sigma_s}{2\varepsilon_>}[1+\Delta], \tag{3.9}$$

which in fact corresponds to the field generated by the charges in the plate (e σ_s) and their images (e $\sigma_s\,\Delta$).

With Eq. (3.9) and the potential Eq. (3.6), we can write down the Hamiltonian of a system composed by a charged wall located at a dielectric jump and its counterions in solution,

$$\begin{aligned} \frac{\mathcal{H}}{k_B\,T} =& \Xi \sum_{j=1}^{N-1}\sum_{k=j+1}^{N}\left\{\frac{1}{|\widetilde{\mathbf{r}}_j - \widetilde{\mathbf{r}}_k|} + \frac{\Delta}{\sqrt{[\widetilde{\mathbf{r}}_j - \widetilde{\mathbf{r}}_k]^2 + 4z_j z_k}}\right\} \\ &+ \sum_{j=1}^{N}\left\{\frac{\Xi\,\Delta}{4\widetilde{z}_j} + [1+\Delta]\widetilde{z}_j\right\}, \end{aligned} \tag{3.10}$$

where all lengths have been rescaled with $\mu = 1/2\pi q\ell_B\sigma_s$ (the Gouy-Chapman length) according to $\mathbf{r} = \widetilde{\mathbf{r}}\,\mu$. As before, Ξ is the coupling parameter as defined in Eq. (2.4) and Δ is given by Eq. (3.7). the Bjerrum length now uses $\varepsilon_>$ in its definition, Eq. (2.2). The first term on the rhs of

Eq. (3.10) refers to the interaction between the counterions in solution while the second one refers to the interactions between each counterion and the images of the other counterions; the third term is the interaction between a counterions and its *own* image, and the last term corresponds to the interaction between the counterions and the charged wall. We will only study systems with $\Delta > 0$; for systems with with negative Δ, one would have to introduce a finite separation between the solution with the counterions and the dielectric jump to avoid the collapse of the particles onto their (oppositely charged) images—in other words, we would have to introduce a hard core for the counterions.

Before we discuss the results obtained with the Monte Carlo simulations, we use the Hamiltonian Eq. (3.10) and do a very simple scaling analysis. As in the case treated in the previous chapter, we can naively assume that the counterions will either be (i) in a three-dimensional disordered structure, with the typical distance between ions scaling like $r_t \sim \Xi^{1/3}$ or (ii) in a planar-like structure, with $r_t \sim \Xi^{1/2}$; as before, the latter structure is the preferred one at high coupling, while the former at low coupling. Unlike the simple double layer, the particles are not going to be necessarily at a typical distance of one μ away from the wall, as the simulations will demonstrate. As a first guess, one can say that what will dictate the interaction between one particle and the wall is the balance between the attraction due to the smeared out charge on the plane (as well as their images) and the repulsion due to the particle's own image (which has a charge with the same sign). The energy per particle is approximately given by

$$\frac{E_{pl}}{N k_B T} \sim [1+\Delta]\widetilde{z} + \frac{\Xi\,\Delta}{4\widetilde{z}}. \tag{3.11}$$

For fixed Δ and Ξ, this energy per particle has a minimum at

$$\widetilde{z}^* = \sqrt{\frac{\Xi\,\Delta}{4\,[1+\Delta]}} \tag{3.12}$$

with the value

$$\frac{E_{pl}^{min}}{k_B T} = \sqrt{\Xi\Delta[1+\Delta]} \tag{3.13}$$

at the minimum. This means that one should expect a maximum in the density profile to occur approximately at $\widetilde{z} = \widetilde{z}^*$, irrespective of the coupling.

At vanishing coupling the mean-field solution, as before, should be recovered. In fact, $\widetilde{z}^*$ vanishes with $\Xi^{1/2}$, and the (expected) maximum of the density moves towards the wall. The derivation done in the previous Chapter for the PB solution assumed the same dielectric constant everywhere; it is a simple matter to show that this is not a necessary condition for PB, and that the dielectric jump does not change the mean-field result. In other words, with vanishing coupling the simulations should show density profiles that are very close to the ones predicted by PB.

In Appendix B we derive the expression predicted by the strong coupling theory[80] for the density profile (at lowest order), which reads

$$\frac{\rho(\widetilde{\mathbf{r}})}{2\pi\ell_B\sigma_s^2} = \sqrt{\frac{1+\Delta}{\Xi\Delta}}\,\frac{1}{K_1\big(\sqrt{\Xi\Delta[1+\Delta]}\big)}\,\exp\!\left(-[1+\Delta]\widetilde{z} - \frac{\Xi\Delta}{4\widetilde{z}}\right), \tag{3.14}$$

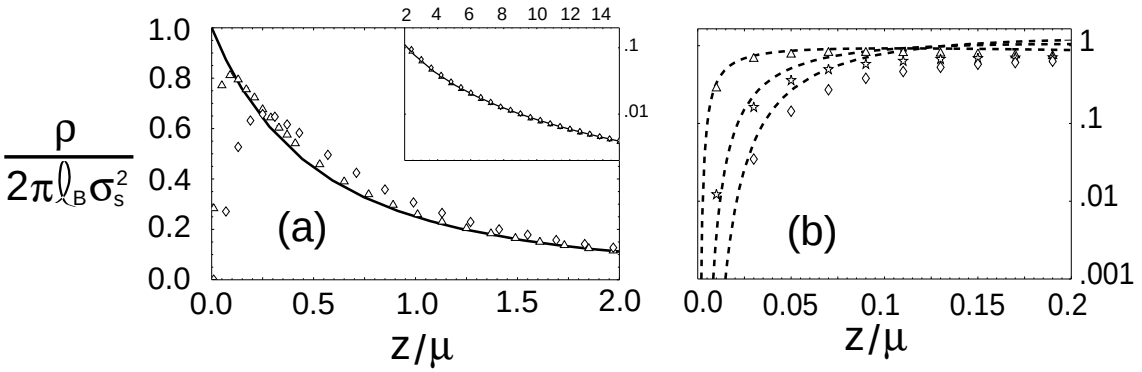

Figure 3.2: Rescaled density profiles from Monte Carlo simulations (75 particles and 10^6 MCS) for $\Xi = 0.5$ and $\Delta = 0.1$ (open triangles) and $\Delta = 0.95$ (open diamonds). In Plot (a), the full line corresponds to the PB solutions, Eq. (2.16). In Plot (b), we also show $\Delta = 0.5$ (open stars) and compare the simulations with the SC predictions (dashed lines), Eq. (3.14). The error bars are comparable to or smaller than the symbols.

where $K_1(x)$ is the first order modified Bessel function of second kind[2]. The strong coupling theory (at this order a one-particle theory) predicts a density profile that is determined only by the interactions between counterions and the wall and counterions and their images. These results can now be testes with the Monte Carlo simulations.

3.4 Monte Carlo simulations: results

The technical details of the simulations presented here are essentially the same as for the simple double layer, Section 2.4. We use the Hamiltonian Eq. (3.10) to calculate the electrostatic energy of the configurations tested in the course of the simulations (as before, we use the Lekner summation[63]).

In Fig. 3.2a we show the simulation results[72] for a system with $\Xi = 0.5$ (75 particles and 10^6 MC steps) for $\Delta = 0.1$ and 0.95, the latter corresponding approximately to the Δ for an interface between water ($\varepsilon \simeq 80\varepsilon_0$) and hydrocarbon ($\varepsilon \simeq 2\varepsilon_0$). As expected, the maximum of the density occurs close to $\widetilde{z}^*$ (0.11 and 0.25 for each case, respectively); as $\widetilde{z}$ grows, the density profiles quickly converge to the PB prediction, with practically no distinction between them for $\widetilde{z} \gtrsim 3$ (inset to Fig 3.2a). At small distances from the wall, the densities fall quickly to zero: a comparison with the strong coupling theory is done in Fig 3.2b for $\Delta = 0.1$, 0.5 and 0.95, where we see that the small distance behavior of the density is approximately dominated by the counterion–wall and counterion–image interactions (as in Eq. (3.14)).

Fig. 3.3 is the same as Fig. 3.2, but now for $\Xi = 10$. The full line in Fig. 3.3 corresponds to the simulation results obtained in the previous Chapter ($\Delta = 0$) for the same coupling. It is clear that as $\widetilde{z}$ grows, the density profile of the systems with $\Delta \neq 0$ also converge to the profile of the $\Delta = 0$ system, but at a slower rate than exhibited by the systems with $\Xi = 0.5$. The small distance behavior is again approximately given by the SC theory (dashed lines), even though SC is a bad description for $\widetilde{z} > 0.5$.

Finally, we show in Fig. 3.4 the results for systems well within the strong coupling regime, viz. $\Xi = 10^3$ (Fig. 3.4a, $\Delta = 0.1$, 0.5 and 0.95) and $\Xi = 5 \times 10^4$ (Fig. 3.4b, $\Delta = 0.1$ and

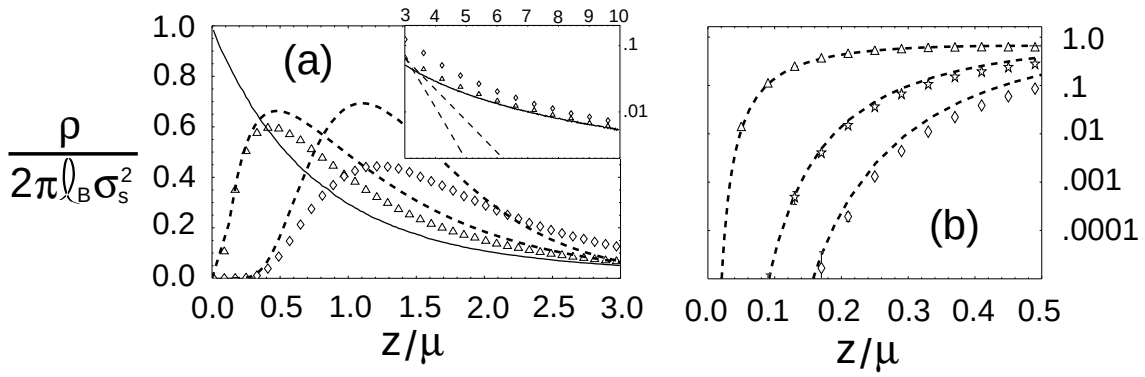

Figure 3.3: Rescaled density profiles from Monte Carlo simulations (75 particles and 10^6 MCS) for $\Xi = 10$ and $\Delta = 0.1$ (open triangles) and $\Delta = 0.95$ (open diamonds). In Plot (a), the full line corresponds to the simulation results obtained in the previous Chapter ($\Delta = 0$) for $\Xi = 10$. In Plot (b) we also show the results for $\Delta = 0.5$ (open stars). In all plots the dashed lines are the SC predictions, Eq. (3.14).The error bars are comparable to or smaller than the symbols.

0.2). It becomes clear that the SC predition, Eq. (3.14), yields only the correct density profiles at small values of Δ. In fact, the density profiles always have the maximum at $\widetilde{z}$ larger than the ones predicted by SC. This is not surprising, and can be understood if we remind that the SC theory (at this order) is a one-particle theory; when the highly coupled counterions form the planar structure at distance $\sim \widetilde{z}^*$ from the wall, SC neglects the repulsive contribution between each particle and the image of all other particles, which are also organized in a planar structure at $\sim -\widetilde{z}^*$. Besides, the fluctuations of the density around the maximum are quite strong (as the density profiles in Fig 3.4 demonstrate), and so the multibody correlation effects cannot be so easily overlooked.

3.5 Conclusions

The simulation results can be summarized in the following conclusions: (i) for couplings in the limit $\Xi \to 0$, the region $\widetilde{z} \ll \widetilde{z}^*$ (which vanishes with the square root of the coupling, cf. Eq.(3.12)) is dominated by the counterion–image-charge interaction and SC becomes asymptotically correct; however, the density profile for large $\widetilde{z}$ quickly converges to the profile predicted by the PB theory. For moderate couplings ($\Xi = 10$), (ii) the same as (i) is concluded, except that the convergence of the density profiles to the $\Delta = 0$ profile slows down with increasing coupling and increasing value of Δ. Finally, (iii) the very high coupling regime is only correctly described by the SC theory for small values of Δ; this confirms the conclusion of the previous Chapter, viz. SC is asymptotically correct as $\Xi \to \infty$ in the case $\Delta = 0$, but also calls the attention to the fact that a one-particle theory (as the SC) neglects effects that become important when the dielectric jump is large, in particular the influence of the images of the other counterions on each counterion. While this seems to be unimportant for small Δ, it cannot be neglected as Δ approaches 1.

An interesting, although trivial, aspect of the results shown here is the fact that the ionic cloud is confined to the region $\widetilde{z} > 0$ not by the hard wall, but by the repulsion between the counterions and their images: for any non-vanishing coupling and Δ, the entropy gain is not enough to drive the counterions away from the solution, since the energetic price to cross the wall is infinite.

In all results, as expected, the larger the difference between the dielectric constants at the

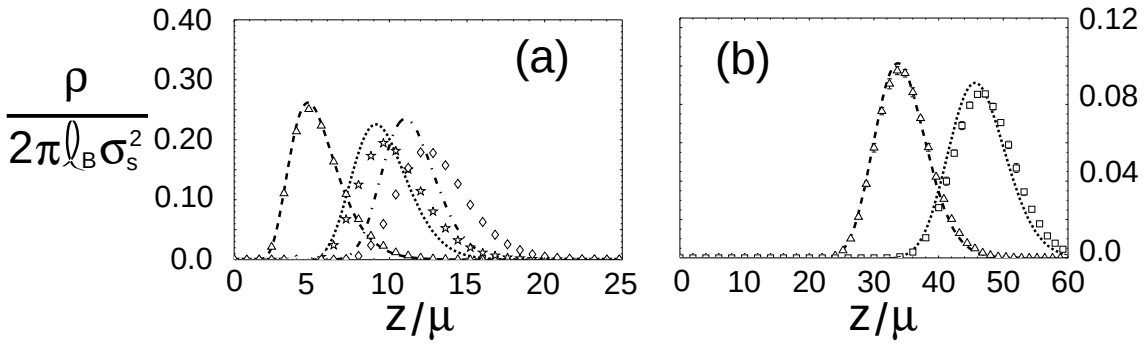

Figure 3.4: Rescaled density profiles from Monte Carlo simulations (75 particles and 10^6 MCS) for (a) $\Xi = 10^3$ and $\Delta = 0.1$ (open triangles), $\Delta = 0.5$ (open stars) and $\Delta = 0.95$ (open diamonds), and for (b) $\Xi = 5 \times 10^4$ and $\Delta = 0.1$ (open triangles), $\Delta = 0.2$ (open squares). The dashed lines correspond to the SC preditions, Eq. (3.14). The error bars are comparable to or smaller than the symbols.

interface, the larger is the effect on the density profile. In fact, for larger values of Δ the repulsion between the counterion cloud and the wall is larger; a similar effect is responsible for a larger repulsion between two charged walls (with dielectric jumps) as the difference between the dieletric constants of the walls and of the solvent with the counterions grows[15].

After investigating the effect of the dielectric constant, we now turn to the effects due to the discretized nature of the charges at the wall.

Chapter 4

Discrete charges at the wall

In this Chapter we focus our attention on the effects due to the discreteness of the charges that form the charged plane. The counterions are still assumed to be point-like, but we constraint the distance of approach between ions in the plane and counterions to a minimum distance D. The ratio between D and the distance between neighboring ions in the plane is, as we will see, one of the important quantities in determining the influence of the discrete nature of the charges at the wall over the density profiles. Another parameter that plays an important role, as in the previous case, is the coupling Ξ: as we will demonstrate, systems with higher coupling are more subject to discretization effects than systems with low coupling parameter.

4.1 Introduction

In most experimental setups that entail charged surfaces, the charge on the surface is not smeared out but formed by chemical groups that are somehow confined to the surface, such that when the latter is in contact with a solvent, counterions are released and it becomes charged. For example, monolayers of ionic surfactants at an air–water interface[10] (where the water-loving head groups release counterions) form a charged layer at the interface. Another example comes from colloidal particles, as for instance latex spheres[86], which often have carboxyl groups (COOH) chemically attached to their surface. When the colloidal particles are in solution, these groups loose hydrogens and become negatively charged (and so the surface of the particle).

Nevertheless, under some conditions the continuum hypothesis for the charge on a surface is a reasonable assumption; in fact, the success of the Poisson-Boltzmann theory somehow proves this. Contrary to what happened in the previous Chapters, the solution of the PB equation when the charges on the wall are discrete demands considerable numerical work; the same happens to the density profile that follows from the strong coupling theory. In such situations, the Monte Carlo method becomes the best tool: although numerically demanding (due to the sums needed to calculate the energy), one is not confined to look at the low (PB) or high (SC) coupling regimes, but has also access to intermediate regimes.

In this Chapter we consider the point charges fixed at the wall to be in a two-dimensional square lattice that is at $z/\mu = \widetilde{z} = -\widetilde{D}$. Although this is done for simplicity, such two-dimensional lattices can be for instance obtained with compressed monolayers[71]. A hard wall is located at

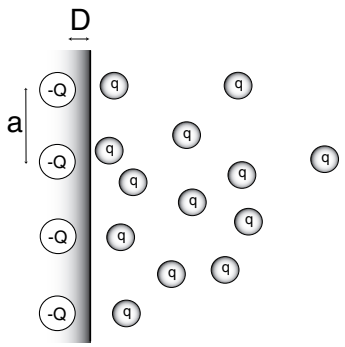

Figure 4.1: Schematic view of system studied in this Chapter, with discrete charges on the wall.

$\widetilde{z} = 0$, and point-like counterions are free to move in the half-space $\widetilde{z} > 0$ (cf. Fig. 4.1). The minimum distance between the fixed charges and the counterions is then $\widetilde{D} = D/\mu$, which prevents the collapse of the counterions into the fixed ions. This distance should roughly correspond to the radius of the charged groups at the wall plus the radius of the counterions. By assuming point-like counterions we neglect hard-core effects that will be important for dense systems, where the packing of the ions—especially close to the wall where the counterion density can be large—influences the final results by setting a maximum allowed value for the density (dense packing).

One way to estimate the behavior of the counterion distribution is by looking at the electric field generated by the two-dimensional array of fixed charges. One expects the existence of a minimum distance away from the lattice (in the perpendicular direction) above which the discrete nature of the charges on the wall becomes irrelevant. In other words, as one moves away from the lattice, the charge distribution looks increasingly as if it were smeared out. This is the topic of the next Section, which proves to be quite useful to interpret the simulation results.

4.2 The electric field due to a 2D square lattice

The electric field generated by the fixed charge density $\sigma(\mathbf{r})$ is given by[102]

$$\widetilde{\mathbf{E}} \equiv \frac{e^2\mathbf{E}(\mathbf{r})}{k_BT} = \int \mathrm{d}\mathbf{r}'\sigma(\mathbf{r}')\frac{\ell_B}{\left[\mathbf{r}-\mathbf{r}'\right]^2}\frac{\mathbf{r}-\mathbf{r}'}{|\mathbf{r}-\mathbf{r}'|}, \tag{4.1}$$

For the hard wall located at $z = 0$ and the square lattice at $z = -D$, the fixed charge density reads

$$\sigma(\mathbf{r}) = -Q\delta(z+D)\sum_{k=-\infty}^{+\infty}\delta(x-ka)\sum_{l=-\infty}^{+\infty}\delta(y-la) \tag{4.2}$$

where Q is the charge valence of each ion in the array and a is the lattice constant, assumed to be the same for the x and y directions. The origin of the xy plane is located at one arbitrarily chosen ion in the lattice. If we put this charge density in Eq. (4.1), then the absolute value of the z-component of the electric field reads

$$|\widetilde{E}_z| = \ell_B\sigma_s\frac{(z+D)}{a}\sum_{k=-\infty}^{+\infty}\sum_{l=-\infty}^{+\infty}\frac{1}{\left[[\xi-k]^2+[\eta-l]^2+[z+D]^2/a^2\right]^{3/2}} \tag{4.3}$$

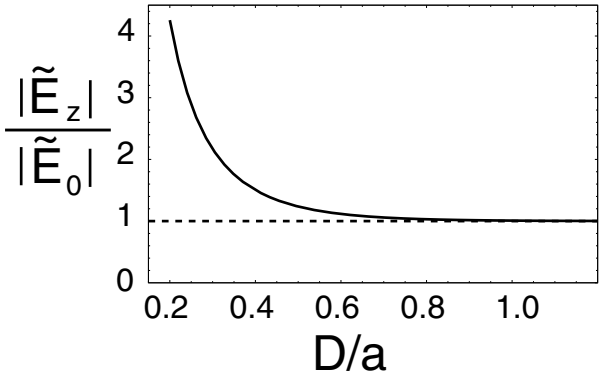

Figure 4.2: The value of the z-component of the electric field due to a 2D square lattice at $z = -D$ at the point $\xi = \eta = z = 0$ (i.e., at the hard wall and directly above one of the charges in the the lattice), as a function of D/a, where a is the lattice spacing. Notice that for $D/a \simeq 0.6$ the field is only 12% larger than the one expected for a smeared out distribution (dashed line). The discrete nature of the charges at the wall is important only for small values of D/a.

where we used the fact that the charge density of the lattice σ_s equals Q/a^2; we also used the definitions $\xi = x/a$ and $\eta = y/a$.

Based on Lekner[63], we transform this sum into a fast converging series by applying (i) the Euler transformation, Eq. (A.2), (ii) the Poisson-Jacobi identity, Eq. (A.3), and finally (iii) the integral representation of the modified Bessel function of second kind, Eq. (A.5). After some algebraic manipulation, Eq. (4.3) reads

$$\widetilde{E}_z = 2\pi\ell_B\sigma_s\Bigg\{\frac{\sinh(2\pi[z+D]/a)}{\cosh(2\pi[z+D]/a)-\cos(2\pi\eta)} + 4\frac{z+d}{a}\sum_{k=1}^{\infty}\cos(2\pi k\xi) \times \sum_{l=-\infty}^{+\infty}\frac{k}{\sqrt{l^2+[z+D]^2/a^2}}K_1\big(2\pi k\sqrt{l^2+[z+D]^2/a^2}\Bigg\}, \quad (4.4)$$

where K_1 is the first order modified Bessel function of second kind[2]. For very large argument, $K_1(x) \sim \exp(-x)/\sqrt{x}$, i.e., for increasing $[z+D]/a$ the sum involving the Bessel function above becomes less important, and the field in the z-direction approaches the limiting value $|\widetilde{E}_0| = 2\pi\sigma_s\ell_B$, or $|E_0| = \sigma_s/2\epsilon$, which is the field due to an homogeneously charged wall with charge density σ_s. In fact, the numerical solution of Eq. (4.4) shows that this limiting solution is attained quite fast as D/a grows. In Fig. 4.2 we show $|\widetilde{E}_z|/|\widetilde{E}_0|$ for $\xi = \eta = z = 0$, i.e., the test point is at the hard wall but directly above one of the charges at the lattice. For $D/a = 0.6$, the field due to the lattice is only $\sim 12\%$ above the one expected for the smeared out distribution; for $D/a = 1$, it is 0.8% above (see also Ref. [47] for a similar calculation). In other words, within the model studied in this Chapter, the discrete nature of the charges is only important when the distance between the lattice and the hard wall is below approximately half of the distance between neighboring fixed ions.

Note that the conclusions based on the electric field are basically valid for a system at zero temperature. As the temperature grows, the coupling between the ions at the wall and the counterions goes down, and one expects the discretization to become even less important, i.e., the minimal value of D/a below which the discrete nature of the charges at the wall is important should be

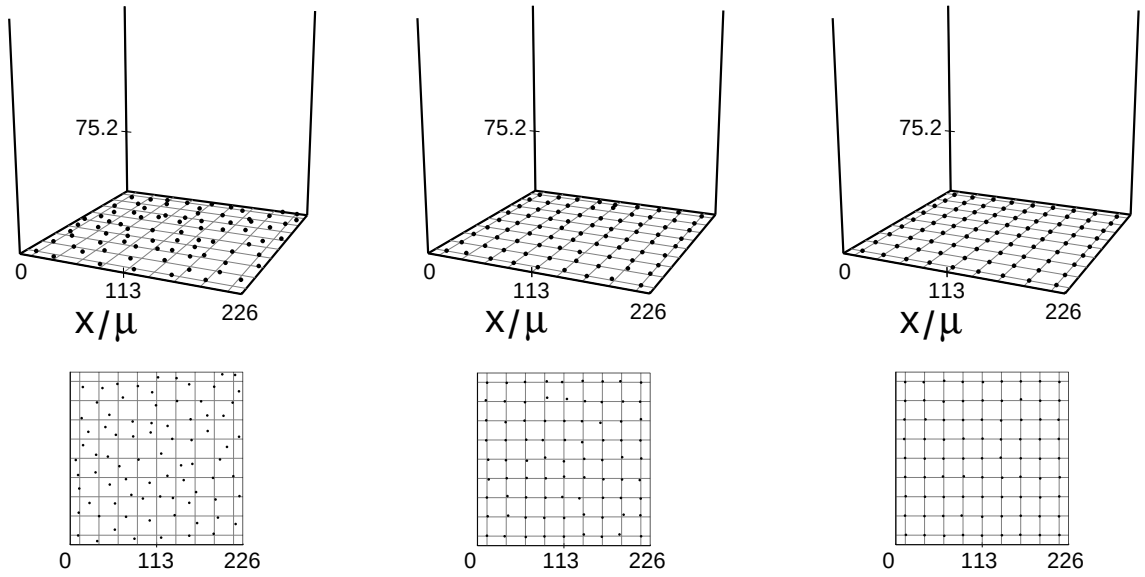

Figure 4.3: Side and top view snapshots for $\Xi = 100$ (with 81 counterions). From left to right, $\widetilde{D} = 10$ ($\widetilde{D}/\widetilde{a} = 0.4$), $\widetilde{D} = 5$ ($\widetilde{D}/\widetilde{a} = 0.2$) and $\widetilde{D} = 3$ ($\widetilde{D}/\widetilde{a} = 0.12$). Notice that as $\widetilde{D}/\widetilde{a}$ decreases, the counterions tend to localize, and stay at the vicinity of the ions fixed at the wall (located below the nodes of the grey lines on the plane).

smaller for systems with low coupling (high temperature) than for systems with high coupling (low temperature). The simulations will confirm this.

4.3 Simulation results

The Hamiltonian of the system reads

$$\frac{\mathcal{H}}{k_B T} = \sum_{j=1}^{N-1} \sum_{k=j+1}^{N} \frac{q^2\,\ell_B}{|\mathbf{r}_j - \mathbf{r}_k|} - \sum_{j=1}^{N} \sum_{k=1}^{N_p} \frac{qQ\,\ell_B}{|\mathbf{r}_j - \mathbf{r}_k|} \tag{4.5}$$

where Q is the charge valence of the particles at the plane and N_p is such that $qN = QN_p$ (electroneutrality). The technical details for the simulations done for this system are the same as what has been described in Section 2.4. We again use the Lekner summation[63] to calculate the electrostatic energy of the system periodically repeated in the x and y directions, now with the charges at the wall being also treated as point charges. For practical reasons we used in the simulations $Q = q$, simplifying the construction of the lattice of fixed charges in the plane $z/\mu = \widetilde{z} = -\widetilde{D}$ (for instance, a system with $N = 100$ with $Q = q$ has a lattice with 10×10 charges). In this case the box size is given by $L/\mu = \widetilde{L} = \sqrt{2\pi N \Xi}$ and the lattice constant by $a/\mu = \widetilde{a} = \sqrt{2\pi\Xi}$, after rescaling all lengths with the Gouy-Chapman length μ.

As it became clear in the previous Section, one of the important variables in this system is the ratio between D, the distance between the lattice and the hard wall (contact distance), and a, the lattice constant. According to Fig. 4.2, one does not have to simulate systems where this ratio is of the order 1 or larger, because the answers will be the same as obtained in Chapter 2

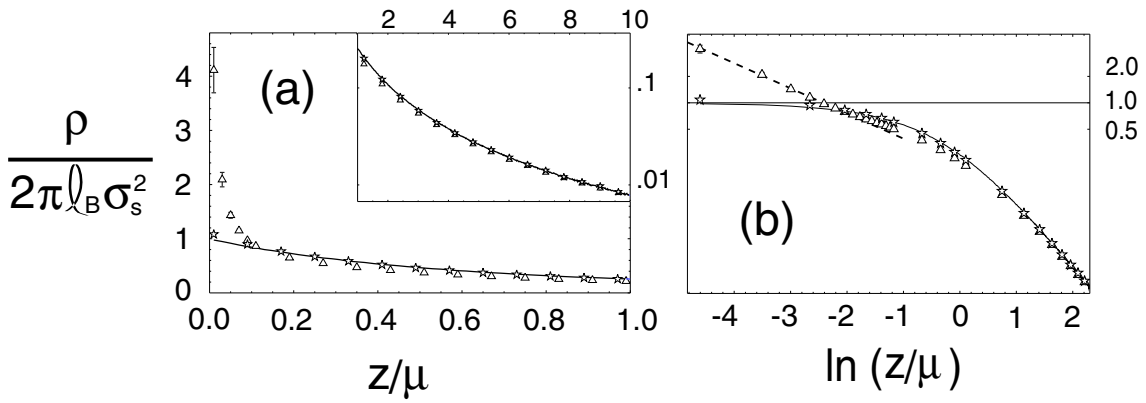

Figure 4.4: Simulation results for counterion density distribution (integrated in x and y) for $\Xi = 1$ (81 particles and 10^6 MC steps) and $D/\mu = \widetilde{D} = 0.1$ ($\widetilde{D}/\widetilde{a} = 0.040$, open triangles) and $\widetilde{D} = 0.3$ ($\widetilde{D}/\widetilde{a} = 0.12$, open stars). The full line corresponds to the MC results obtained for the same coupling, but with smeared out charges on the plane. Plot (a): profile between $\widetilde{z} = 0$ and 1 and (inset) between 1 and 10. Plot (b): log-log plot of the profile between 0 and 1. The dashed line is the fitted curve $-1.6 - 0.66\,\ln(\widetilde{z})$, i.e., the density profile for $\widetilde{D}/\widetilde{a} = 0.040$ initially decays like $\widetilde{z}^{-2/3}$.The error bars are comparable to or smaller than the symbols.

(irrespective of the coupling). When the discretization effects are important, the density profile is not homogeneous in the directions parallel to the wall: the counterions tend to localize and prefer to stay in the vicinity of the ions ate the wall, as depicted in Fig. 4.3 for a system with $\Xi = 100$. However, we will focus our attention on the integrated counterion density profiles (i.e., integrated in the directions x and y), which can be compared to the results obtained in Chapter 2.

Fig. 4.4a shows the results[72] for a system with $\Xi = 1$ (81 particles and 10^6 MC steps) and the lattice at two values of $\widetilde{D} = D/\mu$, viz. $\widetilde{D} = 0.1$ ($\widetilde{D}/\widetilde{a} = 0.040$) and $\widetilde{D} = 0.3$ ($\widetilde{D}/\widetilde{a} = 0.12$). For comparison, we also plot the Monte Carlo results for the same system with the smeared out charges, as obtained in Chapter 2 (full line). For $\widetilde{D}/\widetilde{a} = 0.040$ the deviation between the density profiles is clear: due to the discretization, the charge density close to the wall is, as expected, a few times larger than 1 (the value at contact for the rescaled density with smeared out charges). On the other hand, the discretization is almost unimportant for $\widetilde{D}/\widetilde{a} = 0.12$, a value well below what one would expect from the considerations in the previous Section. In the inset to Fig. 4.4a we see that all density profiles collapse into one curve (which, as we saw in Chapter 2, is very close to the PB prediction) quite quickly, with very small differences between the profiles for $\widetilde{z} > 3$. In Fig. 4.4b we plot the log-log plot of the density profile for $\widetilde{z}$. Interesting is the fact that the density profile of the system with $\widetilde{D}/\widetilde{a} = 0.040$ decays initially with a $-2/3$ power law (cf. linear fit in the log-log plot) crossing over, as $\widetilde{z}$ grows, to the familiar PB behavior (which eventually becomes a -2 power law).

Fig. 4.5a shows the results for the system with $\Xi = 10$ (100 particles and 10^6 MC steps) for $\widetilde{D} = 1$ ($\widetilde{D}/\widetilde{a} = 0.13$) and $\widetilde{D} = 2$ ($\widetilde{D}/\widetilde{a} = 0.25$). For $\widetilde{D}/\widetilde{a} = 0.13$ the discretization effect is large (contrary to what happens for the system with $\Xi = 1$), while for $\widetilde{D}/\widetilde{a} = 0.25$, the density profiles obtained with and without discrete charges are almost the same. In the inset to Fig. 4.5a we see that the density profile with $\widetilde{D}/\widetilde{a} = 0.13$ slowly converges into the profile for the smeared out system (considerably slower than the case with $\Xi = 1$ and $\widetilde{D}/\widetilde{a} = 0.040$). Finally, in Fig. 4.5b we again show the log-log plot of the density versus distance: now the initial decay of the curve

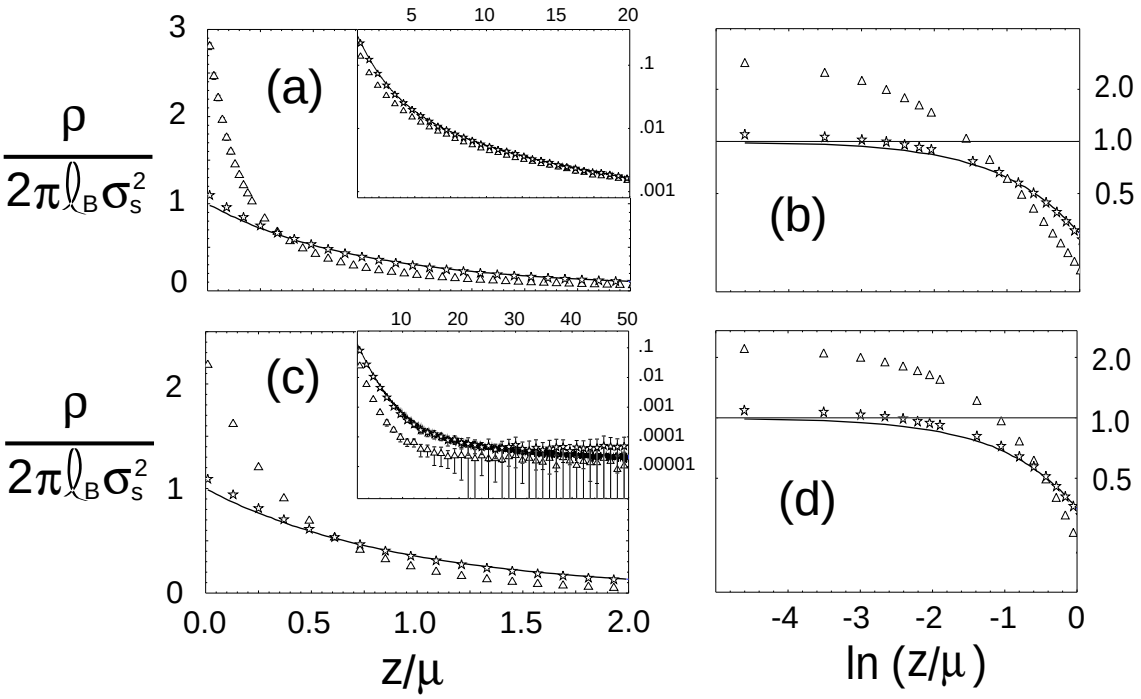

Figure 4.5: Simulation results for counterion density distribution (integrated in x and y) for $\Xi = 10$ (above) and $\Xi = 100$ (below). For $\Xi = 10$ (100 particles and 10^6 MC steps), the results shown correspond to $\widetilde{D} = 1$ ($\widetilde{D}/\widetilde{a} = 0.13$, open triangles) and $\widetilde{D} = 2$ ($\widetilde{D}/\widetilde{a} = 0.25$, open stars). For $\Xi = 100$ (also 100 particles and 10^6 MC steps), the results are for $\widetilde{D} = 6$ ($\widetilde{D}/\widetilde{a} = 0.24$, open triangles) and $\widetilde{D} = 10$ ($\widetilde{D}/\widetilde{a} = 0.40$, open stars). The full lines correspond to the MC results obtained for the same couplings, but with smeared out charges on the plane. Plots (b) and (d) are the respective log-log plots of the density profiles close to the wall. Unless when explicitly shown, the error bars are comparable to or smaller than the symbols.

with $\widetilde{D}/\widetilde{a} = 0.13$ is approximately the same as the decay of the other curves, that is, it is not a power-law decay. It is important to note that the contact value of the density profiles for $\Xi = 1$ and $\widetilde{D}/\widetilde{a} = 0.040$ and for $\Xi = 10$ and $\widetilde{D}/\widetilde{a} = 0.13$ are approximately the same, i.e., the effect due to discretization is, in relative terms, the same in the two cases. Nevertheless, the density profiles that come out are fundamentally different. Similar conclusions follow from the results for $\Xi = 100$ (100 particles and 10^6 MC steps), which are depicted in Figs. 4.5c and 4.5d for $\widetilde{D} = 6$ ($\widetilde{D}/\widetilde{a} = 0.24$) and $\widetilde{D} = 10$ ($\widetilde{D}/\widetilde{a} = 0.4$). In the inset we see that the convergence of the curve with $\widetilde{D}/\widetilde{a} = 0.24$ to the other curves is quite slow (at the large $\widetilde{z}$ it is difficult to obtain good statistics, since the densities are very low, and the error bars are large).

With the previous analysis, it becomes also clear that depending on the value of Ξ, the discretization will be more or less important for the same ratio $\widetilde{D}/\widetilde{a}$: for instance, at $\widetilde{D}/\widetilde{a} = 0.12$–$0.13$, the system with $\Xi = 1$ is weakly affected by the discretization, while for $\Xi = 10$ the effect is quite clear. The same follows for $\widetilde{D}/\widetilde{a} = 0.24$–$0.25$ for the systems with $\Xi = 10$ (discretization is almost unimportant) and $\Xi = 100$ (discretization is important). This behavior is summarized in Fig. 4.6, where $\widetilde{D}/\widetilde{a}$ is fixed at approximatelly 0.12 for the three couplings discussed above, viz. $\Xi = 1$, 10 and 100. As expected, the system with the highest coupling (or lowest temperature) is the one that shows the largest contact value for the density at the wall, i.e., discretization becomes

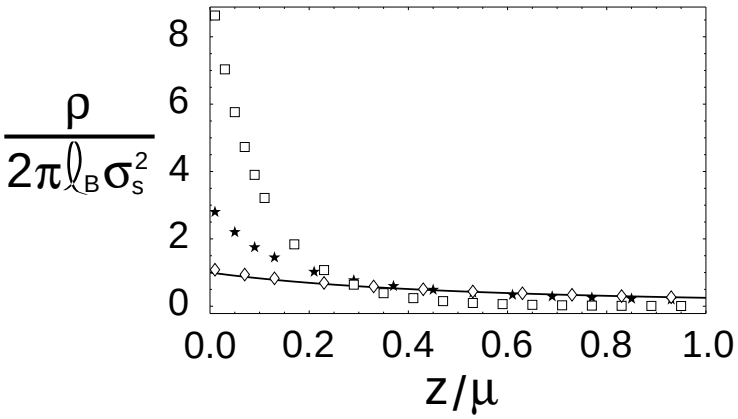

Figure 4.6: Simulation results of the counterion density distributions (integrated in x and y) for $\Xi = 1$ and $\widetilde{D} = 0.3$ ($\widetilde{D}/\widetilde{a} = 0.12$, open diamonds), $\Xi = 10$ and $\widetilde{D} = 1$ ($\widetilde{D}/\widetilde{a} = 0.13$, filled stars) and $\Xi = 100$ and $\widetilde{D} = 3$ ($\widetilde{D}/\widetilde{a} = 0.12$, open squares). The PB density profile is also plotted for reference (full line). The error bars are comparable to or smaller than the symbols.

increasingly important as the coupling parameter grows.

4.4 Conclusions

In summary, we have studied the effects due to the discrete nature of the charges at the wall on the counterion cloud in solution. The simple analysis using the z-component of the electric field generated by a two-dimensional square lattice shows that one should expect the discretization to be important for $\widetilde{D}/\widetilde{a}$ below approximately 0.5. From the simulations, we have conclued that the value of $\widetilde{D}/\widetilde{a}$ below which discretization matters becomes smaller as Ξ decreases, or in other words, for the same value of $\widetilde{D}/\widetilde{a}$ the systems with higher Ξ are more sensitive to the discrete fixed charges. The snapshots shown in Fig 4.3 also show that as $\widetilde{D}/\widetilde{a}$ decreases, the counterions tend to localize and "bind" to the fixed ions in the plane, which explains the increase of the contact value of the density as $\widetilde{D}/\widetilde{a}$ becomes smaller.

A system with monovalent counterions with a contact distance between ions at the wall and counterions of approximately 6 Å (which is a reasonable value, cf. Chapter 6) and coupling equal to 1 would have $\widetilde{D}/\widetilde{a} \sim 0.33$ (cf. Table 2.1); with coupling $\Xi = 10$, this ratio would be $\widetilde{D}/\widetilde{a} \sim 1$. In both cases the model used in this Chapter would predict that the discrete nature of the charges at the wall would not be important. While this might help in understanding why the Poisson-Boltzmann theory works so well, the experimental systems are much more complicated than the model used here assumes: for instance, if instead of putting a hard wall at $\widetilde{z} = 0$ one would put each of the charges at the wall inside a hard half-sphere that would avoid the collapse of the counterions on the fixed ions, the counterions would be able to sit between ions at the wall, and the effects of the discretization would in principle be stronger.

In the next Chapter we will look at the interaction between double layers, i.e., we will confine the counterions between two similarly charged walls and see how this influences the interaction between the walls. This leads to interesting and relevant questions on, for instance, the stability of lyophobic colloids[114] (which stay in solution due to the repulsive interaction between the

macroions) or on the interaction between highly charged DNA molecules[99, 38, 41].

Chapter 5

Counterions confined between two equally charged walls

After studying the isolated double layer, we look at the interaction between two double layers. The system is composed by two equally charged walls at distance d with their counterions confined between them. The charge at the walls is smeared out and the dielectric constant is the same everywhere. Using Monte-Carlo simulations we obtain the inter-plate pressure in the global parameter space, and the pressure is shown to be negative (attraction) at certain conditions. The simulations also show that the equilibrium plate separation (where the pressure changes from attractive to repulsive) exhibits a novel unbinding transition. We compare the Monte Carlo results with the strong-coupling theory, which is shown to describe well the bound states at moderate and high couplings. The regime where the two walls are very close to each other is also shown to be well described by the SC theory.

5.1 Introduction

Up to now we have focused our attention on systems with one charged wall where the counterions were free to move in an infinite half-space. We have seen how the isolated double layer behaves at low and high coupling, and how the dielectric constant and the discrete character of the charges at the wall can affect the results obtained for the simplest case. At this point, it is a natural step to study counterions that are confined between two similarly charged walls, and see how two double layers interact with each other. This is relevant, for instance, on the problem of stability of colloidal suspensions[114] (for instance, for an small ion the surface of a colloidal particle is almost like an infinite plane), stability of lamellar systems[117] and on DNA condensation[99].

It has been known for a long time that two similarly charged plates can attract each other when in the presence of multivalent counterions. This has been first measured in Monte Carlo simulations[40, 15], and later observed experimentally with the surface force apparatus[50]. The Poisson-Boltzmann theory (which is a part of the DLVO theory[47]) predicts on the other hand that the electrostatic interaction between the surfaces should always be repulsive. In this sense, the attraction with electrostatic origin came as a surprise, especially if one minds that the DLVO theory was very successful in the past in explaining many phenomena related to colloidal stability,

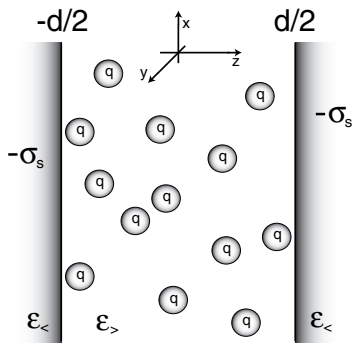

Figure 5.1: Two similarly charged walls at distance d, with their counterions confined between them. Here only systems with $\varepsilon_> = \varepsilon_<$ are considered.

as for instance, the Schulze-Hardy rule[30] (which says that the critical coagulation concentration varies with the counterion valence like $1/q^6$).

This contradiction attracted special attention to this problem. Most theoretical approaches tried to include the correlations (not present in PB) between the counterions and which was thought to be the reason for the discrepancy between the mean-field and the experimental/simulation results[52, 8]. The first theoretical approach that also showed attraction with electrostatic origin is due to Kjellander and Marčelja[54], which used sophisticated integral-equation theory (with HNC closure) and obtained results that compared very well with simulations[40, 54, 53]. Also perturbative expansions around the PB solution[9, 95] and density-functional theory[109, 28] were used, and predicted as well the existence of an attractive interaction. For plates far away from each other, i.e., at distances such that the two double layers weakly overlap, the attractive force was obtained by including in-plane Gaussian fluctuations[91] and, more recently, plasmon fluctuations[60].

In this Chapter, we study the system of confined counterions through extensive Monte Carlo simulations, and compare it with the analytical predictions for both the weak and the strong coupling regime.

5.2 Attraction: a simple scaling argument

Let us assume that the walls are so close to each other that their distance is smaller than the typical lateral distance r_{typ} between two neighboring counterions. In such conditions, a counterion has lateral correlation with the surrounding counterions—it will stay preferably away from them—but will be free to move (between the walls) in the perpendicular direction. The probability of finding a counterion at a certain distance from each of the walls is constant, i.e., the counterions between the two walls act like a constant charge distribution in the perpendicular direction. The electrostatics in the system can be modeled by two similarly charged walls with charge density σ_s that have an oppositely charged plane between them with charge density $2\sigma_s$ (due to electroneutrality).

We now look at the forces acting on one of the walls, say, the one at $d/2$ (Fig. 5.1). There are two contributions to the total force. One comes from the balance between the attraction due to the (oppositely charged) plane in the middle and the repulsion due the other (similarly charged) wall.

This contribution reads

$$\frac{F_{el}}{k_BT} = -A\,\sigma_s\left\{\frac{2\sigma_s}{2\varepsilon k_BT} - \frac{\sigma_s}{2\varepsilon k_BT}\right\} = -A\,2\pi\ell_B\sigma_s^2 \tag{5.1}$$

where A is the area of the wall; note that this contribution is attractive. From the ideal gas equation of state $PV = Nk_BT$ comes the second contribution to the force: the ideal entropic force (due to the counterions) acting on the area A is

$$\frac{F_{id}}{k_BT} = A\,\frac{N}{V} = 2A\frac{\sigma_s}{qd}, \tag{5.2}$$

which is repulsive. In the latter we used the electroneutrality condition $\sigma_s = qNd/2V$, where V is the volume that confines the N counterions and d is the distance between the walls. Summing the two contributions, the total pressure acting on the wall is

$$\frac{P}{2\pi\ell_B\sigma_s^2} = -1 + \frac{2}{\widetilde{d}} \tag{5.3}$$

where the pressure P is in units of k_BT and $\widetilde{d} = d/\mu$ is the rescaled distance between the walls ($\mu \equiv 1/2\pi q\ell_B\sigma_s$ is the Gouy-Chapman length). What this scaling argument says is that at $\widetilde{d} = 2$, the pressure felt by the walls is zero, i.e., the equilibrium distance between the walls is finite.

As previously mentioned, one should mind that this argumentation only holds when the typical lateral distance between counterions, defined though $\pi r_{typ}^2 = q/2\sigma_s$, is much larger than 2μ, which is the obtained equilibrium distance between the walls. This is equivalent to say that the coupling constant (defined and used in the previous Chapters) $\Xi \equiv 2\pi q^3\ell_B^2\sigma_s$ has to be larger than four. As we will demonstrate below, the picture used for this scaling argument is asymptotically exact in the limit of strong coupling and/or small distances between the walls.

5.3 Poisson-Boltzmann and strong coupling

One can apply to this problem similar analytical techniques as used for the double layer problem. The saddle-point equation—valid for small coupling parameter—is again the Poisson-Boltzmann equation, which after rescaling all lengths by the Gouy-Chapman length reads

$$\frac{\mathrm{d}^2\tilde{\phi}(\tilde{z})}{\mathrm{d}\tilde{z}^2} = 2\imath\Lambda\mathrm{e}^{-\imath\tilde{\phi}(\tilde{z})}, \tag{5.4}$$

with $\widetilde{z} \in [-\widetilde{d}/2, \widetilde{d}/2]$ and the boundary conditions $\mathrm{d}\widetilde{\phi}(0)/\mathrm{d}\widetilde{z} = 0$ and $\widetilde{\phi}(0) = 0$. As before, Λ is the rescaled fugacity which is determined by the normalization (or electroneutrality) condition

$$\Lambda\int_{-\widetilde{z}/2}^{\widetilde{z}/2}\mathrm{d}\widetilde{z}\left\langle\mathrm{e}^{-\imath\phi(\widetilde{z}}\right\rangle = 2. \tag{5.5}$$

The solution of Eq. (5.4) is

$$\imath\widetilde{\phi} = 2\ln\cos\left(\Lambda^{1/2}\,\widetilde{z}\right), \tag{5.6}$$

with Λ given by the solution of the transcendental equation

$$\frac{1}{\Lambda^{1/2}} = \tan\left(\frac{\widetilde{d}}{2}\Lambda^{1/2}\right) \tag{5.7}$$

which follows from the normalization condition, Eq. (5.5). Using Eq. (2.12), the PB density profile of the counterions between the wall finally reads

$$\frac{\rho(\tilde{\mathbf{r}})}{2\pi\ell_B\sigma_s^2} = \frac{\Lambda}{\cos^2\left(\Lambda^{1/2}\widetilde{z}\right)}. \tag{5.8}$$

We can use the contact value theorem derived in Appendix C to calculate the pressure acting on the walls when they are at distance $\widetilde{d}$ apart. A positive pressure means that the walls want to go away from each other (repulsion), while a negative pressure means that the walls want to approach each other (attraction). The theorem states that the pressure at one of the walls (say, the one at $\widetilde{d}/2$) is related to the density of counterions at contact through

$$\frac{P}{2\pi\ell_B\sigma_s^2} = -1 + \frac{\rho(\widetilde{d}/2)}{2\pi\ell_B\sigma_s^2}, \tag{5.9}$$

where P is the pressure in units of k_BT. From Eqs. (5.8) and (5.7), $\rho(\widetilde{d}/2)/2\pi\ell_B\sigma_s^2 = 1+\Lambda$, and consequently Poisson-Boltzmann predicts that

$$\frac{P}{2\pi\ell_B\sigma_s^2} = \Lambda. \tag{5.10}$$

We remind that Λ is always a positive quantity. This a classical result[87, 7, 47], stating that the plates will always repel each other at the mean-field level. At distances $\widetilde{d} \ll 1$, Eq. (5.7) yields the solution $\Lambda \simeq 2/\widetilde{d}$, and the pressure reads

$$\frac{P}{2\pi\ell_B\sigma_s^2} = \frac{2}{\widetilde{d}}, \tag{5.11}$$

which is the ideal gas contribution to the pressure, Eq. (5.2). This means that, according to PB, when the walls are close enough the counterions behave purely as an ideal gas.

In the other limit, $\widetilde{d} \gg 1$, $\Lambda \simeq \pi^2/\widetilde{d}^2$ and

$$\frac{P}{2\pi\ell_B\sigma_s^2} = \frac{\pi^2}{\widetilde{d}^2}. \tag{5.12}$$

The latter expression has been used to describe the electrostatic (repulsive) contribution to the pressure in thick wetting films, and is related to the Langmuir equation[58, 47, 7]. Note that Eq. (5.12) can be rewritten as $P = 1/8q^2\ell_B d^2$ showing that in this limit the pressure becomes independent of the surface charge density

We now turn our attention to the limit $\Xi \to \infty$, where PB breaks-down. Again, as for the single-wall problem, one can derive the strong coupling (SC) density profile[80]. This is done at lowest order in Appendix B, and the result is

$$\frac{\rho(\widetilde{z})}{2\pi\ell_B\sigma_s^2} = \frac{2}{\widetilde{d}}, \tag{5.13}$$

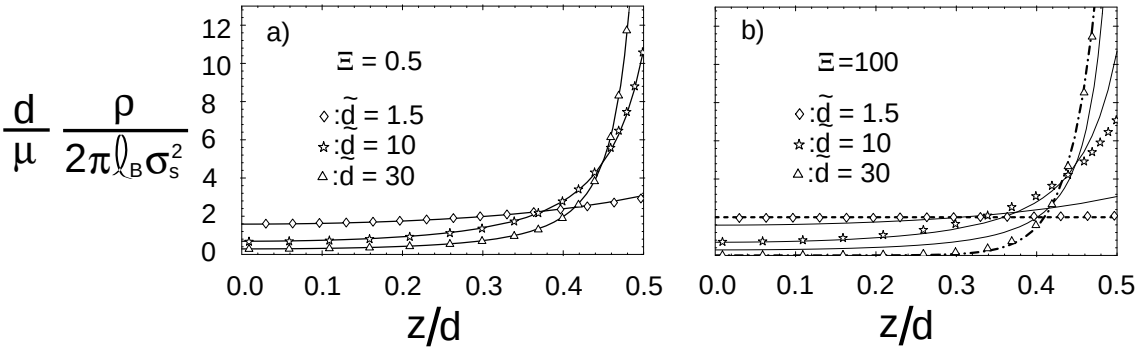

Figure 5.2: MC results for the rescaled counterion density distribution as a function of the rescaled distance from the wall z/d in the a) PB limit for $\Xi = 0.5$ and in the b) SC limit for $\Xi = 100$ for various separations $\tilde{d} = d/\mu = 1.5$ (open diamonds), $\tilde{d} = 10$ (open stars), and $\tilde{d} = 30$ (open triangles). In a) MC results agree well with the corresponding PB predictions (Eq.(5.8), solid lines), whereas in b) results for $\tilde{d} = 1.5$ agree with the asymptotic SC prediction, Eq.(5.13) (dashed line) and for $\tilde{d} = 30$ with two decoupled walls in the SC regime, Eq. (5.15).The error bars are comparable to or smaller than the symbols.

which is a constant density profile. Notice that this is the starting point of the scaling analysis done in the previous Section. The simulations will confirm this results if Ξ is high enough and if the walls are close enough to each other. Using again the contact value theorem,

$$\frac{P}{2\pi\ell_B\sigma_s^2} = -1 + \frac{2}{\widetilde{d}} \tag{5.14}$$

which is the same as Eq. (5.3) obtained with the simple scaling analysis, and as before, leads to negative values of the pressure for $\widetilde{d} > 2$. If $\widetilde{d}$ is very small (viz. $\widetilde{d} \ll 2$), the positive (entropic) contribution dominates over the negative electrostatic contribution (-1 in the rhs of Eq. (5.14)). This is a subtle difference between PB and SC at small $\widetilde{d}$: PB predicts the pressure to be equal to the one of a pure ideal gas, while SC still corrects it with an electrostatic contribution.

As simulations will show, as $\widetilde{d}$ grows the constant profile predicted for large coupling eventually breaks down. For large Ξ and $\widetilde{d} \to \infty$, the MC results show that (cf. Fig. 5.2) the profile is approximately described by

$$\frac{\rho(\widetilde{z})}{2\pi\ell_B\sigma_s^2} = \frac{1}{1-\mathrm{e}^{-\widetilde{d}}}\left\{\exp(-\widetilde{z}-\widetilde{d}/2) + \exp(\widetilde{z}-\widetilde{d}/2)\right\}, \tag{5.15}$$

which incidentally is a sum of two exponential decays, corresponding to the superposition of the solutions of two isolated charged walls (with their counterions) in the SC limit.

Before showing the simulations, we can summarize what we have discussed up to now. On one hand, at low coupling, PB predicts a counterion density profile between the walls that leads to repulsion between the plates at all distances. On the other hand, at high coupling, there are two distinct limits, viz. when the distance between the walls is much smaller than the typical lateral distance between counterions, where a constant density profile between the walls is obtained and negative pressure (attraction) can occur; the second regime, when the walls are far enough from each other and the profile is approximately described by Eq. (5.15). We now use the computer simulations to test these results.

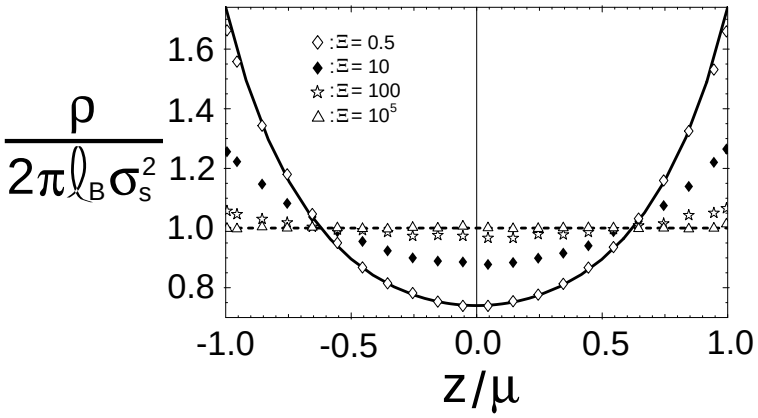

Figure 5.3: MC results for rescaled counterion density profiles $\tilde{\rho} = \rho/2\pi\ell_B\sigma^2$ for fixed plate separation $\tilde{d} = d/\mu = 2$ as a function of the rescaled distance $\tilde{z} = z/\mu$ from one wall. Symbols correspond to coupling parameters $\Xi = 0.5$ (open diamonds), $\Xi = 10$ (filled diamonds), $\Xi = 100$ (open stars), and $\Xi = 10^5$ (open triangles), exhibiting clearly the crossover from the PB prediction (solid line, Eq.(5.8)) to the SC prediction (dashed line, Eq.(5.13)). The error bars are comparable to or smaller than the symbols.

5.4 Monte Carlo results

We performed Monte Carlo simulations on the two-wall system[72], with typically 100–150 counterions and simulated for 10^6 Monte Carlo steps (MCS, defined as a cycle where the computer sequentially tries to move each particle in the system). The systems are assumed to be periodic in the direction parallel to the walls, and the Lekner summation was again used to calculate the interactions between counterions. The technical details are basically the same as in Section 2.4.

5.4.1 Density profiles

Fig. 5.2 shows the MC counterion density profiles obtained for two values of the coupling, viz. $\Xi = 0.5$ and 100, for distances $\widetilde{d} = 1.5$ (open diamonds), 10 (open stars) and 30 (open triangles) between the walls. Fig. 5.2a shows the good agreement between the simulation and the PB results (solid lines) for all values of $\widetilde{d}$. In Fig. 5.2b the same comparison is made, and PB (thin solid lines) clearly fails to describe the profiles. Notice that for $\Xi = 100$, the projected lateral distance between counterions is $\widetilde{r}_{typ} = 20$: for $\widetilde{d} = 1.5$, $\widetilde{d}/\widetilde{r}_{typ} = 0.075$ and, as expected, the constant density profile given by Eq. (5.13) (dashed line) agrees with the simulations (open diamonds); for $\widetilde{d} = 10$, $\widetilde{d}/\widetilde{r}_{typ} = 0.5$ and the system is in an intermidiate state, where the counterions density profile (open stars) is not described by any of the analytical results given above; finally, for $\widetilde{d} = 30$, $\widetilde{d}/\widetilde{r}_{typ} = 1.5$ and the superposition of two single-wall SC solutions, Eq. (5.15) (dash-dotted line), agrees with the simulations (open triangles).

In Fig. 5.3 the crossover between the PB (solid line) and the SC (dashed line) is shown for fixed $\widetilde{d} = 2$ and different couplings, viz. $\Xi = 0.5$ (open diamonds), $\Xi = 10$ (filled diamonds), $\Xi = 100$ (open stars) and $\Xi = 10^5$ (open triangles).

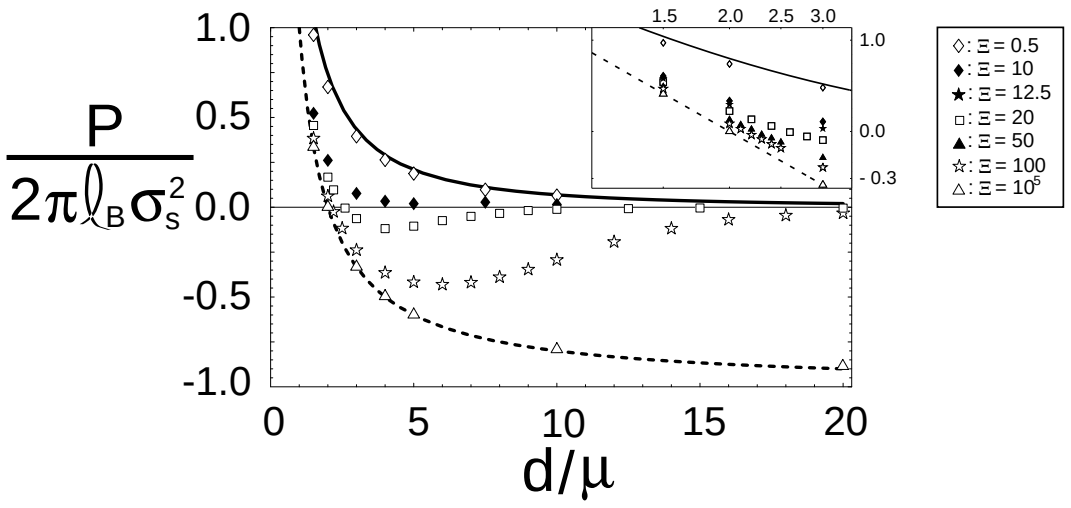

Figure 5.4: MC results for the rescaled pressure $P/2\pi\ell_B\sigma^2$ as a function of the rescaled plate separation $\tilde{d} = d/\mu$ for the same parameter values as in Fig. 5.3 (and $\Xi = 20$, open squares), compared with the PB prediction Eq. (5.10) (solid line) and the SC prediction Eq. (5.14) (dashed line). Inset: Log-log plot of the rescaled pressure as a function of $\tilde{d} = d/\mu < 3$ for $\Xi = 10^5$, 100, 50, 20, 12.5, 10 and 0.5 (from bottom to top). Notice that for small separations between the plates, the strong coupling description is generally better than Poisson-Boltzmann. The error bars are comparable to or smaller than the symbols.

5.4.2 Pressure

From the counterion density profiles obtained with the simulations we can calculate the pressure felt by the walls. If enough data on the density profile close to the walls is available, one can extrapolate the curve and obtain the contact value (value of the density at a wall), from which the pressure follows through the contact value theorem, Eq. (5.9). In our simulations, we had typically bins (for obtaining the density profile, cf. Section 2.4.3) of size 0.02μ, which allowed the extrapolation of the data to contact.

In Fig. 5.4 we show the pressure for systems with different values of Ξ as a function of the separation $\widetilde{d}$ between the walls. As already seen in the previous figures, the system with $\Xi = 0.5$ (open diamonds) agrees well with the PB prediction (solid line) given by Eq. (5.10), while the system with high coupling, $\Xi = 10^5$, agrees well with the SC (dashed line) prediction Eq. (5.14) at this range; notice that for $\Xi = 10^5$, $\widetilde{r}_{typ} \sim 600$, meaning that for this system a distance of $\widetilde{d} = 20$ is still well within the limit where the constant density profile (SC) is valid.

The other systems shown ($\Xi = 10$, 20 and 100) lie between the two analytical results, but as the inset in Fig. 5.4 demonstrates, as $\widetilde{d}$ decreases the pressure values for these systems are increasingly closer to the prediction given by SC (with the constant density profile). The system with $\Xi = 10$ shows always positive pressure (within the error bars, see also Fig. 5.7), while at higher couplings positive and negative values of the pressure (attraction) occur, and a finite equilibrium distance $\widetilde{d}^*$ between the plates arises, viz. where P crosses, with negative derivative, the d-axis. This attractive behavior between equally charged plates has first been seen in a computer simulation by Guldbrand et al. for a system with divalent counterions in water at room temperature and $\sigma_s = 1/71.4$ Å^{-2} (i.e., with $\Xi \simeq 36$).

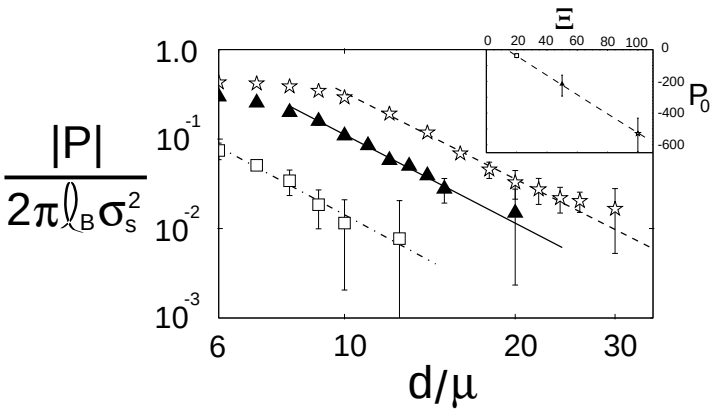

Figure 5.5: Log-log plot of the the absolute value of the rescaled pressure $P/2\pi\ell_B\sigma^2$ obtained from simulations as a function of $\tilde{d} = d/\mu > 5$ for $\Xi = 20$ (open squares), $\Xi = 50$ (filled triangles) and $\Xi = 100$ (open stars). The lines are fits to the data: for $\Xi = 20$, the slope is ~ -3.4, for $\Xi = 50$, ~ -3.3 and for $\Xi = 100$, ~ -3.2. Inset: dependence of P_0 (see text) obtained from the fits to the data in the main graph, as a function of the coupling. Unless when explicitly shown, the error bars are comparable to or smaller than the symbols.

The long range behavior of the pressure for $\Xi = 20$, 50 and 100 is shown in more detail in Fig. 5.5. The lines are fits to the data points: for $\Xi = 20$, the line is given by $3.62(\pm 0.30) - 3.42(\pm 0.15)\ln(\widetilde{d})$, for $\Xi = 50$, $5.38(\pm 0.30) - 3.29(\pm 0.10)\ln(\widetilde{d})$ and finally for $\Xi = 100$, $6.27(\pm 0.20) - 3.21(\pm 0.10)\ln(\widetilde{d})$. If we assume that this attractive contribution to the pressure is approximately of the form P_0/d^3, it follows that P_0 depends on the coupling through $P_0 \simeq 87.3 - 6.14\Xi$ (inset in Fig. 5.5); P_0 vanishes at $\Xi \simeq 14$, which approximatelly coincides with the coupling below which no binding between the walls occurs (cf. phase diagram, Fig. 5.6). In other words, the attractive tail of the force between the plates decays approximately like $\widetilde{d}^{-3}$, in agreement with previous results[9, 91, 66]. The prefactor P_0 given here approximately agrees with the same prefactor from Ref. [9] for the aymptotic pressure, but is approximately one order of magnitude larger than the one from the Ref. [91].

5.4.3 The equilibrium distance between the walls

From the pressure data, it becomes clear that for large values of the coupling there is a finite value of $\widetilde{d}$ where the pressure is zero (the equilibrium distance between the walls), while for low values of Ξ the pressure is never negative (i.e., the equilibrium distance between the walls is infinite). This is summarized in Fig. 5.6, where the equilibrium distance for the two-wall system is plotted as a function of the coupling and of the distance between between the walls. Each point corresponding to the equilibrium distance was determined by simulating systems in the vicinity of $\widetilde{d}^*$ (where the pressure is zero and its derivative is negative). The full line is only a guide to the eye, and corresponds to the equilibrium curve: a system above it tends to shrink, one below it to expand. As the coupling tends to infinity the equilibrium distance saturates around $\widetilde{d}^* = 2$, which is the asymptotic value predicted by SC. There is a minimum value of Ξ (around 11) below which no attraction occurs between the plates. As $\widetilde{d}$ approaches this value from above, the equilibrium distance between the walls diverges, exhibiting a novel unbinding transition. Numerically, we were unable to determine whether this unbinding transition is continuous or discontinous.

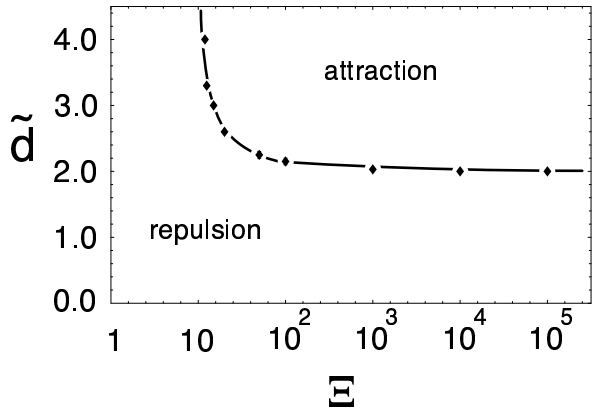

Figure 5.6: Regions of positive (repulsive) and negative (attractive) pressure as a function of the rescaled plate separation $\tilde{d} = d/\mu$ and coupling strength Ξ (valid for small and intermidiate values of $\widetilde{d}$). The dividing line denotes the equilibrium plate separation $\tilde{d}^*$, which saturates at $\tilde{d}^* = 2$ for $\Xi \to \infty$ and which grows as Ξ approaches the value $\Xi^* \approx 11$ from above.

As the distance between the walls grows, the pressure between the plates is expected to vanish from positive values[40]; one indication for this is the fact that the attractive tail of the pressure (as previously shown in Fig. 5.5) decays approximately like $\widetilde{d}^{-3}$, which is faster than the repulsive mean-field (PB) decay $\widetilde{d}^{-2}$: the latter dominate the former, and the pressure eventually becomes again positive[9]. This means that one should expect to see a local maximum in the pressure at large $\widetilde{d}$, which indeed has been seen by Guldbrand et al.[40] for $\Xi = 14.6$, $\Xi = 12.9$ and $\Xi = 11.3$, with a height of approximatelly 20 mM (corresponding in our rescaled pressures to a height of ~ 0.012), and located at approximatelly $\widetilde{d} \sim 10$. This should be compared with our results in Fig. 5.7 for $\Xi = 15$, 12.5 and 10: in the three cases shown, the errorbars have a size comparable to the expected height of the local maximum. In other words, from our data we are unable to confirm or exclude this effect. Differences in the way the pressure is determined[49] might explain the difference in the accuracy between our work and Ref. [40].

Although of interest, this latter question is not relevant to the bound state of most systems, since the line where the plate separation equals the typical lateral distance between counterions crosses the line shown in Fig. 5.6 at $\widetilde{d} \sim 3$. This means that for systems with moderate to large coupling, the bound state is well described by the SC prediction.

5.5 Conclusions

At low enough values of Ξ, the PB solution describes the system quite well. On the other hand, at high coupling the SC prediction (constant density profile) is confirmed by the simulations in the regime where the walls are close enough to each other. Two similarly charged walls can attract each other (although only electrostatic interactions are involved) if the coupling is high enough; at low values of Ξ the attraction disappears, in agreement with previous results[40, 54]: the connection between these two distinct behaviors at high and low coupling is done by the unbinding transition that occurs at approximately $\Xi \sim 11$.

Finally, most of the bound states in the phase diagram Fig. 5.6 have equilibrium distances such

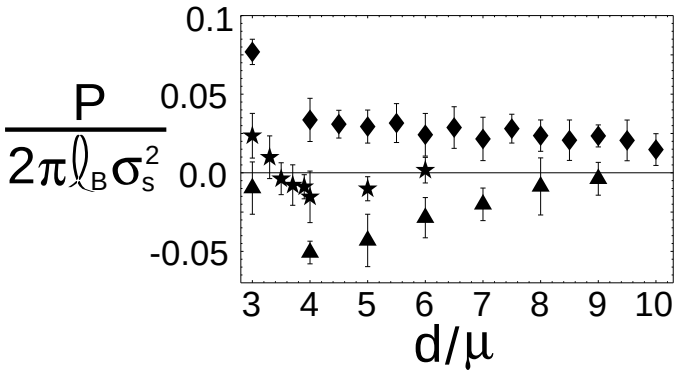

Figure 5.7: Pressure versus distance for $\Xi = 10$ (filled diamonds), 12.5 (filled stars)and $\Xi = 15$ (filled triangles). Notice that the two latter cases show a minimum of the pressure that is already negative. In all cases, the decay of the pressure to zero at large $\widetilde{d}$ is monotonic (after the minimum for $\Xi = 12.5$ and 15).

that they are well described by the SC theory. This means that the correlation between counterions (except in the lateral directions, keeping the ions away from each other) are mostly unimportant for the bound state.

These results are mostly relevant for planar charged systems, like lamellar membrane systems. Notice that a system at room temperature with $\sigma_s = 1/71.4$ Å^{-2} and divalent counterions (in water) has $\Xi = 36$: the bound state is below the dashed curve in Fig. 5.6, and already approximately described by SC (although in such conditions the counterions are at ~ 10 Å away from each other, and packing effects due to their finite size might have some importance). Colloidal particles are not infinite planes, but the results presented here can also say something about the stability of such systems (although the attraction mechanism between spheres has extra contributions due to their finite size[5]). It is known that many systems, like DNA etc., exhibit condensation as multivalent counterions are introduced in solution. In the case of the two walls, this is easily understood by noticing that the coupling parameter changes by a factor of 8 when going from mono- to divalent counterions, and a factor of 27 when going to trivalent counterions. As we saw, systems with large coupling do have a finite distance of equilibrium between the plates (i.e., show condensation).

Chapter 6

Virial expansion for charged colloids and electrolytes

Using a field-theoretic approach, we derive the exact low-density ("virial") expansion of a binary mixture of positively and negatively charged hard spheres (two-component hard-core plasma, TCPHC). The free energy obtained is valid for systems where the diameters d_+ and d_- and the charge valences q_+ and q_- of positive and negative ions are unconstrained, i.e., the same expression can be used to treat dilute salt solutions (where typically $d_+ \sim d_-$ and $q_+ \sim q_-$) as well as colloidal suspensions (where the difference in size and valence between macroions and counterions can be very large). We also discuss some applications of our results.

6.1 Introduction

The two-component hard-core plasma (TCPHC) has been used for a long time as an idealized model for electrolyte solutions. In this model (also called "primitive model"), the ions are spherical particles that interact with each other via hard-core and Coulomb potentials. The positive ions have a charge $q_+ e$ (where e is the elementary charge) and ionic diameter d_+, while the negative ions have a charge $-q_- e$ and diameter d_-. The particles are immersed in a structureless solvent whose presence is felt only through the value of the dielectric constant of the medium, and the system is (globally) electrically neutral (cf. Fig 6.1).

The TCPHC is a quite simplified version of reality. For instance, it treats the solvent—usually water—as a structureless medium where the charged particles are embedded, neglecting the molecular arrangement that occurs around the ions (which is in the origin of the so-called solvation forces[47]). Also, it assumes the ions to be spheres with the same dielectric constant as the one of the solvent, which might be a reasonable approximation only for some ionic systems.

Nevertheless, even with such simplifications, the TCPHC is still not fully understood. A better understanding of this model is a necessary step if one wishes to develop more realistic approaches to charged systems. In this Chapter, we turn our attention to the low-density, or virial, expansion of the TCPHC. Since it yields exact results for the thermodynamic variables at vanishing concentrations, it can be used to describe dilute systems (like colloidal suspensions) as well as to test approximate results obtained for the TCPHC. We are particularly interested in the effects of

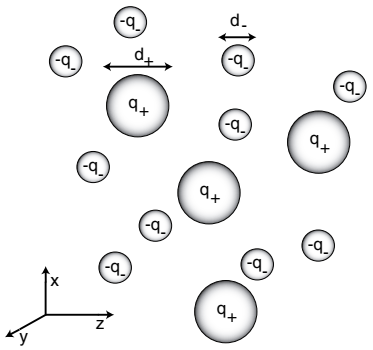

Figure 6.1: Schematic view of the asymmetric two-component hard core plasma (TCPHC).

asymmetry in size and valence on the behavior of the TCPHC.

Due to the long-range character of the Coulomb potential, it is not easy to obtain the thermodynamic behavior of the TCPHC through the usual methods of statistical mechanics. For example, it can be shown[68, 34, 69] that the straightforward application of the cluster expansion to the TCPHC leads to divergent virial coefficients. Mayer[68] proposed a solution to this problem through an infinite resummation of the cluster diagrams, carried out such that the divergent contributions to the virial expansion are canceled. With this, he was able to obtain explicitly the first term in the virial (or low-density) expansion that goes beyond the ideal gas, which turns out to be the well-known Debye-Hückel limiting law[27]. Haga[42] carried the expansion further and went up to order $5/2$ in the ionic density. More or less at the same time, Edwards[29] also obtained the virial expansion of the TCPHC by mixing cluster expansion and field theory.

The methods aforementioned always depend on drawing, counting and recollecting the cluster diagrams which give finite contributions to the expansion up to the desired order in the density. This can be quite a formidable task, and unfortunately it is easy to "forget" diagrams that are relevant to the series (see for instance comment at pp. 222–223 of Ref. [34]). Also, the generalization to ions with different sizes can be quite complicated[34]. Besides, the final results are not given in a closed form, i.e., the final expressions depend on infinite sums that usually have to be evaluated numerically, which is a consequence of the infinite diagrammatic resummation.

We generalize here a novel field-theoretic technique[82], first introduced for the symmetric TCPHC ($q_+ = q_-$ and $d_+ = d_-$), in order to obtain the low-density expansion of the *asymmetric* TCPHC. This method does not use the cluster expansion (and resummation) and yields analytic, closed-form results. We obtain the exact low-density expansion up to order $5/2$ in the volume fraction of a system where the sizes and the charge valences of positive and negative ions are unconstrained, that is, the expression we obtain can be applied, without modifications, to both electrolyte solutions (where ions and counterions have approximately the same size and valence) and to colloidal suspensions (where the macro- and counterions have sizes and valences that can be different by orders of magnitude).

We will take the limit where one of the charged species becomes much smaller and much less charged than the other one, which corresponds to the colloidal limit. As our main result, we show that the electrostatic contribution to the free energy of the TCPHC in this limit maps, up to the second order in the density, into a hard-core one-component plasma with background excluded

from the particles. We will also look at the mean activity coefficient of electrolytes, which is related to the exponential of the chemical potential of the charged species and can be measured experimentally, from which one can get the effective radii of ions when in solution. One of the interesting aspect of this method is that it allows one to obtain the radii as independent parameters, in contrast with what happens, for instance, when the radii are measured from crystal lattices[100].

This Chapter is organized as follows: in Section 6.2 we describe in detail the steps that lead to the low-density expansion Eq. (6.36). In Section 6.3 we apply the free energy obtained to colloidal suspensions and to electrolyte solutions. Finally, Section 6.4 contains some concluding remarks.

6.2 The method

We begin our calculation by assuming a system with N_+ positively charged particles with charge valence q_+ and diameter d_+, and N_- negatively charged particles with charge valence q_- and diameter d_-. The global electroneutrality of the system will be imposed in a later stage of the calculation. As usual, the canonical partition function $\mathcal{Z}$ is

$$\mathcal{Z} = \frac{1}{N_+!N_-!}\int \prod_{i=1}^{N_+} \mathrm{d}\mathbf{r}_i^{(+)} \prod_{j=1}^{N_-} \mathrm{d}\mathbf{r}_i^{(-)}\, \exp\Big(-\frac{\mathcal{H}}{k_B T}\Big) \tag{6.1}$$

where $\mathbf{r}_i^{(+)}$ is the position of the ith positively charged particle (the analogous notation is used for negative particles) and the Hamiltonian $\mathcal{H}$ is given by

$$-\frac{\mathcal{H}}{k_B\,T} = E_{\text{self}} - \frac{1}{2}\sum_{\alpha,\beta}\int \mathrm{d}\mathbf{r}\mathrm{d}\mathbf{r}'\,\hat{\rho}_\alpha(\mathbf{r})\omega_{\alpha\beta}(\mathbf{r}-\mathbf{r}')\hat{\rho}_\beta(\mathbf{r}') - \frac{1}{2}\int \mathrm{d}\mathbf{r}\mathrm{d}\mathbf{r}'\,[\hat{\rho}_+(\mathbf{r}) - \hat{\rho}_-(\mathbf{r})]v_c(\mathbf{r}-\mathbf{r}')[\hat{\rho}_+(\mathbf{r}') - \hat{\rho}_-(\mathbf{r}')]. \tag{6.2}$$

The charge-density operator of the ions are defined as

$$\hat{\rho}_+(\mathbf{r}) = q_+\sum_{i=1}^{N_+}\delta(\mathbf{r}-\mathbf{r}_i^{(+)}), \qquad \hat{\rho}_-(\mathbf{r}) = q_-\sum_{i=1}^{N_-}\delta(\mathbf{r}-\mathbf{r}_i^{(+)}), \tag{6.3}$$

where $\delta(\mathbf{r}-\mathbf{r}')$ is the Dirac delta function. The indices α and β in Eq. (6.2) stand for $+$ and $-$. In order to make some expressions more compact, we will sometimes use this notation: for example, αq_α means both $+q_+$ and $-q_-$. The sum over α and β in Eq. (6.2) runs over all possible permutations (viz. $++$, $--$ and $+-$), i.e., we consider a different short-range potential ω for each combination (in a later stage, the ω's will be assumed to be hard-core potentials). The Coulomb potential is given by $v_c(\mathbf{r}) = \ell_B/r$, where $\ell_B \equiv e^2/(4\,\pi\,\varepsilon\,k_B\,T)$ is the Bjerrum length, defined as the distance at which the electrostatic energy between two elementary charges equals the thermal energy $k_B\,T$. Finally, E_{self} is the self-energy of the system and reads

$$E_{\text{self}} = \frac{N_+}{2}[\omega_{++}(0) + q_+^2 v_c(0)] + \frac{N_-}{2}[\omega_{--}(0) + q_-^2 v_c(0)]. \tag{6.4}$$

Although the self-energies $\omega_{\alpha\beta}(0)$ and $v_c(0)$ are divergent, they do not pose any problems since they will be later exactly canceled.

We proceed by applying the Hubbard-Stratonovich transformation, which can be summarized with the following identity

$$\exp\left(-\frac{1}{2}\int \mathrm{d}\mathbf{r}\mathrm{d}\mathbf{r}'\,\hat{\rho}(\mathbf{r})v(\mathbf{r}-\mathbf{r}')\hat{\rho}(\mathbf{r}')\right) = \frac{\int \mathcal{D}\phi\,\exp\left(-\frac{1}{2}\int \mathrm{d}\mathbf{r}\mathrm{d}\mathbf{r}'\,\phi(\mathbf{r})v^{-1}(\mathbf{r}-\mathbf{r}')\phi(\mathbf{r}') - \imath\int \mathrm{d}\mathbf{r}\,\phi(\mathbf{r})\hat{\rho}(\mathbf{r})\right)}{\int \mathcal{D}\phi\,\exp\left(-\frac{1}{2}\int \mathrm{d}\mathbf{r}\mathrm{d}\mathbf{r}'\,\phi(\mathbf{r})v^{-1}(\mathbf{r}-\mathbf{r}')\phi(\mathbf{r}')\right)} \tag{6.5}$$

where $v(\mathbf{r})$ is some general potential and $\mathcal{D}\phi$ means that the integrals in the rhs are in fact path integrals over the fluctuating field ϕ. While this transformation can be used without problems when $v(\mathbf{r})$ is the Coulomb potential, for the short-range potential this can be more troublesome: for instance, a hard-core potential does not even have a defined inverse function! We will anyway take this formal step for the short-range potential, and, as we will see later, the way we handle the resulting expressions lead to finite (and consistent) results, viz., the virial coefficients.[1]

Applying then Eq. (6.5) to Eq. (6.1) we obtain the partition function in a field-theoretic form

$$\mathcal{Z} = \int \frac{\mathcal{D}\psi_+\,\mathcal{D}\psi_-}{\mathcal{Z}_\psi}\frac{\mathcal{D}\phi}{\mathcal{Z}_\phi}\,\mathrm{e}^{\bar{\mathcal{H}}_0}\,W_+\,W_- \tag{6.6}$$

with the action

$$\bar{\mathcal{H}}_0 = -\frac{1}{2}\sum_{\alpha\beta}\int \mathrm{d}\mathbf{r}\mathrm{d}\mathbf{r}'\,\psi_\alpha(\mathbf{r})\omega^{-1}_{\alpha\beta}(\mathbf{r}-\mathbf{r}')\psi_\beta(\mathbf{r}') - \frac{1}{2}\int \mathrm{d}\mathbf{r}\mathrm{d}\mathbf{r}'\,\phi(\mathbf{r})v_c^{-1}(\mathbf{r}-\mathbf{r}')\phi(\mathbf{r}'), \tag{6.7}$$

where again the indices α and β stand for $+$ and $-$. The inverse potentials are formally defined as the solution of the equation

$$\sum_\beta \int \mathrm{d}\mathbf{r}'\,\omega_{\alpha\beta}(\mathbf{r}-\mathbf{r}')\omega^{-1}_{\beta\gamma}(\mathbf{r}'-\mathbf{r}'') = \delta_{\alpha\gamma}\,\delta(\mathbf{r}-\mathbf{r}'') \tag{6.8}$$

($\delta_{\alpha\gamma}$ is the Kronecker delta) and

$$\int \mathrm{d}\mathbf{r}'\,v_c(\mathbf{r}-\mathbf{r}')v_c^{-1}(\mathbf{r}'-\mathbf{r}'') = \delta(\mathbf{r}-\mathbf{r}''). \tag{6.9}$$

For the Coulomb potential, $v_c^{-1}(\mathbf{r}) = -\nabla^2\delta(r)/4\pi\ell_B$. We have also defined

$$W_\alpha = \frac{1}{N_\alpha!}\left[\mathrm{e}^{\left[\omega_{\alpha\alpha}(0)+q_\alpha^2 v_c(0)\right]/2}\int \mathrm{d}\mathbf{r}\,\mathrm{e}^{-\imath q_\alpha\left[\psi_\alpha(\mathbf{r})+\alpha\,\phi(\mathbf{r})\right]}\right]^{N_\alpha} \tag{6.10}$$

[1] This can be checked in our calculations by turning-off the charges (or simply be setting $\ell_B = 0$) in the final result. Alternatively, one can check this by doing the same calculation as we do here, but having only the hard-core gas from beginning. As expected, this also leads to the correct virial expansion.

(α stands for both $+$ and $-$) and finally,

$$\mathcal{Z}_\psi = \int \mathcal{D}\psi_+ \, \mathcal{D}\psi_- \, \mathrm{e}^{-\frac{1}{2}\sum\limits_{\alpha\beta}\int \mathrm{d}\mathbf{r}\mathrm{d}\mathbf{r}' \, \psi_\alpha(\mathbf{r})\omega^{-1}_{\alpha\beta}(\mathbf{r}-\mathbf{r}')\psi_\beta(\mathbf{r}')} \tag{6.11}$$

and

$$\mathcal{Z}_\phi = \int \mathcal{D}\phi \, \mathrm{e}^{-\frac{1}{2}\int \mathrm{d}\mathbf{r}\mathrm{d}\mathbf{r}' \, \phi(\mathbf{r})v_c^{-1}(\mathbf{r}-\mathbf{r}')\phi(\mathbf{r}')}. \tag{6.12}$$

In order to make the calculations simpler we go to the grand-canonical ensemble. We can do this through the transformation

$$\mathcal{Q} = \sum_{N_+N_-} \lambda_+^{N_+}\lambda_-^{N_-}\mathcal{Z}, \tag{6.13}$$

where λ_+ and λ_- are, respectively, the fugacities (exponential of the chemical potential) of the positively and negatively charged particles. We perform the sum over N_+ and N_- without constraints, i.e., without imposing the electroneutrality condition $q_+N_+ = q_-N_-$. Imposing this condition before going to the grand-canonical ensemble makes, in general, the calculations much more difficult, if not impossible. Later, as we obtain the low-density expansion, this will be imposed order-by-order in a consistent way—any infinities arising from the non-neutrality of the system will be then (automatically) canceled.

In its full form, $\mathcal{Q}$ reads

$$\mathcal{Q} = \int \frac{\mathcal{D}\psi_+ \, \mathcal{D}\psi_-}{\mathcal{Z}_\psi}\frac{D\phi}{\mathcal{Z}_\phi} \, \exp\left(\bar{\mathcal{H}}_0 + \lambda_+\int \mathrm{d}\mathbf{r} \, h_+(\mathbf{r})\mathrm{e}^{-\imath q_+\phi(\mathbf{r})} + \lambda_-\int \mathrm{d}\mathbf{r} \, h_-(\mathbf{r})\mathrm{e}^{\imath q_-\phi(\mathbf{r})}\right), \tag{6.14}$$

where $\bar{\mathcal{H}}_0$ is given in Eq. (6.7). We defined

$$h_\alpha(\mathbf{r}) \equiv \exp\Big(\frac{1}{2}\big[\omega_{\alpha\alpha}(0) + q_\alpha^2 v_c(0)\big] - \imath q_\alpha\psi_\alpha(\mathbf{r})\Big) \tag{6.15}$$

(as before, α stands for both $+$ and $-$).

Introducing the Debye-Hückel propagator,

$$v_{\mathrm{DH}}^{-1}(\mathbf{r}-\mathbf{r}') = v_c^{-1}(\mathbf{r}-\mathbf{r}') + I_2\delta(\mathbf{r}-\mathbf{r}') \tag{6.16}$$

(with $I_2 = q_+^2\lambda_+ + q_-^2\lambda_-$), and doing some algebraic manipulations, we finally arrive to the grand-canonical free energy density. It is defined through $g \equiv -\ln\big(\mathcal{Q}\big)/V$, and reads

$$g = -\lambda_+ - \lambda_- - \frac{1}{2}I_2 v_c(0) - \frac{1}{V}\ln\Big(\frac{\mathcal{Z}_{\mathrm{DH}}}{\mathcal{Z}_\phi}\Big) - \frac{1}{V}\ln\Big\langle \mathrm{e}^{\lambda_+\int \mathrm{d}\mathbf{r} \, Q_+(\mathbf{r}) + \lambda_-\int \mathrm{d}\mathbf{r} \, Q_-(\mathbf{r})}\Big\rangle, \tag{6.17}$$

where V is the volume of the system and the brackets $\langle\cdots\rangle$ denote averages where $\omega_{\alpha\beta}^{-1}$ and v_{DH}^{-1} are the propagators. $\mathcal{Z}_{\mathrm{DH}}$ is defined as $\mathcal{Z}_\phi$ in Eq. (6.12), but having v_{DH}^{-1} instead of v_c^{-1} as propagator. The functions $Q_+(\mathbf{r})$ and $Q_-(\mathbf{r})$ are

$$Q_\alpha(\mathbf{r}) = h_\alpha(\mathbf{r})\mathrm{e}^{-\imath\alpha \, q_\alpha\phi(\mathbf{r})} - 1 + \frac{1}{2}q_\alpha^2\phi^2(\mathbf{r}) - \frac{1}{2}q_\alpha^2 v_c(0). \tag{6.18}$$

With the preceding steps we have obtained the exact expression for the grand-canonical free energy density g (still without imposing electroneutrality). With this, we have what we need to obtain the low-density expansion of the *canonical* free energy. In order to do so, we will (i) expand g in powers of λ_+ and λ_- (up to a order $5/2$), (ii) calculate the concentrations of positive and negative particles and impose electroneutrality *consistently*, order-by-order, and (iii) make a Legendre transformation back to the canonical ensemble.

6.2.1 Expanding g in powers of λ

We start the power-expansion of g by noting that the Fourier transform of the Coulomb potential is $\widetilde{v}_c(\mathbf{k}) = 4\pi\ell_B/k^2$. Using this, one is able to express $v_c(0)$ as

$$v_c(0) = \int \frac{\mathrm{d}\mathbf{k}}{(2\pi)^3}\frac{4\pi\ell_B}{k^2}. \tag{6.19}$$

Since both $\mathcal{Z}_{\mathrm{DH}}$ and $\mathcal{Z}_\phi$ are Gaussian (path) integrals, it is easy to show that

$$\frac{1}{V}\ln\left(\frac{\mathcal{Z}_{\mathrm{DH}}}{\mathcal{Z}_\phi}\right) = -\frac{1}{2}\int \frac{\mathrm{d}\mathbf{k}}{(2\pi)^3}\ln\left(1+\frac{4\pi\ell_B I_2}{k^2}\right). \tag{6.20}$$

Using Eqs. (6.19) and (6.20), we find

$$\frac{1}{2}I_2 v_c(0) + \frac{1}{V}\ln\left(\frac{\mathcal{Z}_{\mathrm{DH}}}{\mathcal{Z}_\phi}\right) = \frac{1}{12\pi}\Big[4\pi\ell_B I_2\Big]^{3/2}. \tag{6.21}$$

Introducing the dimensionless quantity $\Delta v_0 = \sqrt{4\pi\ell_B^3 I_2}$ and doing a cumulant expansion in $Q_+(\mathbf{r})$ and $Q_-(\mathbf{r})$ of the last term on rhs of Eq. (6.17), we get

$$g = -\lambda_+ - \lambda_- - \frac{\Delta v_0^3}{12\pi\ell_B^3} - \lambda_+ Z_1^+ - \lambda_- Z_1^- - \frac{\lambda_+^2}{2}Z_2^{++} - \frac{\lambda_-^2}{2}Z_2^{--} - \lambda_+\lambda_- Z_2^{+-} + O(\lambda^3), \tag{6.22}$$

with

$$Z_1^+ = \frac{1}{V}\int \mathrm{d}\mathbf{r}\,\big\langle Q_+(\mathbf{r})\big\rangle \tag{6.23}$$

and analogous formula for Z_1^-, and

$$Z_2^{++} = \frac{1}{V}\int \mathrm{d}\mathbf{r}\mathrm{d}\mathbf{r}'\Big\{\big\langle Q_+(\mathbf{r})Q_+(\mathbf{r}')\big\rangle - \big\langle Q_+(\mathbf{r})\big\rangle\big\langle Q_+(\mathbf{r}')\big\rangle\Big\} \tag{6.24}$$

and similar formulas for Z_2^{--} and Z_2^{+-}.

The symbol $O(\lambda^3)$ in Eq. (6.22) means that any other contribution to the expansion will be of the order 3 or higher, i.e., with terms like λ_+^3, $\lambda_+^2\lambda_-$, etc. We will expand g up to the order immediately below 3, which turns out to be $5/2$, as we will demonstrate. In order to do so, we need first to calculate the coefficients Z_1^+, etc., in Eq. (6.22). In order to do so, we need the averages given in appendix (cf. Eq. (D.1–D.5)). Noticing that $v_c(0) - v_{\mathrm{DH}}(0) = \Delta v_0$, we obtain

$$Z_1^\alpha = \mathrm{e}^{q_\alpha^2\Delta v_0/2} - 1 - \frac{1}{2}q_\alpha^2\Delta v_0 \tag{6.25}$$

and

$$Z_2^{\alpha\beta} = \int \mathrm{d}\mathbf{r} \left\{ \mathrm{e}^{[q_\alpha^2+q_\beta^2]\Delta v_0/2} \Big[\mathrm{e}^{-\omega_{\alpha\beta}(\mathbf{r})-\alpha\beta\, q_\alpha q_\beta v_{\mathrm{DH}}(\mathbf{r})} - 1 \Big] \right.$$
$$\left. + \frac{1}{2} q_\alpha^2 q_\beta^2 v_{\mathrm{DH}}^2(\mathbf{r}) \Big[1 - \mathrm{e}^{q_\alpha^2 \Delta v_0/2} - \mathrm{e}^{q_\beta^2 \Delta v_0/2} \Big] \right\}. \quad (6.26)$$

We remind that

$$v_{\mathrm{DH}}(\mathbf{r}) = \frac{\ell_B}{r} \mathrm{e}^{-\Delta v_0 r/\ell_B} \quad (6.27)$$

was defined (through its inverse) in Eq. (6.16). We now introduce the hard-core through the short-range potentials, i.e,

$$\omega_{\alpha\beta}(\mathbf{r}) = \begin{cases} +\infty & \text{if } r < \big(d_\alpha + d_\beta\big)/2, \\ 0 & \text{otherwise,} \end{cases} \quad (6.28)$$

where the indices α and β stand again for $+$ and $-$; d_+ and d_- are respectively the (effective) ionic diameters of the positive and negative particles.

The expressions for Z_1^+, etc., do depend on λ_+ and λ_-. In order to have a consistent expansion of g in the fugacities, one should also expand Eqs. (6.25–6.26) in λ_+ and λ_-, up to the relevant order, before using them in g, Eq. (6.22). By doing this consistently up to order $5/2$ in the fugacities, one obtains

$$\widetilde{g} \equiv d_+^3 g = -\widetilde{\lambda}_+ - \widetilde{\lambda}_- - m_1 \widetilde{\lambda}_+^2 - m_2 \widetilde{\lambda}_-^2 - m_3 \widetilde{\lambda}_+ \widetilde{\lambda}_- - \Big[n_1 \widetilde{\lambda}_+^2 + n_2 \widetilde{\lambda}_-^2 + n_3 \widetilde{\lambda}_+ \widetilde{\lambda}_- \Big] \Delta v_0$$
$$- \Big[p_1 \widetilde{\lambda}_+^2 + p_2 \widetilde{\lambda}_-^2 + p_3 \widetilde{\lambda}_+ \widetilde{\lambda}_- \Big] \ln \Delta v_0 - \Big[r_1 \widetilde{\lambda}_+^2 + r_2 \widetilde{\lambda}_-^2 + r_3 \widetilde{\lambda}_+ \widetilde{\lambda}_- \Big] \Delta v_0 \ln \Delta v_0$$
$$- \Big[s_1 \widetilde{\lambda}_+ + s_2 \widetilde{\lambda}_- \Big] \Delta v_0^2 - \Big[t_0 + t_1 \widetilde{\lambda}_+ + t_2 \widetilde{\lambda}_- \Big] \Delta v_0^3 + \Omega_0 \Big[q_+ \widetilde{\lambda}_+ - q_- \widetilde{\lambda}_- \Big]$$
$$- \Delta v_0 \left\{ \Omega_1 \Big[q_+ \widetilde{\lambda}_+ - q_- \widetilde{\lambda}_- \Big]^2 - \Omega_0 \Big[q_+^4 \widetilde{\lambda}_+^2 + q_-^4 \widetilde{\lambda}_-^2 \right.$$
$$\left. - 2 q_+ q_- \Big[\frac{q_+^2 + q_-^2}{2} \Big] \widetilde{\lambda}_+ \widetilde{\lambda}_- \Big] \right\} + O(\lambda^3), \quad (6.29)$$

where we used the (dimensionless) variables $\widetilde{\lambda}_+ \equiv d_+^3 \lambda_+$ and $\widetilde{\lambda}_- \equiv d_+^3 \lambda_-$. In this expansion, Δv_0 is taken as a term scaling like $\widetilde{\lambda}^{1/2}$. The coefficients m_1, etc. are given explicitly in appendix (cf. Eqs. (D.7–D.16)).

The coefficients Ω_0 and Ω_1 are given by the divergent integrals

$$\Omega_0 = 2\pi \ell_B \int_0^\infty \mathrm{d}r\, r\,, \qquad \Omega_1 = 2\pi \int_0^\infty \mathrm{d}r\, r^2. \quad (6.30)$$

These terms are present in Eq. (6.29) because global charge neutrality has not been yet demanded. By imposing this condition, these divergent terms cancel exactly. This is what we show next.

6.2.2 Imposing electroneutrality

The electroneutrality condition says that the global charge of the system is zero, i.e., $q_+N_+ = q_-N_-$. In the grand-canonical ensemble, N_+ and N_- are no longer fixed numbers but average values. This means that the electroneutrality condition is now given by

$$q_+\langle N_+\rangle = q_-\langle N_-\rangle. \tag{6.31}$$

Defining $\widetilde{c}_+ = d_+^3\langle N_+\rangle/V$, it is easy to show that

$$\widetilde{c}_+ = -\widetilde{\lambda}_+\frac{\partial\widetilde{g}}{\partial\widetilde{\lambda}_+} \tag{6.32}$$

with an analogous formula for $\widetilde{c}_-$; $\widetilde{c}_+$ is the volume fractions of the positive ions (notice that it is also usual to define $\pi\widetilde{c}_+/6$ as the volume fraction). As one imposes Eq. (6.31), the fugacities will depend on each other in a non-trivial way such that the system is, on average, neutral. If the system were totally symmetric (i.e., $q_+ = q_-$ and $d_+ = d_-$), this dependence would be given by the relation $\widetilde{\lambda}_+ = \widetilde{\lambda}_-$[82]. However, this is not the case here: we need to find the relation between the fugacities in an order-by-order basis.

First, we assume that $\widetilde{\lambda}_-$ can be expanded in terms of $\widetilde{\lambda}_+$ such that

$$\widetilde{\lambda}_- = a_0\widetilde{\lambda}_+ + a_1\widetilde{\lambda}_+^{3/2} + a_2\widetilde{\lambda}_+^2 + a_3\widetilde{\lambda}_+^2\ln\widetilde{\lambda}_+ + a_4\widetilde{\lambda}_+^{5/2} + a_5\widetilde{\lambda}_+^{5/2}\ln\widetilde{\lambda}_+ + O(\widetilde{\lambda}_+^3). \tag{6.33}$$

This is naturally inspired by the expanded form of the grand-canonical free energy $\widetilde{g}$. After calculating $\widetilde{c}_+$ and $\widetilde{c}_-$ from $\widetilde{g}$ (Eq. (6.29)) and putting it into the electroneutrality condition (Eq. (6.31)), we substitute the occurring $\widetilde{\lambda}_-$ for its expanded form—given by Eq. (6.33)—in a consistent way, i.e., the terms of order $\widetilde{\lambda}_+^3$ or higher are not taken into account. This operation leads to the expanded form (up $\widetilde{\lambda}_+^{5/2}\ln\widetilde{\lambda}_+$) of the electroneutrality condition. Solving it consistently, order-by-order, yields the values of a_0, etc., that keep the system globally neutral. For instance, at $\widetilde{\lambda}_+$ level, the expanded form of Eq. (6.31) reads

$$q_+ - a_0q_- = 0, \tag{6.34}$$

which naturally gives $a_0 = q_+/q_-$. With the knowledge of a_0, we can then solve the next-order term (in this case $\widetilde{\lambda}_+^{3/2}$) and obtain the value of a_1, and so on. The resulting coefficients a_0 up to a_5 are given in appendix (cf. Eqs. (D.17–D.22)).

As this order-by-order neutrality condition is imposed, one notices that the terms in Ω_0 and Ω_1 in Eq. (6.29) are exactly canceled in a natural way, without any further assumptions. The resulting expression for $\widetilde{g}$, now expanded only in one of the fugacities (in this case $\widetilde{\lambda}_+$), is then a well behaved expansion (its full expression is quite lengthy, and for this reason we will not show it here). With this, we are ready for the last step in our calculation, i.e., we can transform back to the canonical ensemble through a Legendre transform.

6.2.3 Low-density expansion: results

We obtained in the last Subsection the grand-canonical free energy $\widetilde{g}$ as an expansion on one of the fugacities (we chose $\widetilde{\lambda}_+$), such that the system is globally neutral. In order to go back to the

canonical ensemble, we use the Legendre transform, which in our case is

$$\widetilde{f} = \widetilde{g} + \widetilde{c}_+ \ln \widetilde{\lambda}_+ + \widetilde{c}_- \ln\big(\widetilde{\lambda}_-\big), \tag{6.35}$$

where $\widetilde{f} \equiv d_+^3 F/V k_B T$, with F as the canonical free energy. Notice that now $\widetilde{\lambda}_-$ is a function of $\widetilde{\lambda}_+$ according to Eq. (6.33).

The first step to obtain $\widetilde{f}$ is to invert the expression given in Eq. (6.32) such that $\widetilde{\lambda}_+$ is obtained as an expansion on $\widetilde{c}_+$. For consistency reasons, one should not retain, in this expansion, any terms of order $\widetilde{c}_+^3$ or higher. With this, we obtain $\widetilde{\lambda}_+ = \widetilde{\lambda}_+(\widetilde{c}_+)$: plugging this consistently into Eq.(6.35), we finally obtain $\widetilde{f}$, which reads

$$\widetilde{f} = \widetilde{f}_{\rm id} + B_{\rm DH}\widetilde{c}_+^{3/2} + B_2\widetilde{c}_+^2 + B_{2\log}\widetilde{c}_+^2 \ln \widetilde{c}_+ + B_{5/2}\widetilde{c}_+^{5/2} + B_{5/2\log}\widetilde{c}_+^{5/2} \ln \widetilde{c}_+ + O\big(c_+^3\big). \tag{6.36}$$

Defining $\eta \equiv q_-/q_+$, $\xi \equiv d_-/d_+$ and the coupling parameter $\epsilon_+ \equiv q_+^2 \ell_B/d_+$ (which is the ratio between the Coulomb energy at contact between two positive ions and the thermal energy $k_B T$), the coefficients in Eq. (6.36) can be explicitly written as

$$\widetilde{f}_{\rm id} = \widetilde{c}_+ \ln \widetilde{c}_+ + \frac{\widetilde{c}_+}{\eta} \ln\Big(\frac{\widetilde{c}_+}{\eta}\Big) - \Big[1 + \frac{1}{\eta}\Big]\widetilde{c}_+ \tag{6.37}$$

which is the ideal contribution to the free energy,

$$B_{\rm DH} = -\frac{2}{3}\sqrt{\pi \epsilon_+^3 [1+\eta]^3} \tag{6.38}$$

which is the coefficient of the Debye-Hückel limiting law term (order $3/2$ in $\widetilde{c}_+$). The higher order coefficients are

$$\begin{aligned} B_2 = -\frac{\pi}{3}\epsilon_+^3 \Bigg\{ & -H(\epsilon_+) - \ln \epsilon_+ + 2\eta^2 \left[H\Big(-\frac{2\eta\epsilon_+}{1+\xi}\Big) + \ln\Big(\frac{2\eta\epsilon_+}{1+\xi}\Big)\right] \\ & - \eta^4 \left[H\Big(\frac{\eta^2\epsilon_+}{\xi}\Big) + \ln\Big(\frac{\eta^2\epsilon_+}{\xi}\Big)\right] - 2\eta^2\big[1-\eta^2\big]\ln\eta \\ & + \frac{1}{2}\big[1-\eta^2\big]^2 \ln\big(36\pi\epsilon_+^3[1+\eta]\big) \Bigg\} \end{aligned} \tag{6.39}$$

(the function $H(x)$—not to be confused with the Hamiltonian—is given by Eq. (D.6)),

$$B_{2\log} = -\frac{\pi}{6}\epsilon_+^3\big[1-\eta^2\big]^2, \tag{6.40}$$

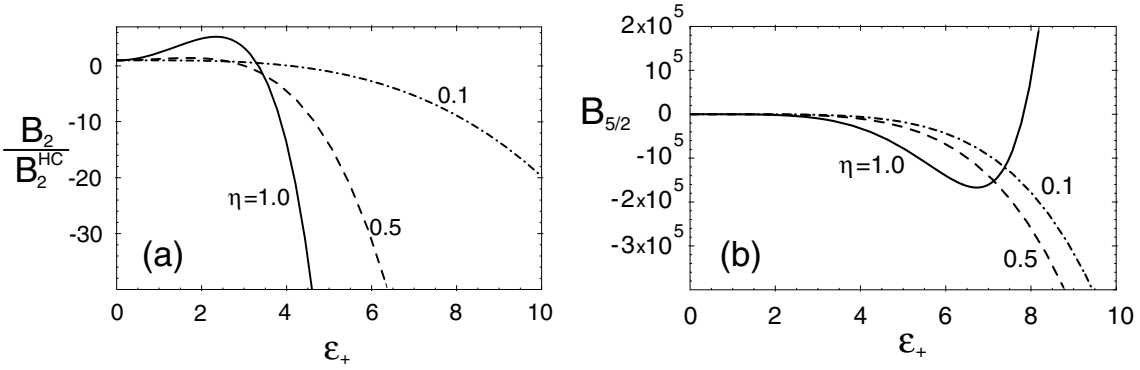

Figure 6.2: Coefficients (a) B_2 and (b) $B_{5/2}$ of the free energy Eq. (6.36) as functions of ϵ_+ for different values of $\eta \equiv q_-/q_+$ (with $d_+ = d_-$). Notice that B_2 is normalized to the second virial of a pure two-component hard-core gas.

$$B_{5/2} = \frac{2}{3}\big[\pi\epsilon_+^3\big]^{3/2}\big[1+\eta\big]^{1/2}\Bigg\{\frac{5}{8} + H\big(\epsilon_+\big) + \ln\big(\epsilon_+\big) + \eta^6\Bigg[\frac{5}{8} + H\Big(\frac{\eta^2\epsilon_+}{\xi}\Big) + \ln\Big(\frac{\eta^2\epsilon_+}{\xi}\Big)\Bigg] + 2\eta^3\Bigg[\frac{5}{8} + H\Big(-\frac{2\eta\epsilon_+}{1+\xi}\Big) + \ln\Big(\frac{2\eta\epsilon_+}{1+\xi}\Big)\Bigg] + \frac{1}{8}\big[1+\eta\big]^2\big[5 - 12\eta + 17\eta^2 - 12\eta^3 + 5\eta^4\big] - 2\eta^3\big[1+\eta^3\big]\ln\eta - \frac{1}{2}\big[1+\eta^3\big]^2\ln\Big(64\pi\epsilon_+^3\big[1+\eta\big]\Big)\Bigg\} \quad (6.41)$$

and

$$B_{5/2\log} = -\frac{1}{3}\big[\pi\epsilon_+^3\big]^{3/2}\big[1+\eta\big]^{1/2}\big[1+\eta^3\big]^2. \quad (6.42)$$

The free energy Eq. (6.36) is the exact low density expansion of the asymmetric TCPHC. The only parameter that is demanded to be small is $\widetilde{c}_+$; the other parameters, viz. ϵ_+, η and ξ can have any value. We have chosen the positive ions as the "reference species" (i.e., the expansion is done with respect to $\widetilde{c}_+$) without any loss of generality, since the relation between $\widetilde{c}_+$ and $\widetilde{c}_-$ is fixed through the electroneutrality condition. As consistency checks, we notice that the expansion $\widetilde{f}$ is symmetric, as expected, with respect to the simultaneous exchange d_+ with d_- and q_+ with q_-. Also, in the limit $d_+ = d_-$ and $q_+ = q_-$, we obtain the same expression as previously calculated in Ref. [82] for totally symmetric systems. Finally, as one turns-off the charges in the system (or equivalently, as one takes the limit $\epsilon_+ \to 0$), the pure hard-core fluid is recovered, i.e., $\widetilde{f}$ becomes the usual virial expansion with $B_{3/2}$ and $B_{5/2}$ equal to zero and B_2 equals the second virial of a two-component hard-core gas. This limit can be also understood as the high-temperature regime: as the thermal energy largely exceeds the Coulomb energy at contact, the hard core interaction becomes the only relevant interaction between the particles.

The behavior of the coefficients B_2 and $B_{5/2}$ as functions of the coupling parameter ϵ_+ are depicted in Figs. (6.2) and (6.3). In Fig. (6.2) the ionic diameters of positive and negative ions are kept equal ($d_+ = d_-$) and the ratio between the charge valences (η) is varied, while in Fig. (6.3) the charge valences are equal and the ratio between the ionic diameters is varied. These figures

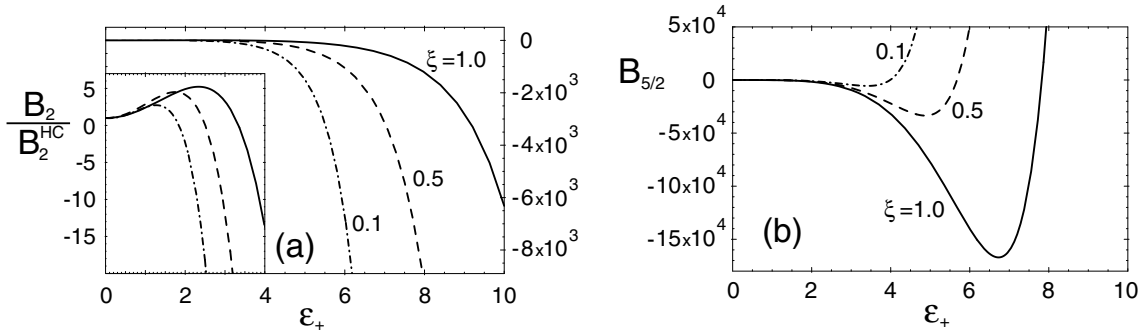

Figure 6.3: Coefficients (a) B_2 and (b) $B_{5/2}$ of the free energy Eq. (6.36) as functions of ϵ_+ for different values of $\xi \equiv d_-/d_+$ (with $q_+ = q_-$). Notice that B_2 is normalized to the second virial of a pure two-component hard-core gas. The inset in (a) shows the behavior of B_2 close to $\epsilon_+ = 0$ in a different scale.

highlight the fact that that both coefficients diverge as ϵ_+ goes to infinity. In this limit,

$$B_2 \approx -\frac{\pi}{4}\frac{[1+\xi]^4}{\eta^2}\frac{1}{\epsilon_+}\exp\Big(\frac{2\eta\epsilon_+}{1+\xi}\Big) \tag{6.43}$$

and

$$B_{5/2} \approx \frac{\pi^{3/2}}{2}\frac{[1+\xi]^4\sqrt{1+\eta}}{\eta}\sqrt{\epsilon_+}\exp\Big(\frac{2\eta\epsilon_+}{1+\xi}\Big). \tag{6.44}$$

Note that $B_{5/2}$ diverges faster (and with opposite sign) than B_2. If the higher order terms have a similar behavior, i.e., if B_3 also diverges faster than $B_{5/2}$ and so on, then one can conclude that the inclusion of higher order terms will not yield better results at high couplings and higher concentrations. Naturally this can only be confirmed with the actual calculation of more terms in the series.

As a final note, we mention that the exponential divergent behavior of B_2 and $B_{5/2}$ when $\epsilon_+ \to \infty$ is due to the increasing importance of the interaction between oppositely charged particles (ionic pairing) as the coupling parameter increases[13, 32, 119], corresponding for instance to lower temperatures. This is justified by noting that the argument in the exponential occurring in both asymptotic forms Eqs. (6.43) and (6.44), viz. $2\,\eta\,\epsilon_+/[1+\xi]$, can be re-expressed as $2\,q_+\,q_-\,\ell_B/[d_+ + d_-]$, which translates the coupling between positive and negative ions (in this case, the ratio between the Coulomb contact energy between oppositely charged ions and the thermal energy k_BT).

6.3 Applications

6.3.1 Colloids

In many colloidal suspensions, flocculation or coagulation (due to the attractive van der Waals interaction between colloidal particles) is prevented by the presence of repulsive electrostatic forces. These suspensions are generally dilute, with volume fractions of colloidal particles usually not higher than a few percent. The macro-particles normally have dimensions ranging from 10 to 1000 nm and charges of several thousands e (elementary charge), with much smaller counterions

that have a charge of a few e. In other words, in such systems the charge and size asymmetry between ions and counterions is very important.

In such dilute solutions, it is reasonable to neglect the van der Waals interactions between the colloidal particles. To see this, let us assume an homogeneous system with $\sim 1\%$ volume fraction ($\widetilde{c}_+ \sim 10^{-2}$); the particles will be typically at distances $\sim 6\,d_+$ (center-to-center distance). The ratio between the van der Waals and the Coulomb interactions at this distance would then be approximately given by

$$\frac{|v_{vdW}|}{|v_c|} \sim \frac{\mathcal{A}}{20\,\epsilon_+} \tag{6.45}$$

where $\mathcal{A}$ is Hamaker constant (in units of $k_B\,T$), and the van der Waals interaction is assumed to be between to equal-sized spheres of diameter d_+[47]. In colloidal suspensions, ϵ_+ is typically very large (at least a few hundreds) while $\mathcal{A} \sim 20$; in other words, the ratio above is small, and the Coulomb interaction is dominant. With such typical distances, it is also true that the hard cores will not play a significant role when considering the interaction between the macro-particles. Its role, as usual, is to prevent oppositely charged particles to collapse on each other; the size asymmetry gives some mathematical sense to the very large difference in sizes between the colloidal particles and their counterions. With this in mind, a very asymmetric TCPHC can be regarded a good model for some dilute colloidal suspensions, and the free energy Eq. (6.36) can be used to characterize such systems.

Still motivated by the colloidal suspensions, we now take the following limit: assume d_+, q_+ and $\widetilde{c}_+$ fixed, and make both $\eta \equiv q_-/q_+$ and $\xi \equiv d_-/d_+$ vanishingly small (this has to be done with some care, since $\eta = 0$ is not well-defined—no electroneutrality). One can then rewrite the free energy Eq. (6.36) up to second order in $\widetilde{c}$ as

$$\widetilde{f} \approx \widetilde{f}_0 + B^c_{\rm DH}\widetilde{c}_+^{3/2} + B^c_2\widetilde{c}_+^2 + B^c_{\rm 2log}\widetilde{c}_+^2\log\widetilde{c}_+ + O(\widetilde{c}_+^{5/2}) \tag{6.46}$$

where

$$\widetilde{f}_0 = \widetilde{c}_+\ln\widetilde{c}_+ + \frac{\widetilde{c}_+}{\eta}\ln\Big(\frac{\widetilde{c}_+}{\eta}\Big) - \Big[1+\frac{1}{\eta}\Big]\widetilde{c}_+ + \frac{\pi}{3}\left[\frac{2\xi^3}{\eta^2} + \frac{[1+\xi]^3}{2\eta}\right]\widetilde{c}_+^2, \tag{6.47}$$

corresponding to the ideal term (for both macro- and counterions) and to the second virial of the counterion–counterion and macroion–counterion hard-core interaction. This term is independent of ϵ_+, i.e., it is independent of the electrostatic interaction. The coefficients $B^c_{\rm DH}$, etc. are given by

$$B^c_{\rm DH} = -\frac{2}{3}\sqrt{\pi\epsilon_+^3}, \tag{6.48}$$

$$B^c_2 = \frac{\pi}{3}\epsilon_+^3\Big\{H\big(\epsilon_+\big) - \frac{1}{2}\ln\big(36\pi\epsilon_+\big)\Big\} + \frac{\pi}{2}\epsilon_+, \tag{6.49}$$

$$B^c_{\rm 2log} \approx -\frac{\pi}{6}\epsilon_+^3. \tag{6.50}$$

This limit was taken at fixed values of ϵ_+ and $\widetilde{c}_+$. In other words, by separating $\widetilde{f}_0$—which contains terms that diverge with $1/\eta$—from the other contributions to the free energy—which are only dependent on the *fixed* parameters ϵ_+ and $\widetilde{c}_+$—we are showing that for dilute colloidal systems it is the ideal contribution of the counterions that dominates the free energy, and cannot

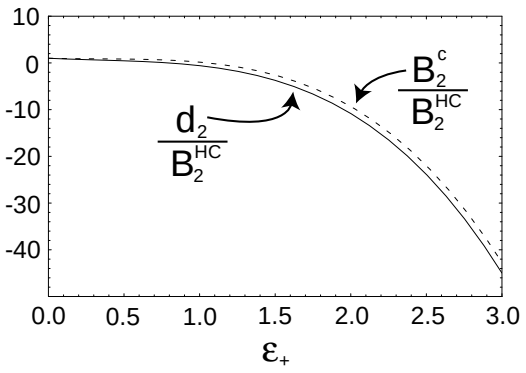

Figure 6.4: Coefficients B_2^c (Eq. (6.52)) and d_2 (pure OCPHC from Ref. [82]) as functions of the coupling ϵ_+. Notice that both coefficients are normalized to the second virial of a pure one-component hard-core gas.

be neglected. Effects due to the electrostatic interaction become, in this sense and up to this order, a true perturbation to the ideal behavior.

At this point, we make a parentheses to briefly introduce another model that is also widely used to describe charged systems. It is the one-component plasma (OCP), which in its simplest form consists of a collection of N equally charged particles immersed in a neutralizing background that assures the global charge neutrality of the system (in the TCPHC electroneutrality is assured by oppositely charged particles). The OCP, or its quantum mechanical counter-part "jellium," has been used to describe degenerate stellar matter (interior of white dwarfs and outer layer of neutron stars) and the interior of massive planets like Jupiter[46]; in condensed matter physics, jellium is often used as a reference state when calculating the electronic structure of solids[46, 11]. The simplicity of the OCP made it a model of choice, with results obtained with many different techniques, from extensions to the Mayer expansion[1, 22, 39] to Monte Carlo simulations[18, 44, 105, 106], as well as integral-equation theory[35, 56, 67] and modifications to the Debye-Hückel theory[85, 89], to mention a few. For good reviews see Refs. [46, 11].

When the particles have a hard core, the OCP is called one-component hard-core plasma (OCPHC): what we will see next is that the electrostatic contribution to the free energy in dilute colloidal suspensions can be almost described through the OCPHC. If we compare the coefficients Eqs. (6.48–6.50) with the ones previously obtained[82] for the OCPHC (cf. Eqs. (51), (56) and (57) of Ref. [82]), we see that

$$B_{\mathrm{DH}}^c = d_{3/2}, \tag{6.51}$$

$$B_2^c = d_2 + \frac{\pi}{2}\epsilon_+ \tag{6.52}$$

and

$$B_{2\log}^c = d_{\ln 2}, \tag{6.53}$$

where the notation used in Ref. [82] is kept on the rhs of Eqs. (6.51–6.53). The comparison between B_2^c and d_2 is shown in Fig. (6.4). This shows that, up to the order $\widetilde{c}_+^2 \ln \widetilde{c}_+$ (i.e., for very dilute colloidal suspension), the OCPHC is almost completely recovered.

This is in fact what one would intuitively expect: each macroion has around it a very large number of small neutralizing counterions which act like a background. However, there is a small

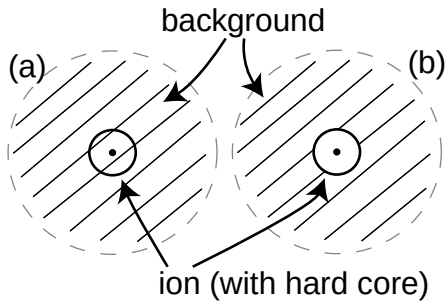

Figure 6.5: A particle (with diameter d_+ and charge valence q_+) in the OCPHC model with and without the penetrating background.

difference between the TCPHC in this limit and the OCPHC: in the latter, the background penetrates the particles, while in the TCPHC it cannot[115, 11]. In our calculation, this is reflected in the $\widetilde{c}_+^2$ term, where $\pi\epsilon_+/2$ is the positive extra cost in the free energy that the OCPHC has to pay (at this order) to expel the background from the hard-core particles. A formal proof of this would require the re-calculation of the OCPHC with the constrained background, which is outside the scope of this calculation. We can however motivate this conclusion: assume that the OCPHC is very dilute, such that each particle and its neighboring background form a neutral entity (in the spirit of the cell model, see for instance Ref. [4]) that can be regarded independent from the other particles. The background is assumed to have no entropy, and so the free energy difference per particle between a system without penetrating background and with penetrating background can be obtained from the difference in the self-energies. Assuming (cf. Fig 6.5) $\hat{\rho}_a(\mathbf{r}) = q_+\delta(\mathbf{r}) - \rho_0$ and $\hat{\rho}_b(\mathbf{r}) = q_+\delta(\mathbf{r}) - \rho_0\big[1-\theta(d_+/2-r)\big]$ (where $\rho_0 = c_+q_+$ is the background concentration and $\theta(x) = 1$ if $x > 0$ and 0 otherwise), this difference reads

$$\begin{aligned}\frac{\Delta F}{Nk_BT} =& \frac{1}{2}\int \mathrm{d}\mathbf{r}\mathrm{d}\mathbf{r}'\left\{\hat{\rho}_b(\mathbf{r})v_c(\mathbf{r}-\mathbf{r}')\hat{\rho}_b(\mathbf{r}') - \hat{\rho}_a(\mathbf{r})v_c(\mathbf{r}-\mathbf{r}')\hat{\rho}_a(\mathbf{r}')\right\} = \\ =& \rho_0 q_+ 4\pi\ell_B\int_0^{d_+/2}\mathrm{d}r\, r + O(c_+^2) = \\ =& \frac{\pi}{2}\widetilde{c}_+\epsilon_+ + O(c_+^2).\end{aligned} \tag{6.54}$$

From this follows that the free energy difference (per volume) is $\Delta\widetilde{f} = \pi\widetilde{c}_+^2\epsilon_+/2$. Note that this is a positive contribution to the $\widetilde{c}^2$ term with the same coefficient as the extra term in Eq. (6.49); this is what one would have to add to the OCPHC to account, at this order, for the exclusion of the background from the hard core of the particles. In other words, we have shown that in the colloidal limit, the electrostatic contribution to the free energy of the TCPHC maps exactly, up to this order, into the one obtained for the OCPHC (with excluded background from the particles).

6.3.2 Ionic activity and radii

In electrochemistry, it is usual to define the mean activity of an electrolyte as

$$\lambda_\pm \equiv \left[\lambda_+^{q_-}\lambda_-^{q_+}\right]^{1/[q_+ + q_-]}, \tag{6.55}$$

where λ_+ and λ_- are respectively the fugacities of the positive and the negative ions. The mean activity coefficient $\mathrm{f}_\pm$ is the ratio between the mean activity of the electrolyte and of an ideal gas, which is in general given by

$$\mathrm{f}_\pm = \exp\Big(\frac{q_-}{q_+ + q_-}\frac{\partial \widetilde{f}_{\mathrm{ex}}}{\partial \widetilde{c}_+}\Big), \tag{6.56}$$

for a two-component system where the positively charged particles were used as reference species, in the same way as in Eq. (6.36); $\widetilde{f}_{\mathrm{ex}}$ is the difference between the full free energy and the free energy of an ideal gas, i.e., $\widetilde{f}_{\mathrm{ex}} = \widetilde{f} - \widetilde{f}_{\mathrm{id}}$, also known as excess free energy.

There are different ways of measuring $\mathrm{f}_\pm$, as for instance, through the change on the freezing point of the solvent (usually water) with the addition of salt[98], or by measuring the change on the potential difference between the electrodes of a concentration cell as salt is added[19, 98] (potentiometry), or by direct measurement of the solvent activity through vapor exchange between a solution with known activity and the sample[97, 98] (isopiestic). Although dating from the early nineteen hundreds, these are still the most common techniques used today, especially the potentiometry, which is regarded as the most precise technique of all. The values of $\mathrm{f}_\pm$ are tabled as function of the salt concentration for many electrolytes[23, 88, 92, 98].

From the free energy Eq. (6.36) and the definition Eq. (6.56) we can get the low density expansion for the mean activity coefficient of a $q_+ : q_-$ salt. To compare with experimental results, it is useful to note that $\widetilde{c}_+ = 6.022 \times 10^{-4} q_- d_+^3 \varrho$, where d_+ is in Ångströms and ϱ is the salt concentration in moles/liter. After the appropriate expansion, $\mathrm{f}_\pm$ reads

$$\mathrm{f}_\pm = 1 + \nu_{\mathrm{DH}}\varrho^{1/2} + \nu_1 \varrho + \nu_{1\log}\varrho \ln \varrho + \nu_{3/2}\varrho^{3/2} + \nu_{3/2\log}\varrho^{3/2}\ln\varrho + O(\varrho^2) \tag{6.57}$$

(the order $3/2$ in the mean activity coefficient is the one consistent to a free energy up to $5/2$). The coefficients ν_{DH}, ν_1, etc. are given in appendix (cf. Eqs. (D.23–D.27)). At infinite dilution, the mean activity coefficient goes to 1, which is the prediction for an ideal gas. The first correction to the ideal behavior is the term $\nu_{\mathrm{DH}}\varrho^{1/2}$, which is the prediction one gets from the Debye-Hückel limiting law (DHLL), and is independent of the ionic diameters (cf. Eq. (D.23)). This means that there is always a range of concentrations where different salts (but with the same q_+ and q_-) will deviate from ideality, but have the same activity. At higher concentrations, the other terms have to be taken into account, and the ionic sizes begin to play an important role. In fact, as one fixes ℓ_B ($\simeq$ 7.1 Å in water at 25 C) and q_+ and q_- (which depend on the salt), the only free parameters in the rhs of Eq. (6.57) are the ionic diameters d_+ and d_-, which can be used in the theoretical predictions to fit the experimental values. This leads to effective equilibrium values of the ionic diameters (when in solution), which one can call the "thermodynamic diameter", in contrast to the bare[47] (or crystallographic) and the hydrodynamic diameters—obtained from mobility measurements[30].

Fitting assuming one mean diameter

We now show the fitting procedure assuming that $d_+ = d_- = d$, where d is the mean diameter. This assumption has been often used in the past to fit activities to theories based on Debye-Hückel, but modified[98] to account for the ionic sizes (as previously mentioned, the Debye-Hückel limiting law is insensitive to it). Since we force the two diameters to be equal, we only need the

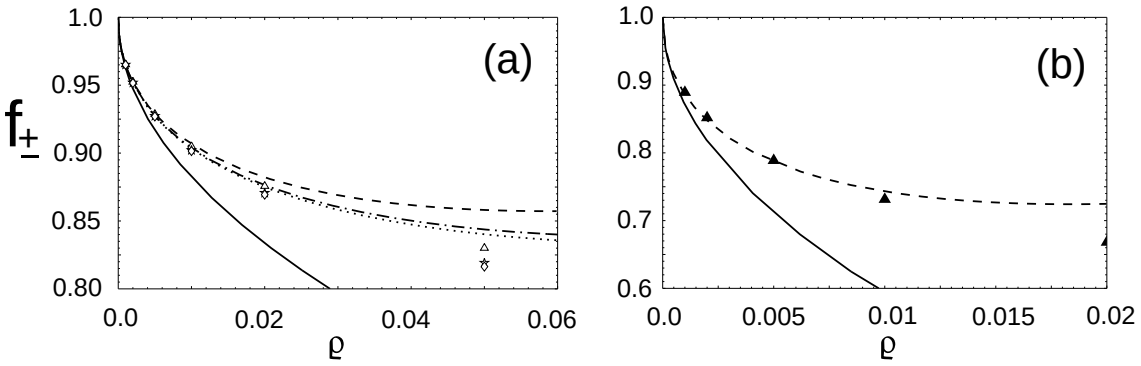

Figure 6.6: Experimental[23] and theoretical mean activity coefficient $\mathrm{f}_\pm$ for various salts as a function of the density ϱ (in mole/liter). Fig. (a) refers to $1:1$ salts, viz. HCl (triangles and dashed line, $d = 4.38$ Å), NaCl (stars and dash-dotted line, $d = 4.00$ Å) and KCl (diamonds and dotted line, $d = 3.90$ Å). Fig. (b) is the same for a $2:1$ salt, viz. $CaCl_2$ (filled triangles and dashed line, $d = 10.8$ Å). In both graphics, the full line denotes the prediction from the DHLL, which is insensitive to the ionic size.

expansion for $f_\pm$ up to linear order: from the experimental data[103, 23] we calculate

$$\Delta \mathrm{f}_\pm \equiv \mathrm{f}_\pm^{exp} - \nu_{\mathrm{DH}} \varrho^{1/2} = \nu_1^{exp} \varrho + O(\varrho^(3/2)). \tag{6.58}$$

By fitting this function we get the coefficient of the linear term ν_1^{exp}, which we then can use to solve the equation $\nu_1(d) = \nu_1^{exp}$, from which d follows. In Fig. 6.6a we show the experimental[103] $f_\pm$ for HCl, NaCl and KCl and the theoretical results, up to linear order in ρ and with the fitted diameters (or distance of approach) 4.38 Å, 4.00 Å and 3.90 Å, respectively. These values are very close to the ones obtained in Ref. [103] with a similar fitting, but using the DH theory with an approximate way to incorporate the ionic sizes. Notice that $d_{\mathrm{HCl}} > d_{\mathrm{NaCl}} > d_{\mathrm{KCl}}$, which is the opposite to what happens with the bare diameters. This is in principle due to the hydration shell, but one should note that the values obtained here are between the bare diameters and the hydrated values available in the literature[47]. In Fig. 6.6b we show the same, but for $CaCl_2$, and with fitted diameter of 10.8 Å. For more asymmetric salts (like $3:1$, etc.) one would need data at lower densities in order to get good results.

Fitting assuming two diameters

If we now assume that both d_+ and d_- are unconstrained, we have to use one more term in the expansion of the activity coefficient and solve the coupled equations

$$\begin{aligned} \nu_1(d_+, d_-) &= \nu_1^{exp} \\ \nu_{3/2}(d_+, d_-) &= \nu_{3/2}^{exp} \end{aligned} \tag{6.59}$$

which can be obtained by fitting the function $\Delta \mathrm{f}_\pm \equiv \mathrm{f}_\pm^{exp} - \nu_{\mathrm{DH}} \varrho^{1/2} - \nu_{1\log} \varrho \ln \varrho = \nu_1 \varrho + \nu_{3/2} \varrho^{3/2} + O(\varrho^{3/2} \ln \varrho)$, or more appropriately,

$$\frac{\Delta \mathrm{f}_\pm}{\varrho} = \nu_1 + \nu_{3/2} \varrho^{1/2}. \tag{6.60}$$

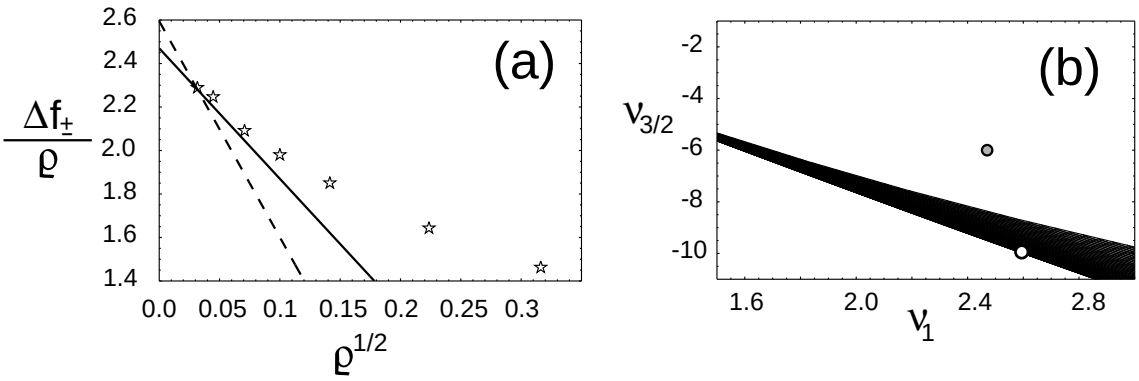

Figure 6.7: Fitting procedure for two unconstrained diameters. (a) asymptotic lines that could describe the experimental values of $\Delta f_\pm/\varrho$ at $\varrho \to 0$ (see text) and (b) their position in the $[\nu_1, \nu_{3/2}]$ plane. The full and dashed lines in (a) lead respectively to the gray and white points in (b). Experimental data from Ref. [23].

What is interesting about this fitting procedure is that the two ionic diameters are independent parameters, that is, the effective sizes obtained through this fitting do not depend on the size of a "reference" ion. The latter is needed, for instance, when ionic sizes are calculated from crystal lattices (also known as the bare ionic diameter[47]), where experimentally one can only measure the distance between the ions, i.e., the sum the ionic radii: a table with the different ionic sizes can be constructed, as long as the absolute size of at least one ionic species is known[100]. The method we show here can potentially give good results for the ionic diameters, as long as there is enough experimental data at very low densities, as we now demonstrate.

In Fig. 6.7a shows $\Delta f_\pm/\varrho$ for NaCl[23] (as a function of $\varrho^{1/2}$), which should approach a line as $\varrho \to 0$. From this, the experimental values of ν_1 and $\nu_{3/2}$ can be extracted: in this particular example we show two possible lines in Fig. 6.7a, viz. $2.47-6.00\varrho^{1/2}$ (full line) and $2.59-9.94\varrho^{1/2}$ (dashed line); notice that in principle both lines could be regarded as the asymptotic limit of the experimental points. As we show next, one of the lines leads to values of ν_1 and $\nu_{3/2}$ that yield reasonable ionic diameters, while the other not.

Fig. 6.7b shows the mapping of the square 0.1 Å $< d_+ < 20$ Å and 0.1 Å $< d_- < 20$ Å into the $[\nu_1(d_+, d_-), \nu_{3/2}(d_+, d_-)]$ plane (the dark region in Fig. 6.7b), i.e., the region where the system Eq. (6.59) has solutions between 0.1 and 20 Å for both ionic diameters. The points shown are the results from the asymptotic lines in Fig. 6.7a. The point corresponding to the ν_1 and $\nu_{3/2}$ given by the full line falls out of the dark region, contrary to what happens to the point that follows from the dashed line. That is, according to the full line, d_+ and d_- lie outside the interval $[0.1, 20]$ Å (which is not reasonable), while the dashed line leads to $d_+ = 3.8$ Å and $d_- = 5.4$ Å. In other words, the asymptotic extrapolation of the experimental data is very sensitive to small errors. To obtain the two ionic diameters with a reasonable degree of confidence as independent parameters, one needs more data at very low densities (which to the best of our knowledge is not available in the literature) so that the asymptotic fit can be done. We have shown the case of NaCl, but the situation is identical for other salts.

6.4 Conclusions

With the help of field theoretic methods we have obtained the exact low density ("virial") expansion of the TCPHC up to order $5/2$ in density. In its general form, the model can be applied to both electrolyte solutions and dilute colloidal suspensions (when the van der Waals forces are unimportant); the free energy derived here provides an unified way for handling both systems in the limit of low concentration. As the calculations above have shown, the generalization to short-range potentials other than the hard core is possible, although one might be unable to write down the final results in a closed form.

The behavior of the coefficients B_2 and $B_{5/2}$ suggests that the series is in fact a non-converging one, meaning that the inclusion of higher order terms is not sure to extended the validity of the free energy to larger densities. We have seen that the divergent behavior of these coefficients is related to the ionic pairing[13, 32, 119] which is favored as the coupling increases (this is not present e.g. in the OCPHC[82]). Also, the use of this expansion is not very good to study phase behavior[75] of ionic systems: in the situation of a phase-separated system with a very dilute phase in coexistence with a denser phase, it is possible that the average density in the denser phase already falls outside the scope of the low density expansion up to the calculated order.

In applying our results to colloidal systems we have concluded that at low density the counterion entropic contribution dominates over the electrostatic contribution due to the macroions; the latter contribution can be described, in this limit and up to this order, by an OCPHC corrected to exclude the background from the particles.

Finally we used the theoretical results for the mean activity coefficient in order to fit experimental data and extract effective ionic sizes. In the simplest fitting, where we assumed the two ionic diameters to be equal, we obtained sizes that are reasonable and close to what one would expect from the results obtained by other methods. For the more interesting case where the two ionic sizes are taken as free parameters and determined independently, we have shown that one would need more experimental data on the mean activity coefficient at very low densities (which, to the best of our knowledge, is not available in the literature) to get the correct values for the diameters. With the proper experimental data it would then be a simple matter to get the ionic sizes.

Chapter 7

Conclusions and outlook

We are now in a position to make a very brief summary of the results obtained here.

In Chapter 2 we have simulated the simple double layer (charged wall in the presence of its counterions) and compared it with analytical results, both at low and high coupling. The novel strong coupling theory[80] was confirmed to yield the correct asymptotic counterion distribution when the coupling parameter Ξ goes to infinity; this complements the classical Poisson-Boltzmann results, which is asymptotically correct as $\Xi \to 0$. We gave a detailed account of the methods employed in the computer simulations.

In Chapters 3 and 4 we have looked at two factors that modify (and complicate) the double layer problem, respectively the presence of a dielectric jump and the discretization of the charges on the wall. Both modifications can have a dramatic impact on the counterion distribution, as we have seen, especially in systems with high coupling.

In Chapter 5 we looked at the interaction between two simple double layers. We have also obtained the celebrated attraction between similarly charged plates. However, as we have demonstrated, for most systems the equilibrium distance in the bound state is below 3 (in units of Gouy-Chapman length), which is usually smaller than the projected (lateral) distance between counterions; the density profile in such case is well described by the strong coupling theory, as showed by the computer simulations. The small $\widetilde{d}$ (distance between the walls in units of Gouy-Chapman length) behavior is also well described by the strong coupling theory, even for systems that at intermediate $\widetilde{d}$ are far from the SC predictions.

Finally in Chapter 6, we have applied field-theoretic tools to derive the low-density expansion of the asymmetric two-component plasma. We have shown, for instance, that in the colloidal limit (very large charge and size asymmetry between macroions and counterions) the free energy is dominated by the entropy of the counterions; the electrostatic contribution to the free energy was proved, up to second order in density, to map into the one-component plasma. A way of determining the "thermodynamic radii" of ions in solution from experimental data for the mean activity coefficient was shown. This is expected to lead to accurate results if more data at low densities (below 0.005 mole per liter) is available.

There are still many open questions which have not been addressed here but that interesting and should be looked at in the future. Some examples are:

Making the double layer more realistic

The double layer as treated here is highly idealized. Real systems are much more complicated, and one should try to bring the modeled systems closer to reality: for instance, discretize the charges at the wall but given them a shape, e.g. instead of putting a hard wall at $\widetilde{z} = 0$ as we did in Chapter 4, one could put each of the charges at the wall inside a half-sphere or a cylinder. Another possibility is to allow the charges at the wall to move in the plane. Mixing up the dielectric jump with the discretization effects, as well as looking at packing effects due to finite size of the counterions are also of experimental interest.

Exchange of ions between the wall and the bulk

In many real systems, the charge on the surface is regulated by the pH of the solution. One should also look at this possibility in the simulations, maybe by assigning a chemical potential to the ions at the wall instead of keeping their number fixed. Also the simultaneous presence of positively and negatively charged species at the wall should lead to interesting effects.

Making the wall "flexible"

Another natural step from this work would be to look at fluid membranes that are charged, or globally neutral but with charged groups. This is a step toward biological systems, and could bring some answers, for instance, to the problem of electroporation (formation of pores in membranes due to the application of external electric fields).

Appendix A

The Lekner summation

We show here a quick derivation of the Lekner summation formula for the electrostatic energy Eq. (2.35), based on the original derivation by Lekner[63]. Our starting point the is the sum

$$v_L(\mathbf{r},\mathbf{r}') = v_L(0) + \sum_{l,m=-\infty}^{+\infty} \frac{1}{\sqrt{[\xi+l]^2+[\eta+m]^2+\zeta^2}} - \sum_{l,m=-\infty}^{+\infty} \frac{1}{\sqrt{[\alpha_1+l]^2+[\alpha_2+m]^2+\alpha_3^2}}, \quad \text{(A.1)}$$

where $v_L(0)$ is the energy of the reference state given by $\xi=\alpha_1$, $\eta=\alpha_2$ and $\zeta=\alpha_3$. Although $v_L(0)$ is divergent, the difference between the two infinite sums in the rhs is well defined, as we will show. To obtain a fast convergent form for the sums, we first apply the Euler transformation (valid for $\nu>0$)

$$\frac{1}{x^\nu} = \frac{1}{\Gamma(\nu)} \int_0^\infty \mathrm{d}t\, t^{\nu-1} \mathrm{e}^{-xt} \quad \text{(A.2)}$$

followed by the Poisson-Jacobi identity

$$\sum_{m=-\infty}^{+\infty} \mathrm{e}^{-[u+m]^2 t} = \sqrt{\frac{\pi}{t}} \sum_{m=-\infty}^{+\infty} \mathrm{e}^{-\pi^2 m^2/t} \cos(2\pi m u) \quad \text{(A.3)}$$

to the infinite sums in Eq. (A.1). After these transformations, v_L looks like

$$v_L(\mathbf{r},\mathbf{r}') = v_L(0) + \sum_{l,m=-\infty}^{+\infty} \left\{ \int_0^\infty \mathrm{d}t \frac{1}{t} \mathrm{e}^{-t\varrho^2-\pi^2 l^2/t} \cos(2\pi l\xi) - \int_0^\infty \mathrm{d}t \frac{1}{t} \mathrm{e}^{-t\bar{\varrho}^2-\pi^2 l^2/t} \cos(2\pi l\alpha_1) \right\} \quad \text{(A.4)}$$

where $\varrho^2=[\eta+m]^2+\zeta^2$ and $\bar{\varrho}^2=[\alpha_2+m]^2+\alpha_3^2$. We now separate the terms with $l=0$ from the sums above and use the integral representation of the modified Bessel function of second kind, viz.

$$\int_0^\infty \mathrm{d}t\, t^{\nu-1} \mathrm{e}^{-p^2 t-\pi^2 m^2/t} = 2\left[\pi\frac{|m|}{|p|}\right]^\nu K_\nu\big(2\pi|mp|\big), \quad \text{(A.5)}$$

to rewrite v_L as

$$v_L(\mathbf{r},\mathbf{r}') = v_L(0) + \sum_{m=-\infty}^{+\infty}\int_0^\infty \mathrm{d}t\frac{1}{t}\left[\mathrm{e}^{-t\varrho^2} - \mathrm{e}^{-t\bar{\varrho}^2}\right] + 4\sum_{l=1}^{\infty}\cos(2\pi l\xi)\sum_{m=-\infty}^{+\infty}K_0(2\pi l\varrho) - 4\sum_{l=1}^{\infty}\cos(2\pi l\alpha_1)\sum_{m=-\infty}^{+\infty}K_0(2\pi l\bar{\varrho}). \quad \text{(A.6)}$$

The term corresponding to $l = 0$ (the second term in the rhs) leads to

$$\sum_{m=-\infty}^{+\infty}\int_0^\infty \mathrm{d}t\frac{1}{t}\left[\mathrm{e}^{-t\varrho^2} - \mathrm{e}^{-t\bar{\varrho}^2}\right] = -\sum_{m=-\infty}^{+\infty}\ln(\varrho^2/\bar{\varrho^2}) = -\ln\left(\frac{\cosh(2\pi\zeta)-\cos(2\pi\eta)}{\cosh(2\pi\alpha_3)-\cos(2\pi\alpha_2)}\right). \quad \text{(A.7)}$$

With this, we finally arrive to Lekner's summation formula for the electrostatic energy, which reads

$$v_L(\mathbf{r},\mathbf{r}') = v_L(0) + C - \ln\Big(\cosh(2\pi\zeta)-\cos(2\pi\eta)\Big) + s(\xi,\eta,\zeta) \quad \text{(A.8)}$$

where s is the series

$$s(\xi,\eta,\zeta) = 4\sum_{l=1}^{\infty}\cos(2\pi l\xi)\sum_{m=-\infty}^{+\infty}K_0\left(2\pi l\sqrt{[\eta+m]^2+\zeta^2}\right) \quad \text{(A.9)}$$

and C is a constant that depends on the reference state, given by

$$C = \ln\Big(\cosh(2\pi\alpha_3) - cos(2\pi\alpha_1)\Big) - s(\alpha_1,\alpha_2,\alpha_3). \quad \text{(A.10)}$$

Appendix B

The strong coupling regime

We derive in this Appendix the lowest order term of the counterion density profile at the strong coupling regime[80]. We start with the partition function for N counterions in the presence of a fixed charge distribution $\sigma(\mathbf{r})$, which reads

$$\mathcal{Z} = \frac{1}{N!}\int \prod_{j=1}^{N} \mathrm{d}\mathbf{r}_j \exp\left(-\frac{1}{2}\int \mathrm{d}\mathbf{r}\,\mathrm{d}\mathbf{r}'\left[\hat{\rho}_c(\mathbf{r})+\sigma(\mathbf{r})\right] v_c(\mathbf{r},\mathbf{r}')\left[\hat{\rho}_c(\mathbf{r}')+\sigma(\mathbf{r}')\right]\right) \tag{B.1}$$

where

$$\hat{\rho}_c(\mathbf{r}) = q\sum_{j=1}^{N}\delta(\mathbf{r}-\mathbf{r}_j), \tag{B.2}$$

$\delta(\mathbf{r})$ is the Dirac delta-function, q is the valence of the counterions and v_c is the Coulomb potential given by the solution of the equation

$$-\frac{k_B T}{e^2}\nabla\cdot\left[\varepsilon(\mathbf{r})\nabla v_c(\mathbf{r},\mathbf{r}')\right] = \delta(\mathbf{r}-\mathbf{r}'), \tag{B.3}$$

which is nothing but the Poisson law. The equation above is given in its most general form, with a space-varying dielectric constant $\varepsilon(\mathbf{r})$ and a potential that is not assumed to depend only on the distance between the charge that generates the field at $\mathbf{r}$ and the test point at $\mathbf{r}'$.

To make this partition function more manageable, we apply a Hubbard-Stratonovich and a Legendre transformation, obtaining the grand-partition function of the system in a field-theoretic form (see also Chapter 6). After this, the grand-partition function looks like

$$\mathcal{Q} = \int \frac{\mathcal{D}\phi}{\mathcal{Z}_v}\exp\left(-\int \mathrm{d}\mathbf{r}\mathrm{d}\mathbf{r}'\phi(\mathbf{r})v^{-1}(\mathbf{r},\mathbf{r}')\phi(\mathbf{r}') - \imath\int \mathrm{d}\mathbf{r}\frac{\sigma(\mathbf{r})}{q}\phi(\mathbf{r}) + \lambda\int_V \mathrm{d}\mathbf{r}\mathrm{e}^{-\imath\phi(\mathbf{r})}\right) \tag{B.4}$$

where λ is the fugacity (exponential of the chemical potential) of the counterions and the integral $\int_V$ spans the volume where the counterions are. We have rescaled the field such that $\phi \to q\phi$ and used the definition $v^{-1}(\mathbf{r},\mathbf{r}') \equiv v_c^{-1}(\mathbf{r},\mathbf{r}')/q^2$, where the inverse Coulomb potential, v_c^{-1}, is related to v_c through

$$\int \mathrm{d}\mathbf{r}'' v_c^{-1}(\mathbf{r}-\mathbf{r}'')\, v_c(\mathbf{r}''-\mathbf{r}') = \delta(\mathbf{r}-\mathbf{r}'). \tag{B.5}$$

Using the latter equation and Poisson's law given in Eq. (B.3), it turns out that

$$v_c^{-1}(\mathbf{r},\mathbf{r}') = -\frac{k_B T}{e^2}\nabla\cdot\big[\varepsilon(\mathbf{r})\nabla\delta(\mathbf{r}-\mathbf{r}')\big]. \tag{B.6}$$

With the help of a generating field, it has been shown in Chapter 2 that the average local density of counterions is given by

$$\rho(\mathbf{r}) = \lambda\langle \mathrm{e}^{-\imath\phi(\mathbf{r})}\rangle. \tag{B.7}$$

It follows from electroneutrality the normalization condition

$$N = \int_V \mathrm{d}\mathbf{r}\rho(\mathbf{r}) \tag{B.8}$$

or, using Eq. (B.7) and assuming lateral symmetry,

$$\Lambda\int \mathrm{d}\tilde{z}\,\langle \mathrm{e}^{-\imath\bar{\phi}(\tilde{z})}\rangle = 1, \tag{B.9}$$

where $\Lambda = \lambda/2\pi\ell_B\sigma_s^2$ and $\widetilde{z} = z/\mu$; the integration over $\widetilde{z}$ is carried out at the volume where the counterions are. The normalization condition can be solved by an expansion of the fugacity as $\Lambda = \Lambda_0 + \Lambda_1/\Xi + \cdots$, and after a Legendre transformation, the density profile is obtained in the canonical ensemble as an expansion where $1/\Xi$ is the small parameter[80]. In the following we will only look at the lowest order term of the expansion, and so the normalization condition can be, in general, easily solved. Using Eq. (B.7), the density at lowest order then reads

$$\rho(\mathbf{r}) = \lambda\frac{\int\mathcal{D}\phi\ \mathrm{e}^{\bar{\mathcal{H}}}}{\int\mathcal{D}\phi\ \mathrm{e}^{\bar{\mathcal{H}}_2}} \tag{B.10}$$

where

$$\bar{\mathcal{H}} = -\frac{1}{2}\int \mathrm{d}\mathbf{r}'\mathrm{d}\mathbf{r}''\phi(\mathbf{r}')v^{-1}(\mathbf{r}',\mathbf{r}'')\phi(\mathbf{r}') - \imath\int\mathrm{d}\mathbf{r}'\phi(\mathbf{r}')\big[\frac{\sigma(\mathbf{r}')}{q}+\delta(\mathbf{r}'-\mathbf{r})\big] \tag{B.11}$$

and

$$\bar{\mathcal{H}}_2 = -\frac{1}{2}\int \mathrm{d}\mathbf{r}'\mathrm{d}\mathbf{r}''\phi(\mathbf{r}')v^{-1}(\mathbf{r}',\mathbf{r}'')\phi(\mathbf{r}'') - \imath\int\mathrm{d}\mathbf{r}'\phi(\mathbf{r}')\frac{\sigma(\mathbf{r}')}{q}. \tag{B.12}$$

Notice that in the fugacity disappeared from $\mathcal{H}$ and $\mathcal{H}_2$. After completing the quadratic terms in $\mathcal{H}$ and $\mathcal{H}_2$, it follows from Eq. (B.10) that

$$\frac{\rho(\mathbf{r})}{2\pi\ell_B\sigma_s^2} = \Lambda\exp\bigg(-\frac{q^2}{2}v_c(\mathbf{r},\mathbf{r}) - q\int\mathrm{d}\mathbf{r}'\sigma(\mathbf{r}')v_c(\mathbf{r}',\mathbf{r})\bigg), \tag{B.13}$$

where we already rescaled the density by the factor $2\pi\ell_B\sigma_s^2$. This is the lowest order result for the density profile of counterions at the strong coupling regime[80]. The expression for the simplest double layer has been derived in Chapter 2. We now particularize to the cases treated in Chapter 3 and 5.

B.1 One charged plane with dielectric jump

The Coulomb potential is given by (cf. Chapter 3)

$$v_c(\mathbf{r},\mathbf{r}') = \ell_B\left[\frac{1}{|\mathbf{r}-\mathbf{r}'|} + \frac{\Delta}{\sqrt{[\mathbf{r}-\mathbf{r}']^2 + 4zz'}}\right] \tag{B.14}$$

for $z, z' > 0$. Notice that here $\ell_B = e^2/4\pi\varepsilon_> k_B T$, where $\varepsilon_>$ is the dielectric constant of the half-space where the counterions are immersed, and $\sigma(\mathbf{r}) = -\sigma_s\delta(z)$. Note that now

$$v_c(\mathbf{r},\mathbf{r}) = v_c(0) + \frac{\ell_B\Delta}{2z}. \tag{B.15}$$

At lowest order, one gets from the normalization condition Eq.(B.9) that for $\Delta > 0$

$$\Lambda_0 = \sqrt{\frac{1+\Delta}{\Xi\Delta}}\frac{1}{K_1\big(\sqrt{\Xi\Delta[1+\Delta]}\big)}\exp\left(\frac{\Xi}{2}v_c(0) - \frac{1}{2\pi}\int \mathrm{d}\widetilde{\mathbf{r}}'\delta(z')\frac{1+\Delta}{\widetilde{r}'}\right), \tag{B.16}$$

with all lengths (also in the self-energy) rescaled by μ, from which follows that

$$\frac{\rho(\widetilde{\mathbf{r}})}{2\pi\ell_B\sigma_s^2} = \sqrt{\frac{1+\Delta}{\Xi\Delta}}\frac{1}{K_1\big(\sqrt{\Xi\Delta[1+\Delta]}\big)}\exp\left(-[1+\Delta]\widetilde{z} - \frac{\Xi\Delta}{4\widetilde{z}}\right), \tag{B.17}$$

where $K_1(x)$ is the first order modified Bessel function of second kind[2]. In the limit $x \to 0$, $K_1(x) \simeq 1/x$, i.e., in the limit $\Delta \to 0$ this expression reduces to the pure exponential decay derived in Chapter 2, as expected.

If $\Delta < 0$, the normalization condition leads to a prefactor in Λ_0 that can have positive or negative values, depending on Ξ and Δ. This is a clear sign of inconsistency, which can be easily understood: the presence of the dielectric jump at the wall leads to an attractive potential that diverges as $1/z$ at $z = 0$, with the consequent divergent behavior of the density at the wall. The only way to avoid this is to put the dielectric jump behind the hard wall, or to put the charges inside hard spheres, so that the counterions never touch their (oppositely charged) images.

B.2 Two charged walls

In this case, the Coulomb potential is the simple $v_c(\mathbf{r},\mathbf{r}') = \ell_B/|\mathbf{r}-\mathbf{r}'|$, and $\sigma(\mathbf{r}) = -\sigma_s\big[\delta(z + d/2) + \delta(z - d/2)\big]$. Again at lowest order, one obtains from the normalization condition Eq.(B.9) that

$$\Lambda_0 = \exp\left(\frac{\Xi}{2}v_c(0) - \frac{1}{2\pi}\int \mathrm{d}\widetilde{\mathbf{r}}'\big[\delta(\widetilde{z}' + \widetilde{d}/2) + \delta(\widetilde{z}' - \widetilde{d}/2)\big]\frac{1}{\widetilde{r}'}\right), \tag{B.18}$$

and it follows that

$$\frac{\rho(\widetilde{z})}{2\pi\ell_B\sigma_s^2} = \frac{2}{\widetilde{d}}, \tag{B.19}$$

where $\widetilde{d} = d/\mu$, as usual.

Appendix C

The contact value theorem

We start with the grand-canonical partition function of a system of moving and fixed charges (the latter given by the charge distribution $\sigma(\mathbf{r})$),

$$\mathcal{Q} = \int \frac{\mathcal{D}\phi}{\mathcal{Z}_v} \exp\left(- \int \mathrm{d}\mathbf{r}\mathrm{d}\mathbf{r}' \phi(\mathbf{r}) v^{-1}(\mathbf{r},\mathbf{r}') \phi(\mathbf{r}') - \imath \int \mathrm{d}\mathbf{r} \frac{\sigma(\mathbf{r})}{q} \phi(\mathbf{r}) + \lambda \int_V \mathrm{d}\mathbf{r} \mathrm{e}^{-\imath\phi(\mathbf{r})} \right) \quad \text{(C.1)}$$

(cf. Eq. (B.4)). As in Appendix B, $v^{-1} = v_c^{-1}/q^2$, with v_c^{-1} given by Eq. (B.6). The $\int_V$ corresponds to the integration over the volume where the counterions are.

We are here interested in two cases: (i) one charged plane is in the presence of its counterions and (ii) two equally charged wall confining their counterions between them. The dielectric constant is assumed to be the same everywhere, i.e., $v(\mathbf{r},\mathbf{r}') = v(\mathbf{r}-\mathbf{r}')$. In the first case the pressure at equilibrium is zero, and we will get the exact value of the density of counterions at contact, while in the second case we will be interested in the pressure itself (we use this result in Chapter 5).

The pressure acting on the wall(s) is given by

$$P = \frac{1}{A} \frac{\partial \ln \mathcal{Q}}{\partial L_z} \quad \text{(C.2)}$$

where the pressure P is in units of $k_B T$, and A is the lateral area (which is infinite in the thermodynamic limit). It is implicitly assumed that when one wall is present, it is fixed to $z = L_z$, while when two wall are present, one is at $z = 0$ and the other[1] at $z = L_z$. $\mathcal{Q}$ depends on L_z through the fixed density profile $\sigma(\mathbf{r})$, which reads

$$\sigma(\mathbf{r}) = -\frac{\sigma_s}{q} \delta(z - L_z) \quad \text{(C.3)}$$

for one wall and

$$\sigma(\mathbf{r}) = -\frac{\sigma_s}{q} [\delta(z) + \delta(z - L_z)] \quad \text{(C.4)}$$

for two walls, and through the volume V where the ions are confined, in the first case $]-\infty, L_z]$ (notice that here the ions are assumed to be confined to the left half-space, contrary to previous

[1] In Chapter 5 we put the walls at $z = -d/2$ and $z = d/2$. We use a different notation in this appendix, without loss of generality, since it is more convenient for the derivation that follows.

Chapters but without loss of generality) and in the second case $[0, L_z]$. By completing the squares in the action in Eq. (C.1), we can rewrite $\mathcal{Q}$ as

$$\mathcal{Q} = \exp\left(-\frac{1}{2q^2}\int \mathrm{d}\mathbf{r}\mathrm{d}\mathbf{r}'\sigma(\mathbf{r})v(\mathbf{r},\mathbf{r}')\sigma(\mathbf{r}')\right)\int \frac{\mathcal{D}\Phi}{\mathcal{Z}_v}\mathrm{e}^{\bar{\mathcal{H}}} \tag{C.5}$$

where the action reads

$$\bar{\mathcal{H}} = -\int \mathrm{d}\mathbf{r}\mathrm{d}\mathbf{r}'\Phi(\mathbf{r})v^{-1}(\mathbf{r},\mathbf{r}')\Phi(\mathbf{r}') + \lambda\int_V \mathrm{d}\mathbf{r}\mathrm{e}^{-\imath\Phi(\mathbf{r})-\int \mathrm{d}\mathbf{r}'v(\mathbf{r},\mathbf{r}')\sigma(\mathbf{r}')/q} \tag{C.6}$$

and $\Phi(\mathbf{r}) = \phi(\mathbf{r}) + \imath\int \mathrm{d}\mathbf{r}'v(\mathbf{r},\mathbf{r}')\sigma(\mathbf{r}')/q$. We use Eq. (C.5) to calculate the pressure, which then reads

$$P = \frac{1}{A}\left\langle\frac{\partial\bar{\mathcal{H}}}{\partial L_z}\right\rangle - \frac{1}{2q^2A}\frac{\partial}{\partial L_z}\left[\int \mathrm{d}\mathbf{r}\mathrm{d}\mathbf{r}'\,\sigma(\mathbf{r})v(\mathbf{r},\mathbf{r}')\sigma(\mathbf{r}')\right]. \tag{C.7}$$

The derivative of $\mathcal{H}$ has to be done with some care, with special attention to the fact that the confining volume V where the counterions are also depends explicitly on L_z; with this in mind, we obtain

$$\begin{aligned}\frac{\partial\bar{\mathcal{H}}}{\partial L_z} = \lambda\int \mathrm{d}\mathbf{r}\,\delta(z-L_z)\,\mathrm{e}^{-\imath\Phi(\mathbf{r})-\int \mathrm{d}\mathbf{r}'v(\mathbf{r},\mathbf{r}')\sigma(\mathbf{r}')/q} \\ - \lambda\int_V \mathrm{d}\mathbf{r}\,\mathrm{e}^{-\imath\Phi(\mathbf{r})-\int \mathrm{d}\mathbf{r}'v(\mathbf{r},\mathbf{r}')\sigma(\mathbf{r}')/q}\frac{\partial}{\partial L_z}\left[\int \mathrm{d}\mathbf{r}'\,v(\mathbf{r},\mathbf{r}')\frac{\sigma(\mathbf{r}')}{q}\right].\end{aligned} \tag{C.8}$$

If we use $\rho(\mathbf{r}) = \lambda\langle\mathrm{e}^{\imath\phi(\mathbf{r})}\rangle$, and the fact that the density profile has lateral symmetry, we finally obtain the pressure as

$$\begin{aligned}P = \rho(L_z) - \frac{1}{qA}\int_V \mathrm{d}\mathbf{r}\,\rho(\mathbf{r})\frac{\partial}{\partial L_z}\left[\int \mathrm{d}\mathbf{r}'\,v(\mathbf{r},\mathbf{r}')\sigma(\mathbf{r})\right] \\ - \frac{1}{2q^2A}\frac{\partial}{\partial L_z}\left[\int \mathrm{d}\mathbf{r}\mathrm{d}\mathbf{r}'\,\sigma(\mathbf{r})v(\mathbf{r},\mathbf{r}')\sigma(\mathbf{r}')\right]\end{aligned} \tag{C.9}$$

which is the contact value theorem in its general form. We can now particularize it to the two cases of interest.

C.1 One wall

In this case, $\sigma(\mathbf{r}) = -\sigma_s\delta(z-L_z)/q$ and $v(\mathbf{r},\mathbf{r}') = q^2\ell_B/|\mathbf{r}-\mathbf{r}'|$. It follows that

$$-\frac{1}{2q^2A}\frac{\partial}{\partial L_z}\left[\int \mathrm{d}\mathbf{r}\mathrm{d}\mathbf{r}'\,\sigma(\mathbf{r})v(\mathbf{r},\mathbf{r}')\sigma(\mathbf{r}')\right] = 0 \tag{C.10}$$

and

$$-\frac{1}{qA}\int_V \mathrm{d}\mathbf{r}\,\rho(\mathbf{r})\frac{\partial}{\partial L_z}\left[\int \mathrm{d}\mathbf{r}'\,v(\mathbf{r},\mathbf{r}')\sigma(\mathbf{r})\right] = -2\pi\ell_B\sigma_s^2. \tag{C.11}$$

In the latter, we used the fact that the density profile has xy symmetry and

$$\int_V \mathrm{d}\mathbf{r}\, \rho(\mathbf{r}) = N = A\, \frac{\sigma_s}{q}. \tag{C.12}$$

Since the pressure is zero when the system is in equilibrium, we arrive at the final result

$$\frac{\rho(L_z)}{2\pi\ell_B\sigma_s^2} = 1. \tag{C.13}$$

C.2 Two walls

Now $\sigma(\mathbf{r}) = -\sigma_s[\delta(z) + \delta(z - L_z)]/q$, and it follows that

$$-\frac{1}{2q^2A}\frac{\partial}{\partial L_z}\left[\int \mathrm{d}\mathbf{r}\mathrm{d}\mathbf{r}'\, \sigma(\mathbf{r})v(\mathbf{r},\mathbf{r}')\sigma(\mathbf{r}')\right] = 2\pi\ell_B\sigma_s^2 \tag{C.14}$$

and

$$-\frac{1}{qA}\int_V \mathrm{d}\mathbf{r}\, \rho(\mathbf{r})\frac{\partial}{\partial L_z}\left[\int \mathrm{d}\mathbf{r}'\, v(\mathbf{r},\mathbf{r}')\sigma(\mathbf{r})\right] = -4\pi\ell_B\sigma_s^2. \tag{C.15}$$

Notice that we used $\sigma_s = qN/2A$ in the latter integral. It finally follows that

$$\frac{P}{2\pi\ell_B\sigma_s^2} = -1 + \frac{\rho(L_z)}{2\pi\ell_B\sigma_s^2}, \tag{C.16}$$

which relates the pressure felt by the walls and the contact value of the counterion density distribution. Notice that if $P = 0$ (for instance when $L_z \to \infty$), this expression reduces to Eq. (C.13), as expected.

Appendix D

Some expressions used in the low density expansion

D.1 Averages needed for Z_1 and Z_2

The following expressions were used to obtain Eqs. (6.25–6.26). In order to have more compact formulas we use the Greek letters α and β instead of $+$ or $-$. For instance, $\alpha\, q_\alpha$ means both $+q_+$ and $-q_-$.

$$\big\langle h_\alpha(\mathbf{r})\big\rangle = \mathrm{e}^{q_\alpha^2 v_{\mathrm{c}}(0)/2}, \tag{D.1}$$

$$\big\langle \mathrm{e}^{-\imath\alpha q_\alpha \phi(\mathbf{r})}\big\rangle = \mathrm{e}^{-q_\alpha^2 v_{\mathrm{DH}}(0)/2}, \tag{D.2}$$

$$\big\langle h_\alpha(\mathbf{r}) h_\beta(\mathbf{r}')\big\rangle = \mathrm{e}^{-\omega_{\alpha\beta}(\mathbf{r}-\mathbf{r}')+\left[q_\alpha^2 v_{\mathrm{c}}(0)+q_\beta^2 v_{\mathrm{c}}(0)\right]/2}, \tag{D.3}$$

$$\big\langle \mathrm{e}^{-\imath\alpha\, q_\alpha\phi(\mathbf{r})-\imath\beta\, q_\beta\phi(\mathbf{r}')}\big\rangle = \mathrm{e}^{-\left[q_\alpha^2 v_{\mathrm{DH}}(0)+q_\beta^2 v_{\mathrm{DH}}(0)\right]/2}\mathrm{e}^{-\alpha\beta\, q_\alpha q_\beta v_{\mathrm{DH}}(\mathbf{r}-\mathbf{r}')}, \tag{D.4}$$

$$\big\langle \phi^2(\mathbf{r}')\mathrm{e}^{-\imath\alpha\, q_\alpha\phi(\mathbf{r})}\big\rangle = \mathrm{e}^{-q_\alpha^2 v_{\mathrm{DH}}(0)/2}\Big[v_{\mathrm{DH}}(0) - q_\alpha^2 v_{\mathrm{DH}}^2(\mathbf{r}-\mathbf{r}')\Big]. \tag{D.5}$$

We remind that $\langle\cdots\rangle$ are averages where ω^{-1} and v_{DH}^{-1} are the propagators.

D.2 The coefficients in the grand-canonical free energy

We give here the explicit expressions for the coefficients in g, Eq. (6.29). It is useful to define the function

$$H(x) = \frac{11}{6} - 2\gamma + \frac{1}{x^3}\mathrm{e}^{-x}\left[2 - x + x^2\right] - \Gamma(0,x) - \ln x, \tag{D.6}$$

where γ is Euler's constant and $\Gamma(a,b)$ is the incomplete Gamma-function[2]. The coefficients then read

$$m_1 = \frac{\pi}{3}\frac{q_+^6\ell_B^3}{d_+^3}\Big\{-H\Big(\frac{q_+^2\ell_B}{d_+}\Big)+\ln\Big(\frac{3d_+}{\ell_B}\Big)\Big\}, \tag{D.7}$$

$$m_2 = \frac{\pi}{3}\frac{q_-^6\ell_B^3}{d_+^3}\Big\{-H\Big(\frac{q_-^2\ell_B}{d_-}\Big)+\ln\Big(\frac{3d_-}{\ell_B}\Big)\Big\}, \tag{D.8}$$

$$m_3 = \frac{2\pi}{3}\frac{q_+^3q_-^3\ell_B^3}{d_+^3}\Big\{H\Big(\frac{2q_+q_-\ell_B}{d_++d_-}\Big)-\ln\Big(\frac{3[d_++d_-]}{2\ell_B}\Big)\Big\}, \tag{D.9}$$

$$n_1 = \frac{\pi}{3}\frac{q_+^8\ell_B^3}{d_+^3}\Big\{-\frac{5}{8}-2H\Big(\frac{q_+^2\ell_B}{d_+}\Big)+\ln\Big(\frac{12d_+^2}{\ell_B^2}\Big)\Big\}, \tag{D.10}$$

$$n_2 = \frac{\pi}{3}\frac{q_-^8\ell_B^3}{d_+^3}\Big\{-\frac{5}{8}-2H\Big(\frac{q_-^2\ell_B}{d_-}\Big)+\ln\Big(\frac{12d_-^2}{\ell_B^2}\Big)\Big\}, \tag{D.11}$$

$$\begin{aligned} n_3 =& \frac{2\pi}{3}\frac{q_+^3q_-^3\ell_B^3}{d_+^3}\Big\{-\frac{5}{8}q_+q_-+\frac{[q_+-q_-]^2}{2}H\Big(-\frac{2q_+q_-\ell_B}{d_++d_-}\Big)\\ &+q_+q_-\ln\Big(\frac{2[d_++d_-]}{\ell_B}\Big)-\frac{q_+^2+q_-^2}{2}\ln\Big(\frac{3[d_++d_-]}{2\ell_B}\Big)\Big\}, \end{aligned} \tag{D.12}$$

$$p_1 = \frac{\pi}{3}\frac{q_+^6\ell_B^3}{d_+^3}, \qquad p_2 = \frac{\pi}{3}\frac{q_-^6\ell_B^3}{d_+^3}, \qquad p_3 = -\frac{2\pi}{3}\frac{q_+^3q_-^3\ell_B^3}{d_+^3}, \tag{D.13}$$

$$r_1 = \frac{2\pi}{3}\frac{q_+^8\ell_B^3}{d_+^3}, \qquad r_2 = \frac{2\pi}{3}\frac{q_-^8\ell_B^3}{d_+^3}, \tag{D.14}$$

$$r_3 = \frac{2\pi}{3}\frac{q_+^3q_-^3\ell_B^3}{d_+^3}\Big[q_+q_--\frac{q_+^2+q_-^2}{2}\Big], \tag{D.15}$$

$$s_1 = \frac{q_+^4}{8}, \quad s_2 = \frac{q_-^4}{8}, \quad t_0 = \frac{d_+^3}{12\pi\ell_B^3}, \quad t_1 = \frac{q_+^6}{48}, \quad t_2 = \frac{q_-^6}{48}. \tag{D.16}$$

D.3 The coefficients in $\widetilde{\lambda}_-$

In Eq. (6.33) we have established the dependence of $\widetilde{\lambda}_-$ as a power expansion of $\widetilde{\lambda}_+$. The coefficients a_0, a_1, etc. must be such that the system is globally neutral. These are given by

$$a_0 = \frac{q_+}{q_-}, \tag{D.17}$$

$$a_1 = \frac{q_+^2}{q_-}\big[q_+^2-q_-^2\big]\sqrt{\frac{\pi\ell_B^3}{d_+^3}\Big[1+\frac{q_-}{q_+}\Big]}, \tag{D.18}$$

$$a_2 = \frac{q_+}{q_-^2}\big[-2m_2q_+ + 2m_1q_- + m_3[q_1 - q_2]\big] + \frac{\pi}{6}\frac{q_+^2\ell_B^3}{q_-d_+^3}\big[q_+ + q_-\big]^2 \times \big[7q_+^3 - 9q_+^2q_- + 2q_-^3\big] + \frac{\pi}{3}\frac{q_+^2\ell_B^3}{q_-d_+^3}\big[q_+^5 - q_+^3q_-^2 + q_+^2q_-^3 - q_-^5\big] \times \ln\Big(\frac{4\pi\ell_B^3}{d_+^3}q_+\big[q_+ + q_-\big]\Big), \quad \text{(D.19)}$$

$$a_3 = \frac{\pi}{3}\frac{q_+^2\ell_B^3}{q_-d_+^3}\big[q_+^5 - q_+^3q_-^2 + q_+^2q_-^3 - q_-^5\big], \quad \text{(D.20)}$$

$$a_4 = \frac{\ell_B^{3/2}}{24q_-^3}\sqrt{\pi q_+\big(q_+ + q_-\big)}\Big\{24n_1\big[5q_+q_-^2 - q_-^3\big] + 24n_2\big[q_+^3 - 5q_+q_-^2\big] + 72n_3\big[q_+^2q_- - q_+q_-^2\big] + 24m_1\big[q_+^2q_-^3 - 3q_+q_-^4\big] + 24m_2\big[-4q_+^4q_- - q_+^3q_-^2 + 7q_+^2q_-^3\big] + 12m_3\big[2q_+^4q_- - q_+^3q_-^2 - 6q_+^2q_-^3 + 5q_+q_-^4\big] + \frac{\pi\ell_B^3}{d_+^3}q_+^2q_-^2[q_+ + q_-]^2\big[26q_+^5 - 34q_+^4q_- - 31q_+^3q_-^2 + 67q_+^2q_-^3 - 45q_+q_-^4 + 17q_-^5\big]\Big\} + \frac{\pi^{3/2}}{6}\frac{q_+^{5/2}\ell_B^{9/2}}{q_-d_+^{9/2}}\big[q_+ - q_-\big]\big[q_+ + q_-\big]^{5/2} \times \big[10q_+^4 - 11q_+^3q_- + 13q_+^2q_-^2 - 4q_+q_-^3 + 3q_-^4\big] \times \ln\Big(\frac{4\pi\ell_B^3}{d_+^3}q_+\big[q_+ + q_-\big]\Big), \quad \text{(D.21)}$$

$$a_5 = \frac{\pi^{3/2}}{6}\frac{q_+^{5/2}\ell_B^{9/2}}{q_-d_+^{9/2}}\big[q_+ - q_-\big]\big[q_+ + q_-\big]^{5/2}\big[10q_+^4 - 11q_+^3q_- + 13q_+^2q_-^2 - 4q_+q_-^3 + 3q_-^4\big]\ln\Big(\frac{4\pi\ell_B^3}{d_+^3}q_+\big[q_+ + q_-\big]\Big). \quad \text{(D.22)}$$

Notice that m_1, m_2, etc. were defined in Eqs. (D.7–D.16).

D.4 The coefficients in the mean activity coefficient

In Eq. 6.57 we obtained the low-density expansion of the mean activity coefficient of ionic solutions where the ions have valences q_+ and q_- and effective diameters d_+ and d_- (in Ångströms). Defining $\omega \equiv 6.022\times10^{-4}\ell_B^3q_+^6q_-$ (with $\eta \equiv q_-/q_+$ and $\xi \equiv d_-/d_+$), the coefficients in Eq. 6.57 read

$$\nu_{\rm DH} = -\eta\sqrt{\pi\omega[1+\eta]}, \quad \text{(D.23)}$$

$$\nu_1 = \frac{\pi\omega\eta}{6[1+\eta]}\Big\{-1 + 3\eta + 8\eta^2 + 3\eta^3 - \eta^4 + 4\Big[H\big(\epsilon_+\big) + \ln\big(\epsilon_+\big)\Big] + 4\eta^4\Big[H\big(\frac{\eta^2\epsilon_+}{\xi}\big) + \ln\big(\frac{\eta^2\epsilon_+}{\xi}\big)\Big] - 8\eta^2\Big[H\big(-\frac{2\eta\epsilon_+}{1+\xi}\big) + \ln\big(\frac{2\eta\epsilon_+}{1+\xi}\big)\Big] + 8\eta^2[1-\eta^2]\ln(\eta) - \big[2 - 4\eta^2 + 2\eta^4\big]\ln\big(36\pi\omega[1+\eta]\big)\Big\}, \quad \text{(D.24)}$$

$$\nu_{1\log} = -\frac{\pi\omega\eta}{3}[1-\eta]^2[1+\eta], \tag{D.25}$$

$$\begin{aligned}\nu_{3/2} = \frac{\eta[\pi\omega]^{3/2}}{24\sqrt{1+\eta}}\Big\{ & 42 - 6\eta - 14\eta^2 + 68\eta^3 - 14\eta^4 - 6\eta^5 + 42\eta^6 \\ & + 40\big[1-\frac{2\eta}{5}\big]\Big[H\big(\epsilon_+\big) + \ln\big(\epsilon_+\big)\Big] + 40\eta^6\big[1-\frac{2}{5\eta}\big]\Big[H\big(\frac{\eta^2\epsilon_+}{\xi}\big) \\ & + \ln\big(\frac{\eta^2\epsilon_+}{\xi}\big)\Big] + 112\eta^3\Big[H\big(-\frac{2\eta\epsilon_+}{1+\xi}\big) + \ln\big(\frac{2\eta\epsilon_+}{1+\xi}\big)\Big] \\ & - 16\eta^3\big[7 - 2\eta^2 + 5\eta^3\big]\ln(\eta) + 8\eta\big[1-\eta^2\big]^2\ln\big(36\pi\omega[1+\eta]\big) \\ & - 20\big[1+\eta^3\big]^2\ln\big(64\pi\omega[1+\eta]\big)\Big\},\end{aligned} \tag{D.26}$$

$$\nu_{3/2\log} = -\frac{\eta[\pi\omega]^{3/2}}{6}\sqrt{1+\eta}\big[5 - 7\eta + 7\eta^2 + 7\eta^3 - 7\eta^4 + 5\eta^5\big]. \tag{D.27}$$

Appendix E

Notation

We list here some of the symbols used in this work. We tried to keep the notation as clear and consistent as possible, but sometimes the same symbol has been used in different Chapters for different quantities. When this is the case (or there is a risk of confusion) we indicate in bold the Chapter where the symbols are used.

$\widetilde{\ }$	**Chs. 2–5**: denotes that a length has been rescaled with the Gouy-Chapman length μ according to $\widetilde{r} = r/\mu$. **Ch. 6**: denotes that a variable has been multiplied by d_+^3, e.g. $\widetilde{f} = d_+^3\, f$.
$\mathcal{A}$	Hamaker constant.
A	Area.
C_v	Specific heat at constant volume.
c_+, c_-	Bulk concentration of positive and negative ions.
D	**Ch. 4**: Distance at contact between ions on the wall and counterions.
d	**Ch. 5**: Distance between the walls.
d_+, d_-	**Ch. 6**: Diameters of the positive and negative ions.
e	Elementary charge unit. In SI units, $e = 1.60 \times 10^{-19}$ C.
F, f	Canonical ensemble free energy, total and per unit volume respectively.
$\mathrm{f}_\pm$	Mean activity coefficient.
g	Grand-canonical ensemble free energy per volume.
$\mathcal{H}$	Hamiltonian.
$\bar{\mathcal{H}}$	Field-theoretic action.
$\imath$	Imaginary unit, $\imath = \sqrt{-1}$.
k_B	Boltzmann constant. In SI units, $k_B = 1.38 \times 10^{-23}$ J K^{-1}.
L	Box size in the simulations.
ℓ_B	Bjerrum length. Distance at which the electrostatic interaction between two elementary charges equals the thermal energy, i.e., $\ell_B \equiv e^2/4\,\pi\,\varepsilon\,k_B\,T$.
N	**Chs. 2–5**: number of counterions.
N_+, N_-	**Ch. 6**: Number of positive and negative ions.

P	Pressure (in units of k_BT).
$\mathcal{Q}$	Grand-canonical ensemble partition function.
Q	**Ch. 4**: Charge valence of the charges fixed on the plane.
q	**Chs. 2–5**: Charge valence of counterions.
q_+, q_-	**Ch. 6**: Charge valence of positive and negative ions.
T	Temperature.
V	Volume.
$v_c(\mathbf{r})$	Coulomb potential given by Eq. (B.3). In the simplest case, $v_c(r) = \ell_B/r$.
$v_{DH}(\mathbf{r})$	Debye-Hückel potential (Eqs. (6.16) and (6.27)).
$\mathcal{Z}$	Canonical ensemble partition function.
Δ	Dielectric jump constant (image charge prefactor), defined in Eq. (3.7).
$\delta(\mathbf{r})$	Dirac delta function.
ε,$\varepsilon_>$,$\varepsilon_<$	Dielectric constant of a medium. For water, $\varepsilon \simeq 80\,\varepsilon_0$.
ε_0	Dielectric constant of vacuum. In SI units, $\varepsilon_0 = 8.85 \times 10^{-12}$.
ϵ_+	**Ch. 6**: Coupling parameter of the positive ions, defined as $q_+^2 \ell_B/d_+$.
ζ	Used in the Lekner summation as $\lvert z_i - z_j\rvert/L$.
η	**Ch. 2**: used in the Lekner summation as $\lvert y_i - y_j\rvert/L$. **Ch. 6**: charge ratio q_-/q_+.
$\theta(z)$	Theta function: 1 if $z > 0$, 0 otherwise.
Λ	Rescaled fugacity, $\lambda/2\pi\ell_B\sigma_s^2$.
$\lambda, \lambda_+, \lambda_-$	Fugacity (exponential of the chemical potential).
$\lambda_\pm$	Mean activity.
μ	Gouy-Chapman length. It is the distance at which the electrostatic interaction between a charge $q\,e$ and a charged plate (with charge density $\sigma_s\,e$) equals the thermal energy, i.e., $\mu \equiv 1/2\,\pi\,q\,\ell_B\,\sigma_s$.
Ξ	Coupling constant, $\Xi \equiv q^2\,\ell_B/\mu$.
ξ	**Ch. 6**: used in the Lekner summation as $\lvert x_i - x_j\rvert/L$. **Ch. 6**: size ratio d_-/d_+.
$\rho(\mathbf{r})$	Thermal average of the local counterion density distribution.
$\hat{\rho}(\mathbf{r})$	Instantaneous charge distribution (sum of deltas), as in Eq. (6.3).
$\sigma(\mathbf{r})$	General fixed charge density distribution.
σ_s	Charge density on the plates; number of charges per unit area.
$\phi(\mathbf{r})$	Fluctuating field, conjugate to the charge density.
$\psi_+(\mathbf{r}), \psi_-(\mathbf{r})$	Fluctuating fields, conjugate to the number density.
$\omega_{\alpha\beta}$	**Ch. 6**: hard core potential.

Bibliography

[1] R. Abe, Prog. Theor. Phys. **22**, 213 (1959).

[2] M. Abramowitz and I. A. Stegun (editors), *Handbook of mathematical functions*, Dover, New York (1965).

[3] D. J. Adams, J. Chem. Phys. **78**, 2585 (1983).

[4] S. Alexander, P. M. Chaikin, P. Grant et al., J. Chem. Phys. **80**, 5776 (1984).

[5] E. Allahyarov, I. D'Amico and H. Löwen, Phys. Rev. Lett. **81**, 1334 (1998).

[6] M. P. Allen and D. J. Tildesley, *Computer simulations of liquids*, Clarendon Press, Oxford (1987).

[7] D. Andelman, in R. Lipowsky and E. Sackmann (editors), *Handbook of biological physics*, Elsevier, Amsterdam (1995).

[8] P. Attard, in I. Prigogine and S. A. Rice (editors), *Advances in chemical physics*, volume XCII, John Wiley and Sons, New York (1996).

[9] P. Attard, D. J. Mitchell and B. W. Ninham, J. Chem. Phys. **88**, 4987 (1988).

[10] S. Bae, K. Haage, K. Wantke and H. Motschmann, J. Phys. Chem. B **103**, 1045 (1999).

[11] M. Baus and J. Hansen, Phys. Rep. **59**, 1 (1980).

[12] J. J. Binney, N. J. Dowrick, A. J. Fisher and M. E. J. Newman, *The theory of critical phenomena*, Oxford University Press, Oxford (1992).

[13] N. Bjerrum, Kgl. Danske Videnskab. Selskab, Math.–fys. Medd. **7**, 1 (1926); *Selected papers*, pp. 108–119, Einar Munksgaard, Copenhagen (1949).

[14] I. Borukhov, D. Andelman and H. Orland, Phys. Rev. Lett. **79**, 435 (1997).

[15] D. Bratko, B. Jönsson and H. Wennerström, Chem. Phys. Lett. **128**, 449 (1986).

[16] N. V. Brilliantov, Contrib. Plasma Phys. **38**, 489 (1998).

[17] N. V. Brilliantov, C. Bagnuls and C. Bervillier, Phys. Lett. A **245**, 274 (1998).

[18] S. G. Brush, H. L. Sahlin and E. Teller, J. Chem. Phys. **45**, 2102 (1966).

[19] J. N. Butler and R. N. Roy, in K. S. Pitzer (editor), *Activity coefficients in electrolyte solutions*, CRC Press, Boca Raton, 2nd edition (1991).

[20] D. L. Chapman, Phil. Mag. **25**, 475 (1913).

[21] G. V. Childs, http://cellbio.utmb.edu/cellbio/ (online text book on cell biology). Picture originally from Bloom and Fawcet, *A textbook of hystology*, Chapman and Hall, New York, 12th edition (1994).

[22] E. G. D. Cohen and T. J. Murphy, Phys. Fluids **12**, 1404 (1969).

[23] B. E. Conway, *Electrochemical data*, Elsevier, Amsterdam (1952).

[24] F. S. Csajka and C. Seidel, Macromolecules **33**, 2728 (2000).

[25] B. D'Aguanno, P. Nielaba, T. Alts and F. Forstmann, J. Chem. Phys. **85**, 3476 (1986).

[26] S. W. de Leeuw, J. W. Perram and E. R. Smith, Proc. R. Soc. Lond. A **373**, 27 (1980).

[27] P. Debye and E. Hückel, Physik. Z. **24**, 185 (1923).

[28] A. Diehl, M. N. Tamashiro, M. C. Barbosa and Y. Levin, Physica A **274**, 433 (1999).

[29] S. F. Edwards, Philos. Mag. **4**, 1171 (1959).

[30] D. F. Evans and H. Wennerström, *The colloidal domain*, VCH, New York (1994).

[31] P. P. Ewald, Ann. Phys. **64**, 253 (1921).

[32] M. E. Fisher and Y. Levin, Phys. Rev. Lett. **71**, 3826 (1993).

[33] H. Flyvberg and H. G. Petersen, J. Chem. Phys. **91**, 461 (1989).

[34] H. L. Friedman, *Ionic solution theory*, Interscience, New York (1962).

[35] M. J. Gillan, J. Phys. C: Solid State Phys. **7**, L1 (1974).

[36] J. Glimm and A. Jaffe, *Quantum physics: a functional integral point of view*, Springer, Berlin, 2nd edition (1987).

[37] G. Gouy, J. de Phys. **IX**, 457 (1910).

[38] N. Grønbech-Jensen, R. J. Marshl, R. F. Bruinsma and W. M. Gelbart, Phys. Rev. Lett. **78**, 2477 (1997).

[39] R. L. Guernsey, Phys. Fluids **21**, 2162 (1978).

[40] L. Guldbrand, B. Jönson, H. Wennerström and P. Linse, J. Chem. Phys. **80**, 2221 (1984).

[41] B. Ha and A. J. Liu, Phys. Rev. Lett. **79**, 1289 (1997).

[42] E. Haga, J. Phys. Soc. Jpn. **8**, 714 (1953).

[43] J. Hansen and I. R. McDonald, *Theory of simple liquids*, Academic Press, London (1986).

[44] J. Hansen and J. J. Weis, Mol. Phys. **33**, 1379 (1977).

[45] J. Hautman and M. L. Klein, Mol. Phys. **75**, 379 (1992).

[46] S. Ishimaru, Rev. Mod. Phys. **54**, 1017 (1982).

[47] J. Israelachvili, *Intermolecular and surface forces*, Academic Press, London, 2nd edition (1991).

[48] B. Jönson, H. Wennerström and B. Halle, J. Phys. Chem. **84**, 2179 (1980).

[49] B. Jönsson, private communication.

[50] P. Kékicheff, S. Marčelja, T. J. Senden and V. E. Shubin, J. Chem. Phys. **99**, 6098 (1993).

[51] A. L. Kholodenko and A. L. Beyerlein, Phys. Rev. A **34**, 3309 (1986).

[52] R. Kjellander, Ber. Bunsenges. Phys. Chem. **100**, 894 (1996).

[53] R. Kjellander, T. Åkesson, B. Jönsson and S. Marčelja, J. Chem. Phys. **97**, 1424 (1992).

[54] R. Kjellander and S. Marčelja, Chem. Phys. Lett. **112**, 49 (1984).

[55] R. Kjellander and S. Marčelja, J. Chem. Phys. **82**, 2122 (1985).

[56] F. Lado, Mol. Phys. **31**, 1117 (1976).

[57] G. Landhäußer, *Monte-Carlo-Simulation von Polyelektrolytlösungen*, Ph.D. dissertation, Technical University of Berlin (1997).

[58] I. Langmuir, J. Chem. Phys. **6**, 873 (1938).

[59] A. E. Larsen and D. G. Grier, Phys. Rev. Lett. **76**, 3862 (1996). See also http://griergroup.uchicago.edu/˜grier/.

[60] A. W. C. Lau, D. Levine and P. Pincus, Phys. Rev. Lett. **84**, 4116 (2000).

[61] M. Le Bellac, *Quantum and statistical field theory*, Clarendon Press, Oxford (1991).

[62] J. Lekner, Phys. A **157**, 826 (1989).

[63] J. Lekner, Phys. A **176**, 485 (1991).

[64] J. M. H. Levelt Sengers and J. A. Given, Mol. Phys. **80**, 899 (1993).

[65] R. Lipowsky, Prog. Colloid Polym. Sci. **111**, 34 (1998).

[66] D. B. Lukastky and S. A. Safran, Phys. Rev. E **60**, 5848 (1999).

[67] D. MacGowan, J. Phys. C: Solid State Phys. **16**, 59 (1983).

[68] J. E. Mayer, J. Chem. Phys. **18**, 1426 (1950).

[69] D. A. McQuarrie, *Statistical mechanics*, Harper Collins, New York (1976).

[70] N. Metropolis, A. W. Rosenbluth, M. N. Rosenbluth et al., J. Chem. Phys. **21**, 1087 (1953).

[71] H. Möhwlad, Rep. Prog. Phys. **56**, 653 (1993).

[72] A. G. Moreira and R. R. Netz, to be published.

[73] A. G. Moreira and R. R. Netz, Eur. Phys. J. D **8**, 145 (2000).

[74] A. G. Moreira and R. R. Netz, Europhys. Lett. **52**, 705 (2000).

[75] A. G. Moreira and R. R. Netz, Eur. Phys. J. D **13**, 61 (2001).

[76] A. G. Moreira, M. M. Telo da Gama and M. E. Fisher, J. Chem. Phys. **110**, 10058 (1999).

[77] R. Morf, in L. Pietronero and E. Tosati (editors), *Physics of intercalation compounds*, volume 38, Springer, Berlin (1981).

[78] T. Narayanan and K. S. Pitzer, Phys. Rev. Lett. **73**, 3002 (1994).

[79] D. R. Nelson and M. Rubinstein, Phil. Mag. A **46**, 105 (1982).

[80] R. R. Netz, to be published.

[81] R. R. Netz, Phys. Rev. E **60**, 3174 (1999).

[82] R. R. Netz and H. Orland, Eur. Phys. J. E **1**, 67 (2000).

[83] R. R. Netz and H. Orland, Eur. Phys. J. E **1**, 203 (2000).

[84] P. Nielaba, T. Alts, B. D'Aguanno and F. Forstmann, Phys. Rev. A **34**, 1505 (1986).

[85] S. Nordholm, Chem. Phys. Lett. **105**, 302 (1984).

[86] R. H. Ottewill, in F. Candau and R. H. Ottewill (editors), *An introduction to polymer colloids*, Kluwer academic publishers, Dordrecht (1990).

[87] V. A. Parsegian, J. Chem. Soc. Faraday Trans. **62**, 848 (1966).

[88] R. Parsons, *Handbook of electrochemical constants*, Butterworths, London (1959).

[89] R. Penfold, S. Nordholm, B. Jönsson and C. E. Woodward, J. Chem. Phys. **95**, 2048 (1991).

[90] R. Penfold, J. Warwicker and B. Jönsson, J. Phys. Chem. B **102**, 8599 (1998).

[91] P. A. Pincus and S. A. Safran, Europhys. Lett. **42**, 103 (1998).

[92] K. S. Pitzer (editor), *Activity coefficients in electrolyte solutions*, CRC Press, Boca Raton, 2nd edition (1991).

[93] K. S. Pitzer, J. Phys. Chem. **99**, 13070 (1995).

[94] K. S. Pitzer, M. C. P. de Lima and D. R. Schreiber, J. Phys. Chem. **89**, 1854 (1985).

[95] R. Podgornik, J. Phys. A: Math. Gen. **23**, 275 (1990).

[96] R. Podgornik and B. Žekš, J. Chem. Soc., Faraday Trans. 2 **84**, 611 (1988).

[97] J. A. Rard and R. F. Platford, in K. S. Pitzer (editor), *Activity coefficients in electrolyte solutions*, CRC Press, Boca Raton, 2nd edition (1991).

[98] R. A. Robinson and R. H. Stokes, *Electrolyte solutions*, Butterworths, London (1959).

[99] I. Rouzina and V. A. Bloomfield, J. Phys. Chem. **100**, 9977 (1996).

[100] K. Schwister (editor), *Taschenbuch der Chemie*, Fachbuchverlag Leipzig, Leipzig, 2nd edition (1999).

[101] P. Sens and J. Joanny, Phys. Rev. Lett. **84**, 4862 (2000).

[102] A. Shadowitz, *The electromagnetic field*, Dover, New York (1975).

[103] T. Sheldlovsky, J. Am. Chem. Soc. **72**, 3680 (1950).

[104] B. I. Shklovkii, Phys. Rev. E **60**, 5802 (1999).

[105] W. L. Slattery, G. D. Doolen and H. E. DeWitt, Phys. Rev. A **21**, 2087 (1980).

[106] W. L. Slattery, G. D. Doolen and H. E. DeWitt, Phys. Rev. A **26**, 2255 (1982).

[107] R. Sperb, Mol. Simul. **20**, 179 (1998).

[108] O. Stern, Z. Elektrochem. **30**, 508 (1924).

[109] M. J. Stevens and M. O. Robbins, Europhys. Lett. **12**, 81 (1990).

[110] D. J. Tildesley, in M. P. Allen and D. J. Tildesley (editors), *Computer simulations in chemical physics*, Kluwer academic publishers, Dordrecht (1993).

[111] G. M. Torrie and J. P. Valleau, Chem. Phys. Lett. **65**, 343 (1979).

[112] J. P. Valleau, in D. Ceperley (editor), *The problem of long-range forces in the computer simulation of condensed media*, NRCC workshop proceedings **9**, 3 (1980).

[113] J. P. Valleau and S. G. Whittington, in B. Berne (editor), *Modern theoretical chemistry*, Plenum, New York (1977).

[114] E. J. W. Verwey and J. T. G. Overbeek, *Theory of the stability of lyophobic colloids*, Elsevier, New York (1948).

[115] E. Waisman and J. L. Lebowitz, J. Chem. Phys. **56**, 3086 (1972); J. Chem. Phys. **56**, 3093 (1972).

[116] H. Weingärtner, M. Kleemeier, S. Wiegand and W. Schröer, J. Stat. Phys. **78**, 169 (1995).

[117] H. Wennerström, A. Khan and B. Lindman, Adv. Colloid Interface Sci. **34**, 433 (1991).

[118] T. A. Witten, Rev. Mod. Phys. **71**, S367 (1999).

[119] S. Yeh, Y. Zhou and G. Stell, J. Phys. Chem. **100**, 1415 (1996).

Acknowledgments

I thank Prof. Lipowsky for giving me the opportunity to work at the MPIKG. I also would like to thank all my colleges at the theory division of the MPIKG, who make the institute a very creative and productive place to work at. Special thanks to some of my colleges with whom I had the chance to interact in the past three years, some of them still working at the institute, some already gone: Thomas Baumann, Markus Breidenich, Martin Brinkmann, Felix Csajka, Willy Fenzl, Andreas Ferry, Hans-Günter Döbereiner, Prof. Gehard Gomper, Maik Kschischo, Sunil Kumar, Karl-Kuno Kunze, Peter Petrov, Karin Riske, Julian Shilcock, Paul van der Schoot, Peter Swain, Christian Seidel, Udo Seifert, Oliver Theissen, Antonio Valencia, Angelo Valleriani, Euridice Vieira, Thomas Weikl. I also thank Christian Fleck for very interesting discussions. A special thank to Prof. Margarida Telo da Gama, who supported me in various ways.

To Dr. habil. Roland Netz I would like to express my gratitude for his supervision, for the interesting research topics he proposed me and for being always available to discuss. His help went beyond physics, especially in getting adapted to Germany, where he (but also of his family and his wife Petra) played an important role.

I finally thank my friends and my family for the support they offered me all this time. Especially, I thank my parents, Ramiro and Jurema, and Kathrin, for being there. This thesis is dedicated to them.

This work was financially supported by the Portuguese “Fundação para a Ciência e Tecnologia” through the grant Praxis XXI/BD/13347/97 and materially supported by the Max-Planck-Gesellschaft.